Development of Compact Local Power Distribution System for the International Linear Collider

国際リニアコライダーに向けた コンパクトな局所電力分配系の開発

Baiting DU

DOCTOR OF PHILOSOPHY

Department of Accelerator Science

School of High Energy Accelerator Science

The Graduate University for Advanced Studies, SOKENDAI

2020

Supervisor:	Toshihiro Matsumoto
Head Examiner:	Shuji Matsumoto
Examiner:	Shinichiro Michizono
	Toshihiro Matsumoto
	Zhigao Fang
	Ken Watanabe
	Morishita Takatoshi

For all who supported me.

Abstract

In this investigation, a compact Local Power Distribution System (LPDS) for the International Linear Collider (ILC) is developed and tested in the Superconducting RF Test Facility (STF) at the High Energy Accelerator Research Organization (KEK).

The total number of RF units and cavities is 236 and approximately 8,000 for the 250 GeV ILC. Referring to the ILC Technical Design Report (TDR), each group of 39 cavities is driven by one 10 MW multi-beam klystron. The frequency is 1.3 GHz, the repetition rate is 5 Hz, and the pulse width is 1.65 ms. The space between adjacent cavities is 1326 mm. Therefore, the phase difference between adjacent cavities is 90°. The Power Distribution System (PDS) can transmit power from the klystron to the cavities. Each PDS consists of three LPDS and each LPDS contains three 4- or 5-cavity LPDS. The maximal input power of the 5-cavity LPDS is approximately 1.3 MW. The ILC-TDR indicates that the variable hybrid and variable phase shifter of the LPDS should be controlled remotely. Moreover, its power dividing ratio should satisfy the ±20% variation of the accelerating gradient of each cavity to achieve the maximal average accelerating gradient. Due to the limited space of the tunnel, the LPDS is expected to be constructed, and integrated with the cryomodule on the ground and to be moved into the tunnel by a cart. In the case of the LPDS designed in the ILC-TDR, it seems to be difficult of facilitating removal of the cart after the installation process of the cryomodule. To address this difficulty and reduce the production cost, the compact LPDS is developed. The cryomodule integrated with the compact LPDS is expected to be installed in the tunnel.

Several candidate models for a compact LPDS are proposed. The new variable hybrid, variable phase shifter, and fixed phase shifter are designed for the compact LPDS. They have geometric lengths of 730 mm, 300 mm, and 296 mm (or 1026 mm) respectively, to satisfy the distance between the cavities. The ±25% variation of the power fed to the cavity is evaluated to satisfy the ±20% variation of the accelerating gradient. To achieve the ±25% variation of power dividing ratio, the variable hybrid has an adjusted range of the coupling ratio from -8.84 dB to -2.04 dB. The maximal phase shift of the variable hybrid is evaluated to be 17.0° when the power dividing ratio is adjusted within ±25%. The adjusted phase range of the variable phase shifter is 38.4°, which can compensate for the phase shift of the variable hybrid and a margin of more than 15°. When the variable hybrid is set for average power distribution and the variable phase shifter is set on the center of the phase adjusted range, the fixed phase shifter is designed by increasing or decreasing the width of the waveguide to adjust the phase difference between adjacent cavities, which is 90°.

Based on the assumption of uniform distribution of the cavity acceleration gradient (31.5 MV/m ± 20%) and detuning, the distribution of required power of the cavity and the tolerance of detuning by the low level RF control system is

evaluated. Considering the 236 RF units for the 250 GeV ILC, the probability which the compact LPDS can adjust all 39 cavities of a RF unit to their maximal accelerating gradient is at least 99.6%. This probability is analyzed with the condition of equal Q_L and P_kQ_L control of superconducting cavities, respectively. In the case of the equal Q_L operation, the tolerance of detuning should be controlled within $\pm$16 Hz. In the case of the P_kQ_L control with on resonance operation, the compact LPDS can adjust all 39 cavities to its maximal accelerating gradient.

The three variable hybrids, four variable phase shifters, and three fixed phase shifters are manufactured, and the measured S parameter can satisfy the requirements of the compact LPDS. In the average condition that 39 cavities are fed equal power from the 10 MW MBK, the input power of the compact LPDS for five cavities is 1.3 MW with a pulse width of 1.65 ms, and the interlock time is approximately 7 μs, which shut down the power source to protect the RF system from arcing. The required power handling capability is evaluated of 2.0 MW with a pulse width of 2 ms, and 5.2 MW with a pulse width at least 50 μs. The L-band resonant ring is constructed in the STF to generate a traveling wave of up to 5.2 MW to evaluate the power handling capability of RF components. Part of the resonant ring is filled with SF_6 gas to prevent arcing and 10 acoustic sensors are installed on the resonant ring to detect the arcing position. Finally, the power handling capabilities of these RF components are demonstrated, which satisfies the requirements of the compact LPDS.

The compact LPDS for 4 cavities is constructed in the STF. The test result indicates that the adjusted power dividing ratio for each cavity can satisfy the $\pm$25% variation, and the phase between adjacent cavities can be maintained at 90°. In this work, the feasibility of a compact LPDS is demonstrated and the operated procedure of this system is developed. The compact LPDS will be installed on the cryomodule of 'CM-2a' in the STF, and demonstrated with beam operation in 2021.

Contents

Chapter 1

Introduction

1.1 General Introduction

The ILC is a 250 GeV linear electron–positron collider based on 1.3 GHz Superconducting RF (SCRF) technology [1]. The electron and position beams are accelerated to 125 GeV by a 20.5 km Linear Accelerator (LINAC). Figure 1.1 shows the concept of the 250 GeV ILC [2]. The ILC was proposed to prove the existence of the Higgs field and to study the quantum properties of the Higgs boson to experimentally evaluate the Standard Model. A collision energy of 250 GeV supports the peak cross section for the reaction $e^+e^- \rightarrow Zh$. The decay rate of the Higgs boson to various types of quarks, leptons, and bosons can be precisely measured using the ILC. The full design energy of the ILC is 500 GeV, to facilitate the study of the Higgs boson for the reaction $e^+e^- \rightarrow \nu\bar{\nu}h$ to measure the absolute normalization of the underlying Higgs coupling strength. Thus the length of tunnel for the 250 GeV ILC is expected to be 33.5 km allow for extending of the ILC to increase the collision energy to 500 GeV.

The luminosity of the 250 GeV ILC is $1.35 \times 10^{34}\mathrm{cm}^{-2}\mathrm{s}^{-1}$ and the beam current is 5.8 mA [3]. The horizontal and vertical emittance are 10 μm and 35 nm, respectively. The superconducting cavity of the Tesla type is occupied for the ILC with the designed accelerating gradient of 31.5 MV/m. The number of RF stations and cavities are approximately 220 and 8000, respectively. In the RF system, the 10 MW multi–beam klystron is used as the power source.

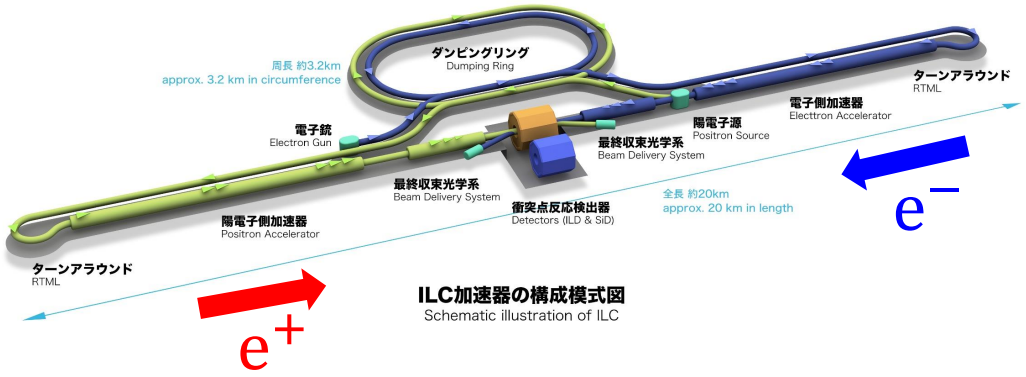

Figure 1.1: Concept of the 250 GeV ILC [2].

1.2 Goal of this Study

The goal of this study is the development of a compact Local Power Distribution System (LPDS) for the ILC. To achieve this goal, the results of previous studies are considered.

Referring to the ILC Technical Design Report (TDR) [1], each of 39 cavities are driven by one 10 MW multi-beam klystron. The average accelerating gradient of the superconducting (SC) cavity is 31.5 MV/m. The maximal accelerating gradient of the SC cavity has a variation of ±20% due to manufacturing differences. The Power Distributed System (PDS) transmits RF power from one klystron to 39 cavities. Each PDS consists of three LPDSs. The variable hybrid and variable phase shifter in the LPDS adjust the input power and RF phase of each cavity. The accelerating field in the SC cavity is close to the quench limit and the beams are accelerated on the crest of the RF field. The variable hybrid and variable phase shifter of the LPDS should be controlled remotely and the variation of the power fed to the cavities can satisfy the ±20% variation of the maximal accelerating gradient. The cryomodule integrated with the LPDS is expected to be installed in the tunnel using a cart. The lowest position of the LPDS in the ILC TDR is lower than that of the cryomodule. Thus, the LPDS can only be constructed and assembled in the tunnel. Otherwise, the cart cannot be removed after the installation process. Difficulty in the assembly of the LPDS is encountered. The goal of developing a compact LPDS is to satisfy the requirements of the LPDS, to address the assembly difficulty, and to reduce the production cost.

To address the difficulty in the the assembly process, the compact LPDS is expected to be constructed and assembled to the cryomodule on the ground.

Then, the integration of the compact LPDS and the cryomodule are installed in the tunnel. The position of the variable phase shifter is moved from the vertical line to the horizontal line. Thus, the lowest position of the compact LPDS is higher than that of the cryomodule, which leaves enough space for the installation cart.

The geometric length between adjacent cavities is 1326 mm, which is 5.75 λ_0 at 1.3 GHz. The phase difference between adjacent cavities should be 90°. The compact LPDS should follow this length. The new variable hybrid and variable phase shifter are designed with shorter geometric lengths. The reduced phase shift range is caused by the shorter variable phase shifter. Thus, the fixed phase shifter is developed to adjust the phase difference between adjacent cavities to 90° in advance, and the variable phase shifter is used to compensate for the phase shift of the variable hybrid.

In the case of the variable hybrid, the goal is to adjust the range of the coupling ratio from -8.84 dB to -2.04 dB to satisfy the ±25% variation of the power dividing ratio. This ±25% variation can satisfy the ±20% variation of the accelerating gradient of each cavity. In the final design, the geometric length of the variable hybrid is decreased to 730 mm.

In the case of the variable phase shifter, the adjusted range of the phase will decrease with the decrease of the geometric length. It should compensate for the 17° phase shift of the variable hybrid and has a phase of 15° for beam on-crest searching. Thus, the purpose of the variable phase shifter is to achieve a phase range of at least 32°. In the final design, the geometric length of the variable phase shifter is decreased to 300 mm.

In the case of the fixed phase shifter, it should adjust the phase difference between adjacent cavities of 90° when the variable hybrid is set for the average power distributed condition, and the variable phase shifter is set at the center of its adjusted phase range. Based on the limitation of the geometric length, the lengths of the fixed phase shifters are 296 mm or 1026 mm. To reduce the production cost, the fixed phase shifter designed with a wider or narrower waveguide width is used to change the phase. Due to the limitation of the cut off mode and high order mode, the 296 mm fixed phase shifter cannot achieve a phase range of 360°.

In the case of the LPDS for 5 cavities, the maximal input power is approximately 1.3 MW with a pulse width of 1.65 ms. The power handling capability of the RF components should be evaluated. Considering the worst condition of total reflection for which the power may be quadrupled, a power handling capability of 5.2 MW is necessary. With the 7 μs interlock time of the VSWR meter that monitors the reflected power, the RF components are operated at 5.2 MW with a pulse width of more than 50 μs, and can satisfy the requirements of the power handling capability. Moreover, the RF compo-

nents can be operated at 2.0 MW with a pulse width of 2 ms, corresponding to the maximal standing wave with an incident power of 1.3 MW and -13 dB (5%) of reflected power.

To protect the power source, the L-band resonant ring is constructed in the STF at the KEK for high power testing of the RF components. The 800 kW klystron is used as the power source to generate 5.2 MW in the resonant ring. The 500 kW circulator is used to protect the klystron. Ten acoustic sensors are installed on the resonant ring to detect the arcing positions. Thus, the power gain of the resonant ring should be more than 10 dB.

The compact LPDS is constructed in the STF. The evaluated goal of the compact LPDS is to adjust the power range of $\pm 25\%$ and the phase difference between adjacent cavities can be fixed at 90° during the adjustment of power dividing ratio and beam on-crest searching.

1.3 Structure of the Dissertation

The dissertation is dividing into eight chapters. A short overview of each chapter is given in the following.

- In chapter 2, an introductions to the PDS of the ILC and the ILC–like accelerators used worldwide is presented.
- In chapter 3, an introduction to the requirements of compact LPDS is given. Several candidate models are proposed. The RF components of variable hybrid, variable phase shifter, and fixed phase shifter are designed for the compact LPDS.
- In chapter 4, an introduction to probabilistic analysis of the compact LPDS is given.
- In chapter 5, the details of the construction of the L-band resonant ring in the STF at KEK are presented. The theory and power gain are demonstrated based on the low power test. High power operation is performed. A circular power of 4.5 MW with a pulse width of 1.65 ms is achieved.
- In chapter 6, the S parameter and power capability of the RF components are evaluated to satisfy the requirements of the compact LPDS. The L-band resonant ring is used to evaluate power handling capability.
- In chapter 7, the details of the construction of the compact LPDS in the STF at KEK is presented and its feasibility is demonstrated.

Chapter 2

Power Distribution System for Accelerator

In this chapter, the power distribution system (PDS) for three superconducting accelerators is introduced. The PDS for the International Linear Collider (ILC) is compared to the PDS for the Superconducting RF Test Facility (STF) and the European X-band Free Electron Laser (EXFEL). The common points of ILC, STF, and EXFEL are pulse operated using the supper-conducting RF technology of 1.3 GHz.

2.1 RF System for the ILC

2.1.1 Introduction of theSC cavity for the ILC

The 9–cell Tesla–type Superconducting (SC) standing wave cavity is used to accelerate electron and positron beams to 125 GeV, respectively, for the 250 GeV ILC [3]. The RF frequency is 1.3 GHz with a repetition rate of 5 Hz. Figure 2.1 shows the 9–cell superconducting cavity for the ILC. The effective length of the cavity is 1,038.5 mm [1]. The distance between cavities is 1,326.7 mm, which is equal to $5.75\lambda_0$ (λ_0 is the wavelength at 1.3 GHz in free space). The average accelerating gradient is 31.5 MV/m with a variation of $\pm 20\%$ depending on the cavity's performance. The average power fed to the SC cavity is 190 kW. The tunable range of the resonant frequency of the SC cavity is ± 300 kHz. The quality factor of the SC cavity is higher than 1×10^{10} and the matched loaded Q is 5.4×10^6. The filling time of the SC cavity is 924 μs and the beam pulse width is 727 μs. Thus, the total RF pulse width is 1650 μs. Table 2.1 displays the key parameters of the superconducting cavity for ILC.

Table 2.1: Key parameters of the superconducting cavity for ILC [1].

Accelerating structure	Standing wave
Accelerating mode	TM_{010},π mode
Cells	9
Fundamental frequency	1.3 GHz
Tunable range	$\pm$300 kHz
Effective length	1038.5 mm
Distance between cavities	1326.7 mm
Average gradient	31.5 MV/m
Gradient fluctuation	$\pm$20%
Average RF power	190 kW
Quality factor (31.5 MV/m)	$>1 \times 10^{10}$
Matched loaded Q	5.4×10^{6}
R/Q	1036 Ω
Filling time	924 μs
Beam pulse	727 μs
Total RF pulse	1650 μs
Repetition rate	5 Hz

Figure 2.1: 9-cell superconducting cavity for the ILC.

The SC cavity is assembled in the cryomodule to achieve the extremely low temperature of 2 K and SC's performance. There are two types of cryomodules, type A contains nine cavities and type B contains eight cavities and a SC quadrupole package. The length of the cryomodule is 12.652 m. Figure 2.2 shows the longitudinal view of the cryomodule (Type B) with eight cavities and a central quadrupole. Table 2.2 displays the parameters for the cryomodule for the ILC.

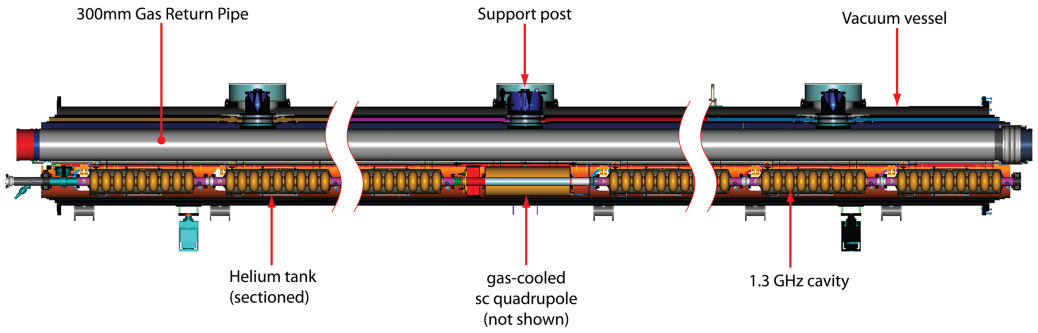

Figure 2.2: Longitudinal view of cryomodule (Type B) with eight cavities and a central quadrupole [1].

Table 2.2: Parameters of the cryomodule for the ILC [1].

Length of cryomodule	12.652 m
Type A	9 cavities
Type B	8 cavities + 1 quad package
Cryogenic	Liquid Helium
Lowest temperature	2 K

2.1.2 Power Distribution System for the ILC

The Power Distribution System (PDS) is used to transmit RF power from a power source to the SC cavities. A PDS for more standard Distributed Klystron Scheme (DKS) was developed for a mountainous topography [1]. Figure 2.3 shows the PDS of the DKS option for the ILC. A 10 MW multi–beam klystron (MBK) is used as the power source to drive 39 Tesla type 9–cell SC cavities, which are assembled in 4.5 cryomodules [1]. There are two output ports with 5 MW power each for the 10 MW MBK [4]. These two 5 MW power are distributed to three 3.33 MW power via two hybrids with a power distributed ratio of 2:1 and a power combiner. Then, the three 3.33 MW power are transmitted to three Local Power Distribution Systems (LPDS). Each LPDS is connected to 13 SC cavities.

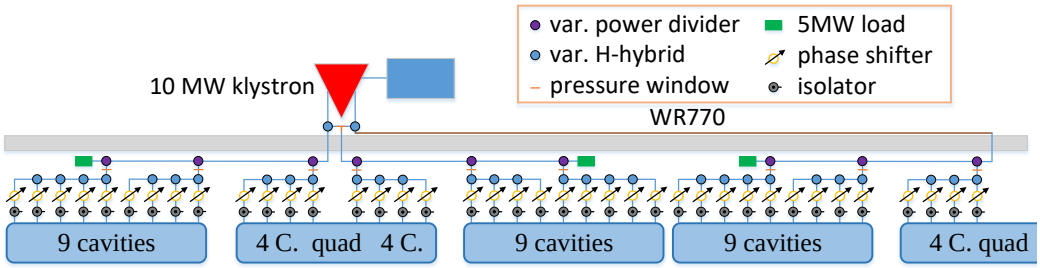

Figure 2.3: Power Distribution System (PDS) of the Distributed Klystron Scheme (DKS) option for the ILC [1]. The DKS option is developed for a mountainous topography. Each PDS contains three Local PDSs (LPDS).

Figure 2.4 shows an image of the 10 MW MBK. The peak output power is 10 MW. The pulse width and repetition rate are 1.65 ms and 5 Hz, respectively, and the average output power is 82.5 kW. The MBK splits the electron current into six beams of low perveance, and the beam voltage is decreased to reduce the space–charge effect. Thus, the power efficiency is improved to 65%. The lifetime is more than 40,000 hours. Table 2.3 displays the parameters for the 10 MW MBK.

Figure 2.4: Image of 10 MW multi–beam klystron [5].

Table 2.3: Parameters of 10 MW multi–beam klystron [1].

Frequency	1.3 GHz
Peak output power	10 MW
Pulse width	1.65 ms
Repetition rate	5 Hz
Average output power	82.5 kW
Lifetime	>40,000 hours

In the case of the PDS of the DKS option, a "Kamaboko–shaped" tunnel is designed. Figure 2.5 shows a cross section of the "Kamaboko–shaped" tunnel. The tunnel has a width of 11 m and is divided into two corridors by a thick (2.0 m $\sim$ 3.5 m) concrete wall. The cryomodule and RF system that contains signal modulators, power supplies, and the klystron, are installed in the two corridors, respectively. The concrete wall can effectively reduce the radiation to the RF system and the equipment for RF system can be repaired or replaced during beam operation.

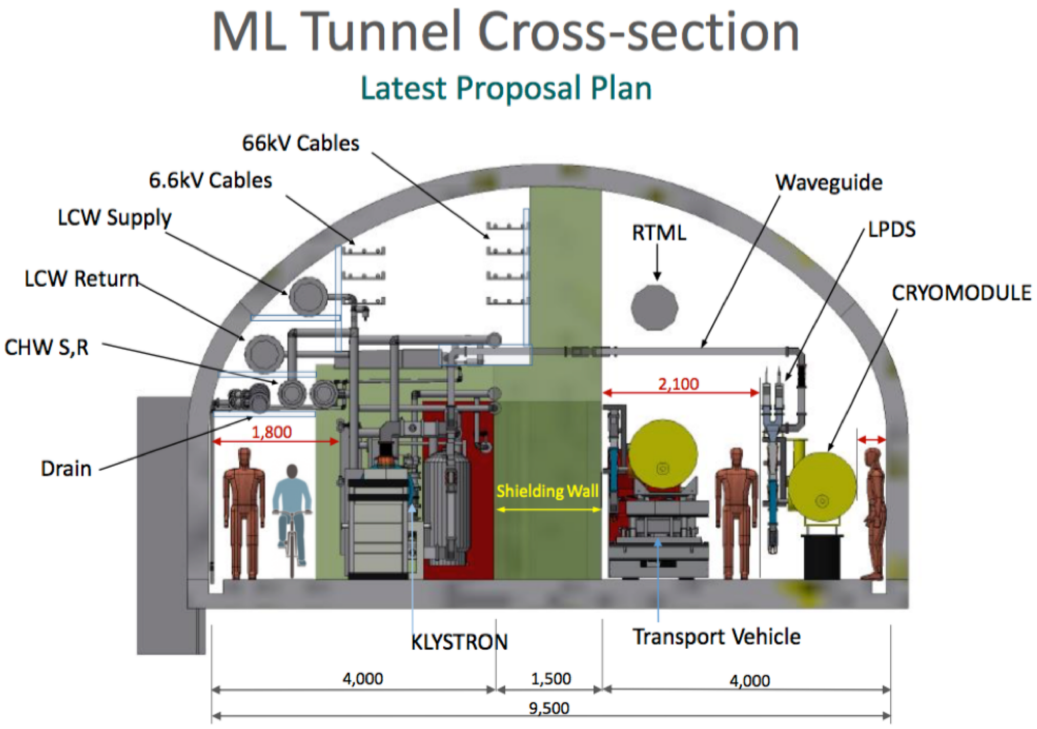

Figure 2.5: Cross section of "Kamaboko–shaped" tunnel [6]. This tunnel is designed for the DKS option and mountainous topography.

2.1.3 Local Power Distribution System for the ILC

Figure 2.6 shows the CAD model of the Local Power Distribution System (LPDS) for 13 cavities. The input power of the LPDS for 13 cavities is approximately 3.3 MW. This LPDS contains two secondary LPDSs for four cavities and a secondary LPDS for five cavities. The RF power is transmitted to each secondary LPDS via the WR650 type waveguide.

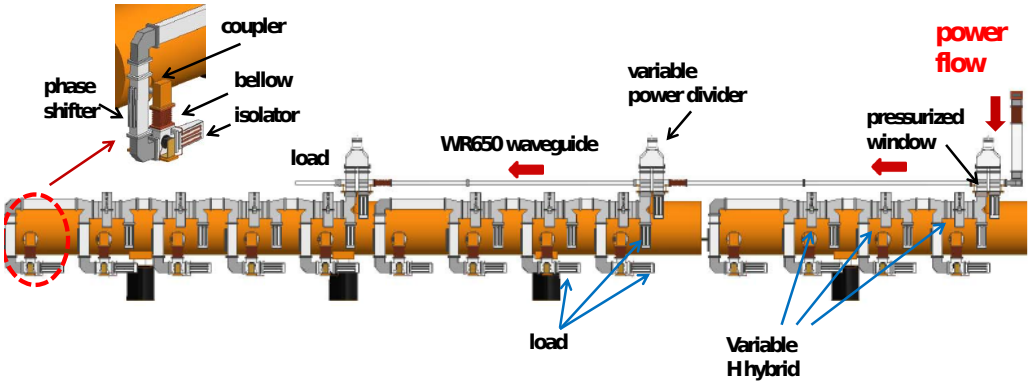

Figure 2.6: CAD model of the Local Power Distribution System (LPDS) for 13 cavities [1].

The accelerating gradient of the SC cavity has a variation of ±20% due to the cavity's performance. To achieve the maximal average accelerating gradient, the input power of each cavity should be different to operate all the SC cavities close to the quench limit. Thus, the input power of each secondary LPDS for four or five cavities will also be different. As shown in Fig 2.6, three variable power dividers (VPD) are used to divide the power supplied to each secondary LPDS. The input power and phase of each secondary LPDS can be adjusted via the VPD. Figure 2.7 shows the schematic of the VPD, U-bend phase shifter, and the magic tee. The VPD is a 4-port component that consists of two folded magic tees and two U-bend phase shifters [7]. The U–bend phase shifter was designed in the SLAC. A pair of waveguides with a length of a quarter wavelength is inserted between the magic tee and a U–bend phase shifter. Port–2, port–3, and port–4 of the VPD are connected to the next VPD or the terminal dummy load, LPDS, and dummy load, respectively.

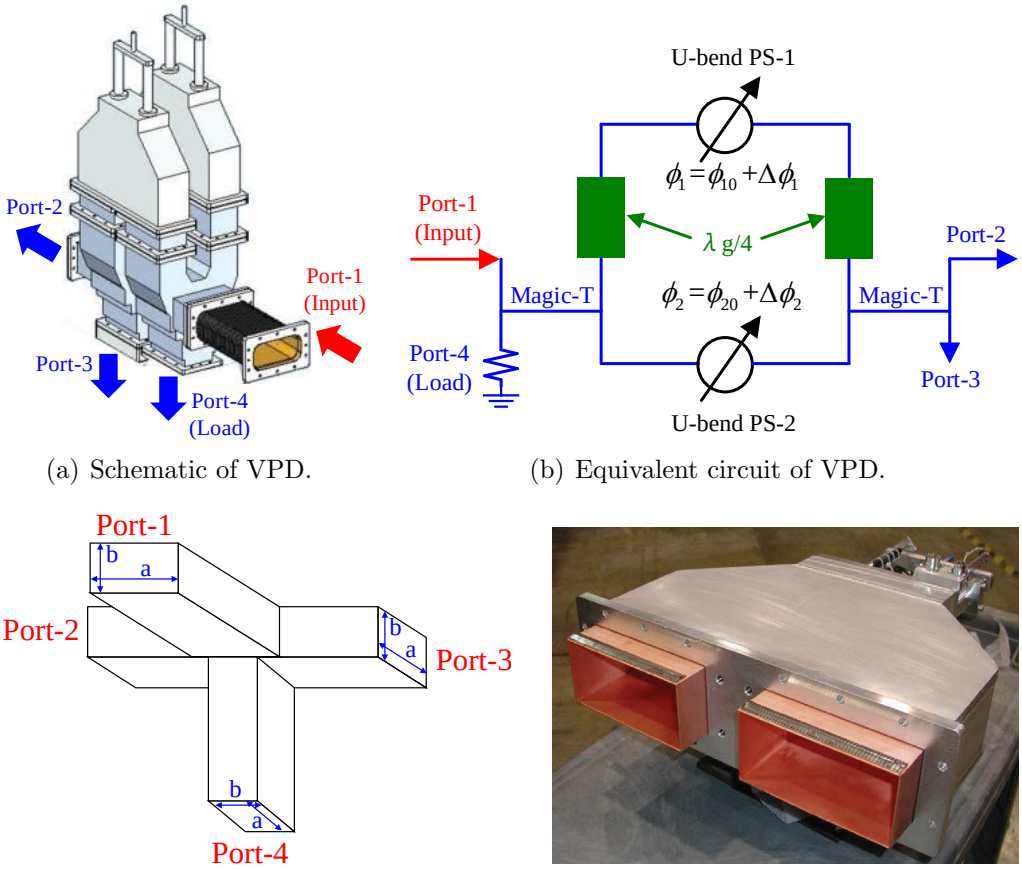

(a) Schematic of VPD.

(b) Equivalent circuit of VPD.

(c) Magic tee.

(d) U-bend Phase Shifter.

Figure 2.7: Schematic of the Variable Power Divider(VPD), U-bend phase shifter, and magic tee. The VPD is composed of two folded magic tees and two U-bend phase shifters.

The scattering matrix of the symmetric magic tee [8] is

$$[S_T] = \frac{-j}{\sqrt{2}} \begin{bmatrix} 0 & 1 & 1 & 0 \\ 1 & 0 & 0 & -1 \\ 1 & 0 & 0 & 1 \\ 0 & -1 & 1 & 0 \end{bmatrix} \tag{2.1}$$

The output voltage of port–2 and port–3 of the VPD can be calculated using Eq. 2.2. ϕ_{10} and ϕ_{20} are the initial phase of the two U-bend phase shifters, whereas $\Delta\phi_1$ and $\Delta\phi_2$ are the shifted phase of two U-bend phase shifters.

$$\begin{cases} V_2 = -j\sin(\frac{\phi_2-\phi_1}{2})e^{j[(\phi_1+\phi_2)/2]} \\ V_3 = -\cos(\frac{\phi_2-\phi_1}{2})e^{j[(\phi_1+\phi_2)/2]} \end{cases} \tag{2.2}$$

The power dividing ratio and phase of Port–2 and Port–3 can be adjusted for the full range by adjusting the phase of the two U-bend phase shifters. The pure adjustment of power can be achieved by moving the two U-bend phase shifters in opposite directions ($\Delta\phi_1 = -\Delta\phi_2$, $\phi_2 + \phi_1 = con.$), and the output phase of the VPD is fixed. Pure adjustment of the phase can be achieved by moving the two U-bend phase shifters in the same directions ($\Delta\phi_1 = \Delta\phi_2$, $\phi_2 - \phi_1 = con.$), and the output power of the VPD is fixed.

To adjust the input power of each cavity to the maximal value, a variable hybrid is used in the LPDS [1]. Figure 2.8 shows a schematic of the variable hybrid used for the ILC. The variable hybrid is a 4–port RF components. The distance from port–1 to port–2 of this hybrid is 1,100 mm. The input power from port–1 is divided and output from the port–2∼4. The output power of port–2 and port–3 are transmitted to the secondary variable hybrid and cavity, respectively. The output power of port–4 is expected to be less than -20 dB. Two metallic fins are symmetrically inserted in the variable hybrid. The power distributed ratio between port–2 and port–3 can be adjusted by moving the two fins symmetrically.

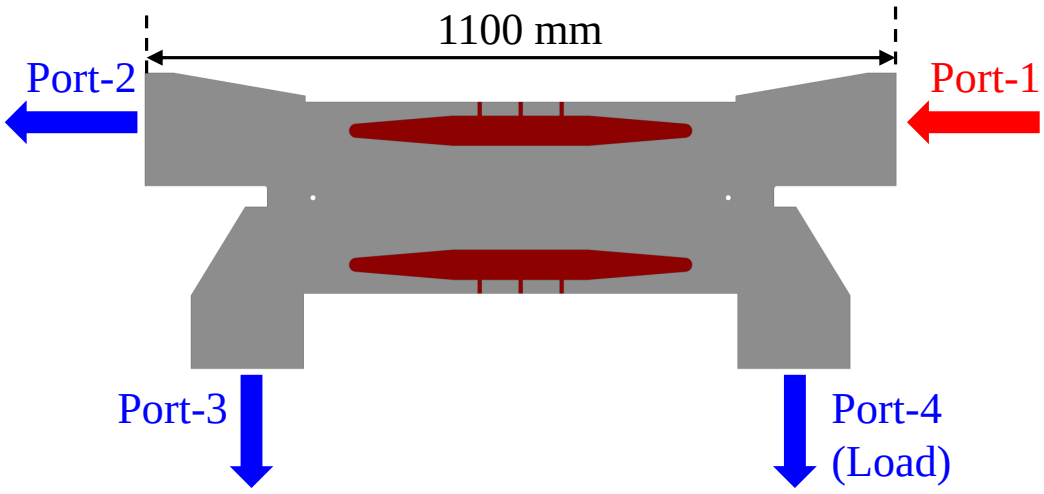

Figure 2.8: Schematic of variable hybrid for the ILC [1].

The beam energy transferred from the RF field can be improved if the beam is accelerated on the crest of the field. The variable phase shifter is used to adjust the phase of the RF field. Figure 2.9 shows a schematic of the variable phase shifter for the ILC. The length of this variable phase shifter is 600 mm. A metallic fin is moved in the waveguide to adjust the transmitted phase [9].

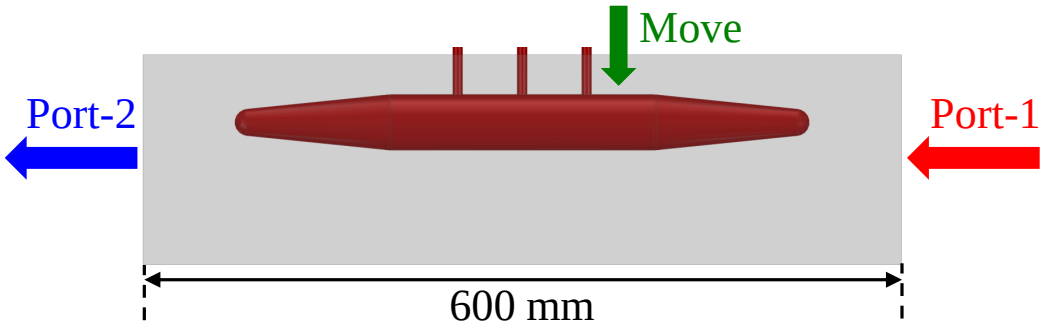

Figure 2.9: Schematic of the variable phase shifter for the ILC [9].

The isolator and bellow are installed before the input coupler. The isolator can prevent the reflected power from the SC cavity from be transmitted to the LPDS. This reflected power is absorbed by the dummy load connected to the isolator. There are two coupling outputs on the input and load ports of the isolator, to monitor the power and phase of the forward and reflected signal of the SC cavity. The bellow provides the adjustment of the geometric length for the installation of the LPDS.

In conclusion, the PDS and LPDS for the ILC are developed. The 10 MW MBK is used as the power source to drive 39 SC cavities. The variable power divider and the variable hybrid are used to adjust the transmitted power to each secondary LPDS and the cavity, respectively. The variable phase shifter is used to adjust the phase of the RF field. Under ideal conditions, the accelerating gradient of the SC cavity is close to the quench limit and the beams are accelerated on the crest of the RF field.

2.1.4 Local Power Distribution System for the STF

The Superconducting RF Test Facility (STF) was built to demonstrate RF technology for the ILC [10]. Figure 2.10 shows the STF-2 accelerator constructed in the STF. The STF-2 accelerator is composed of a photocathode RF gun, a capture cryomodule containing two SC cavities, a cryomodule (CM–1) containing eight SC cavities, and a cryomodule (CM-2a) containing four SC cavities. During the beam operation in 2019, eight SC cavities in the CM–1 and CM–2a were operated. The maximal beam energy was 271 MeV and the average accelerating gradient of the eight SC cavities was 32 MV/m. Table 2.4 displays the parameters of the beam operation for the STF-2 accelerator at the STF in 2019.

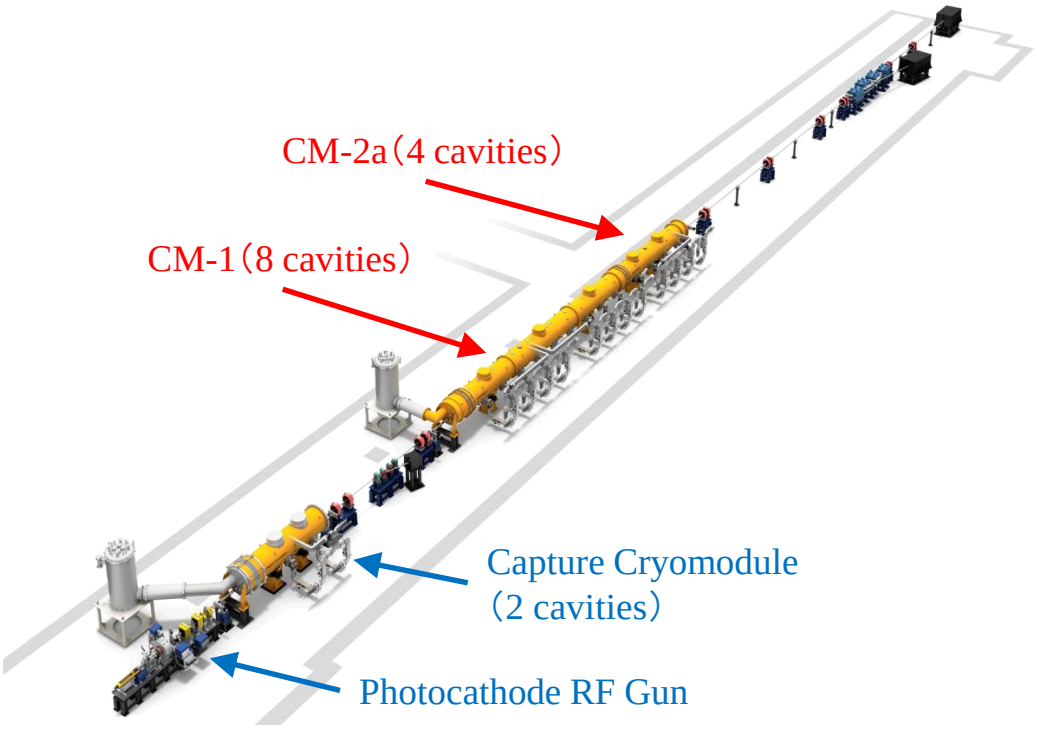

Figure 2.10: STF-2 accelerator constructed in the STF [10].

Table 2.4: Parameters for beam operation of the STF-2 accelerator at the STF in 2019.

Operated cavities	2(Capture) + 8 (CM–1 & CM–2a)
Beam energy	271 MeV
Average acc. gradient	32 MV/m

Figure 2.11 shows the LPDS constructed in the STF. Due to the difference between the cryomodule in the STF and the one in the ILC, the LPDS in the STF is also different compared to the one in the ILC-TDR. The variable hybrid is connected to two H-corners, a horizontal spacer, and two vertical spacers. The H-corners and horizontal spacers are used to adjust the distance between the variable hybrid to 1,326 mm. The vertical spacers are used to adjust the phase difference between adjacent cavities to 90°. The length of the vertical spacers is different for each cavity. To test the quench limit of the SC cavity, the input power of the LPDS is greater than the summation of the designed power of the total cavities. Thus, one more variable hybrid

is installed before the last SC cavity. The redundant power can be absorbed by the dummy load connected to the last variable hybrid.

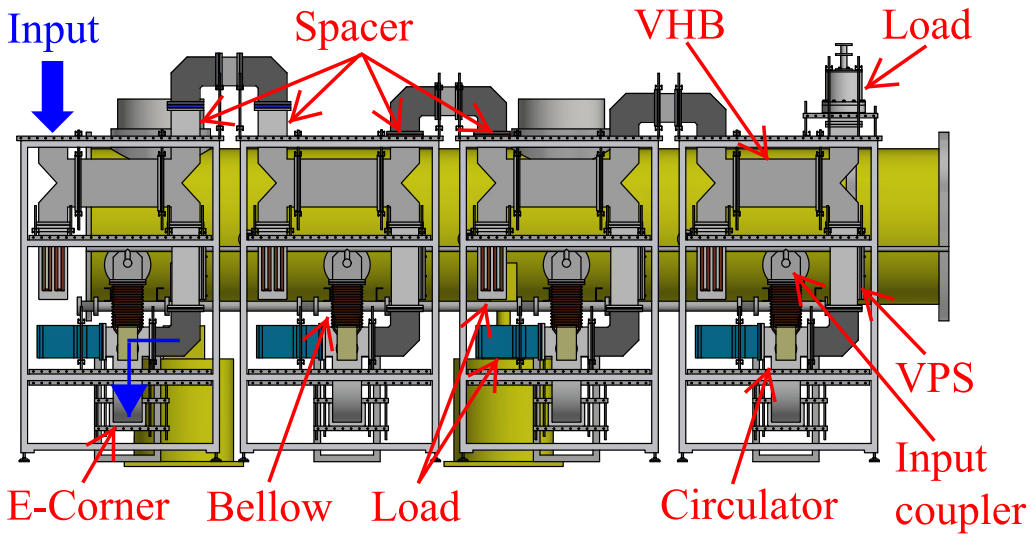

Figure 2.11: LPDS constructed in the STF. The VHB is a variable hybrid. The VPS is a variable phase shifter.

2.2 Power Distribution System for the EXFEL

The 3.4 km European X-band Free Electron Laser (EXFEL) was constructed in the DESY to generate extremely intense X–ray flashes [11]. The first laser pulse was produced in May 2017. Superconducting RF technology was utilized for the EXFEL. The RF power has a frequency of 1.3 GHz, a repetition rate of 10 Hz, and a pulse width of 1,380 μs, with a filling time of 780 μs. The SC cavity is also 9–cell Tesla–type with an accelerating gradient of 23.6 MV/m. Table 2.5 shows the key parameters of superconducting cavity for the EXFEL. The RF system of the ILC is very similar to the EXFEL except for the pulse width, the repetition rate, and the accelerating gradient.

Table 2.5: Parameters of the superconducting cavity for EXFEL [11].

Accelerating structure	Standing wave
Accelerating mode	TM_{010},π mode
Cells	9
Fundamental frequency	1.3 GHz
Tuning range	±300 kHz
Effective length	1038 mm
Distance between cavities	1383.6 mm
Average gradient	23.6 MV/m
Average RF power	122 kW
Quality factor	$>1 \times 10^{10}$
Matched loaded Q	$\sim 4.6 \times 10^{6}$
R/Q	1036 Ω
Filling time	780 μs
Beam pulse	600 μs
Total RF pulse	1380 μs
Repetition rate	10 Hz

There are 27 RF stations for the EXFEL. Each RF station is driven by a 10 MW MBK and transmits RF power to 32 cavities that are equally assembled in four cryomodules. Figure 2.12 shows the compact Waveguide Distribution System (WDS) for the EXFEL. This system (WDS) is developed to conserve tunnel space, increase reliability, and decrease the mounting time of the WDS [12].

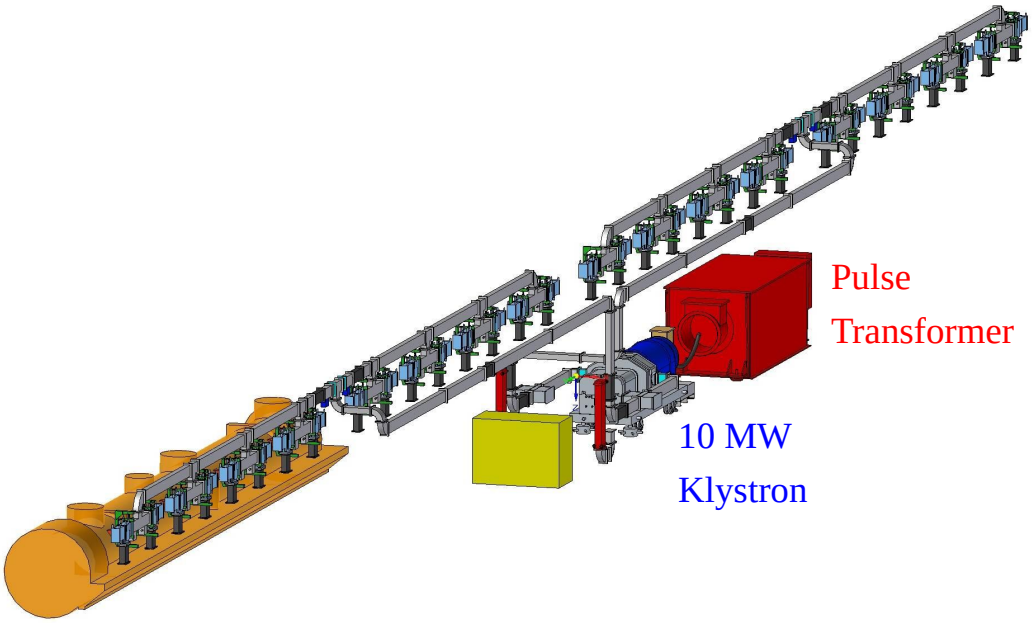

Figure 2.12: Compact waveguide distribution system for the EXFEL [12]. Each 32 SC cavities assembled in four cryomodules are driven by a 10 MW MBK.

Figure 2.13 shows a schematic of the compact WDS for eight cavities. It is composed of three pre–tunable asymmetric shunt tees, three fixed phase shifters, and four binary cells [13]. Three asymmetric shunt tees divide the power equally to four binary cells. The fixed phase shifter adjusts the phase difference between the binary cells to 0°. Each binary cell is connected to two SC cavities and composed of a long shunt tee integrated with a phase shifter, two 500 kW circulators, two 500 kW dummy loads, and two waveguide bellows. The circulator integrated with the dummy load is called an isolator. The reflected power from the SC cavity is very high during the filling and decay time. By placing the phase shifter between the isolator and the klystron, the maximal voltage of the standing wave can be reduced by half. The lengths of the long shunt tee, asymmetric shunt tee, and fixed phase shifter are 940 mm, 380 mm, and 2387 mm, respectively. The fixed phase shifter is designed using different cross sections with the WR650 to shift the phase from $-220°$ to 0°.

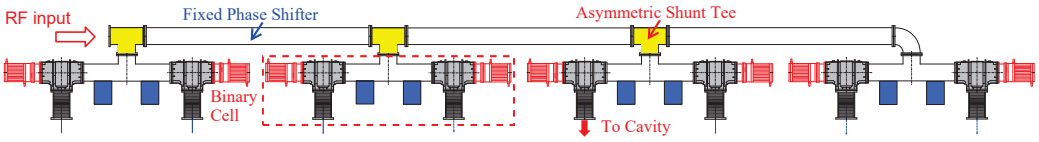

(a) Compact WDS for eight cavities.

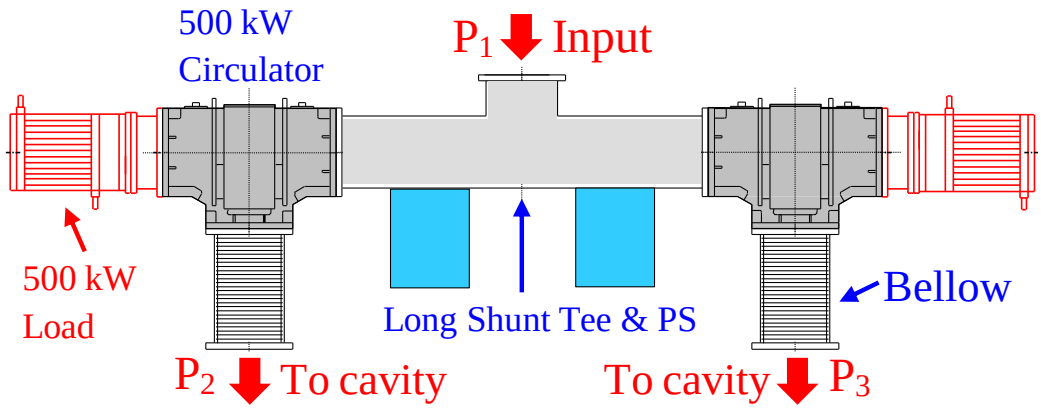

(b) Binary cell.

Figure 2.13: Schematic of the compact waveguide distribution system (WDS) for eight cavities and the binary cell for EXFEL [13].

Figure 2.14 shows the model for a long shunt tee of the compact WDS for EXFEL. Two pistons of length 370 mm are symmetrically placed in the long shunt tee [14]. The phase of each output port is changed by 90° when the piston is moved 25 mm. A metallic post is placed inside the long shunt tee. The power distributed ratio of the two output ports (P_2 and P_3) can be adjusted by tuning the horizontal position of the post for the fluctuation of the accelerating gradient of cavities. In case the SWR is less than 1.2, the tunable range of P_2/P_3 is ±6 dB and the maximal phase difference between two outputs is shifted by ±60° during this adjustment.

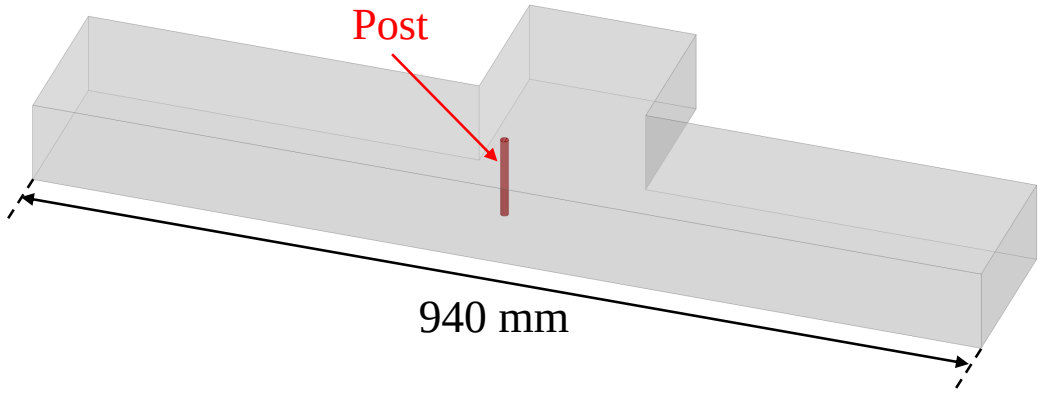

(a) Model.

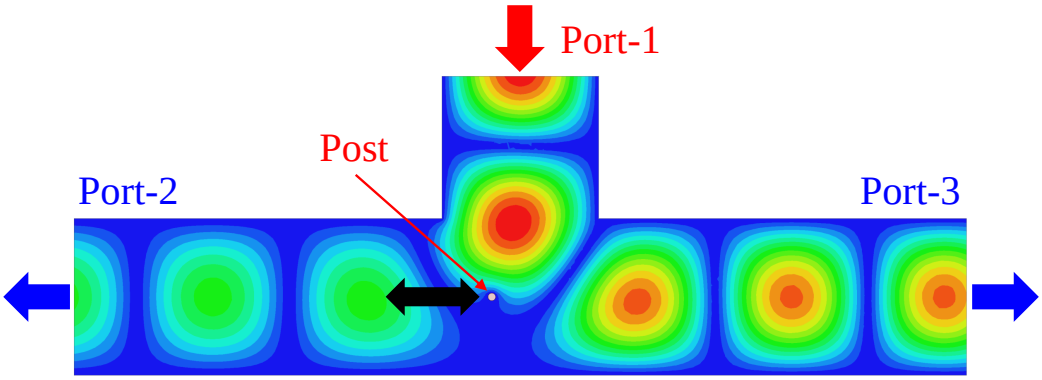

(b) E–field.

Figure 2.14: Model of the long shunt tee integrated with phase shifters of the compact WDS for EXFEL [14].

Figure 2.15 shows the model of an asymmetric shunt tee for the compact WDS for EXFEL. There are two metallic posts placed in the asymmetric shunt tee [14]. By pre–tuning the vertical position of post–1 and the horizontal position of post–2, the power transmitted to each binary cell can be adjusted. For the average power distributed condition, the coupling ratios from input port of asymmetric shunt tee to binary cell are -6.0 dB, -4.77 dB and -3.0 dB for the three asymmetric shunt tees.

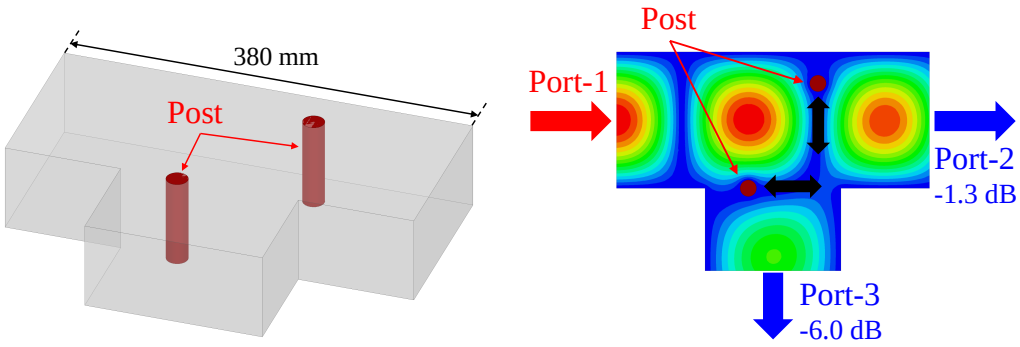

(a) Model. (b) E–field.

Figure 2.15: Model of the asymmetric shunt tee of the compact WDS for EXFEL [14].

Figure 2.16 shows an image of the compact WDS and cryomodule for EXFEL. The advantage of the compact WDS is that it occupies less space. The compact WDS can easily be integrated on the cryomodule. The disadvantage is that the post of the long shunt tee and asymmetric shunt tee need to be pre–tuned. The coupling ratio cannot be changed after it is manufactured. Thus, some SC cavities may not be operated with maximal accelerating gradient.

Figure 2.16: Image of the compact WDS and cryomodule for EXFEL [15].

Chapter 3

Design of Compact LPDS

In this chapter, the motivation behind the development of the compact LPDS and its requirements are introduced. Several candidate models of the compact LPDS were developed. The RF components of the variable hybrid, variable phase shifter, and fixed phase shifter were designed for the compact LPDS.

3.1 Motivation

Referring to the ILC-TDR, the lowest position of the LPDS is lower than the cryomodule. The cryomodule is moved and installed in the tunnel using a cart [1]. If the cryomodule integrated with the LPDS is installed in the tunnel, the cart cannot be removed after the installation process. Due to the limited space of the tunnel, the construction and installation of the LPDS in the tunnel will be difficult and time consuming. It is expected that the compact LPDS will be assembled on the cryomodule on the ground, and the integration of the LPDS and cryomodule will be installed in the tunnel. For this purpose, the vertical length of the compact LPDS must be reduced. For the 250 GeV ILC, the number of RF units and cavities are approximately 236 and 8,000 respectively and the production cost of the RF system is very high. It is also expected that the compact LPDS will reduce the production cost by reducing the number and the dimensions of the RF components.

3.2 Requirements of the Compact LPDS

The ILC-TDR directly indicates the five requirements of the LPDS. Firstly, the adjustment of the power dividing ratio should satisfy the $\pm 20\%$ variation of the accelerating gradient of the SC cavity. Thus, the SC cavity can be

operated close to the quench limit, and the maximal average accelerating gradient of the main LINAC can be achieved. The variable hybrid is used to adjust the input power of the SC cavity in the LPDS from the ILC-TDR. Secondly, the beam should be accelerated on the crest of the RF field to improve the accelerating efficiency of the beam. The variable phase shifter is expected to adjust the phase of the RF field. Thirdly, the variable hybrid and variable phase shifter of the LPDS should be remotely controlled. Fourthly, the geometric distance between adjacent cavities is 1,327 mm and the dimensions of the LPDS should follow this value. Finally, the input power of the LPDS for five cavities is approximately 1.3 MW, with a pulse width of 1.65 ms and a repetition rate of 5 Hz for the average power distributed condition. The power handling capability of the LPDS should be at least 1.3 MW.

The relationship between the accelerating gradient and generator power is useful for the requirements of the LPDS. In the case of the optimal tuning of the SC cavity, the minimal generator power is expressed by the equation (3.1) [17].

$$(P_g)_{min} = E_{acc} \cdot l \cdot I_{b0} \cdot \cos\phi_b \tag{3.1}$$

where E_{acc}, l, I_{b0}, and ϕ_b are the accelerating gradient, effective cavity length, DC component of the beam current, and beam phase, respectively. During the beam operation, the beam current I_{b0}, and beam phase ϕ_b, are constant. The variation of the generator power should be at least $\pm 20\%$ to satisfy the $\pm 20\%$ variation of the accelerating gradient. Considering a given margin, the adjustment of the power dividing ratio of the compact LPDS should be $\pm 25\%$.

When the power dividing ratio is changed by the variable hybrid, the phase changes. The phase shifter should compensate for the phase shift of the variable hybrid to fix the phase difference between adjacent cavities to 90°. Another 15° phase adjusted range is expected for the margin.

The geometric length between adjacent cavities is 1,327 mm, which is $5.75\lambda_0$ at 1.3 GHz. The λ_0 is the wavelength in free space. Thus, the phase of each cavity is 90° delayed relative to the previous cavity along the direction of the beam. Figure 3.1 shows the phase relationship of the cavities for the ILC.

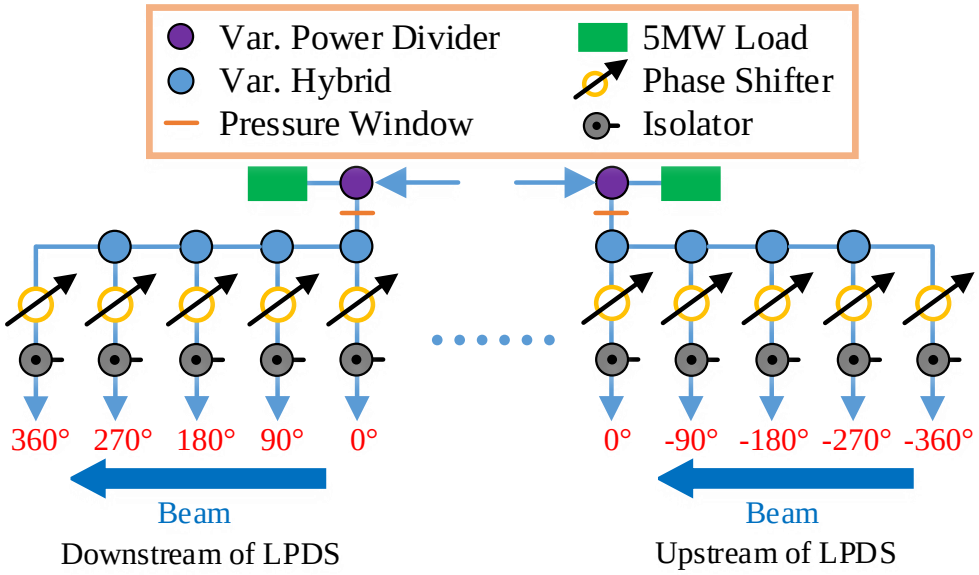

Figure 3.1: Phase relationship of the cavities for the ILC.

The requirements of a compact LPDS is summarized as follows:

- The adjustment of the power dividing ratio should be ±25% by the variable hybrid.
- The RF phase can be adjusted to accelerate beams on the crest of the RF field.
- The phase shifter can compensate for the phase shift of the variable hybrid and supply 15° for the margin.
- The geometric distance between the adjacent output port of the compact LPDS should be 1,327 mm.
- The phase difference between adjacent cavities should be 90°.
- The compact LPDS should be remotely controlled.
- The power handling capability is at least 1.3 MW with a pulse width of 1.65 ms and a repetition rate of 5 Hz.

3.3 Design Concept of Compact LPDS

To address the assembly difficulty, the lowest position of the LPDS should be higher than that of the cryomodule. Thus, the input coupler should be rotated. Considering the structure of the input coupler and a peripheral such as a vacuum tube, the direction of the input coupler should be vertical and not horizontal. Thus, the input coupler will be rotated by 180°. The power flow direction to the input coupler is changed from above to below. To reduce the vertical length of the LPDS to lower the center of gravity, the variable phase shifter is changed from a vertical line to a horizontal line [16]. In the case of a variable phase shifter that is set vertically, it can only adjust the phase of one cavity and the phase shift of the variable hybrid accumulated to the next cavity. This will significantly increase the required phase adjusted range of the variable phase shifter. For example, if the maximal phase shift of the variable hybrid is 20°, the required phase adjusted range of the variable phase shifter should be at least 80° for a LPDS for 5 cavities. In the case of a variable phase shifter that is set horizontally, the phase adjustment of the variable phase shifter is effective for all the following cavities in the same LPDS. The variable hybrid and variable phase shifter can be regarded as an integration. Every time the variable hybrid is adjusted, the variable phase shifter is also adjusted to compensate for the phase shift. Thus, the phase of the following cavities is not changed. If the maximal phase shift of the variable hybrid is 20°, the required phase adjusted range of the variable phase shifter is only 20°. It is evident that the phase adjusted range is positively correlated to the geometric length of the variable phase shifter. By moving the variable phase shifter from the vertical position to the horizontal position, the required geometric length of variable phase shifter is reduced and the LPDS can be compact. Figure 3.2 shows the candidate concepts for the compact LPDS. These concepts will be discussed later. Fig 3.3 shows the PDS based on the compact LPDS.

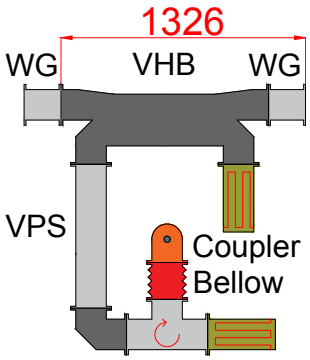

(a) LPDS in ILC-TDR.

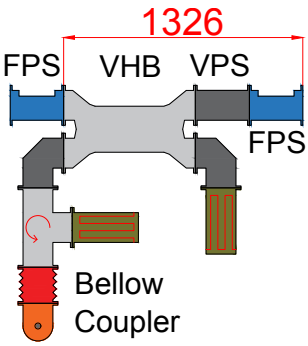

(b) #1 concept for compact LPDS.

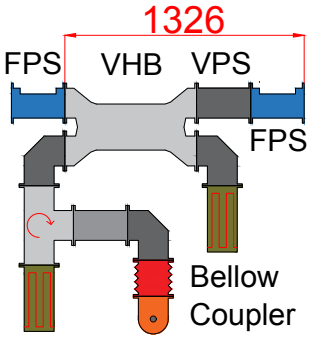

(c) #2 concept for compact LPDS.

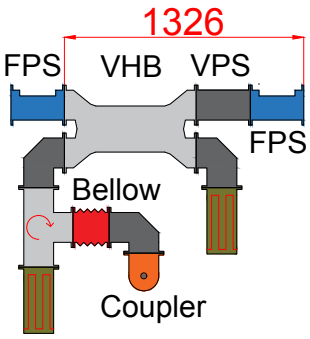

(d) #3 concept for compact LPDS.

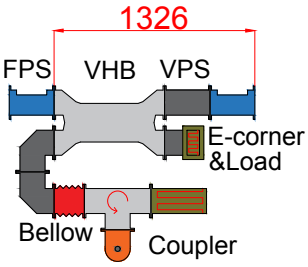

(e) #4 concept for compact LPDS.

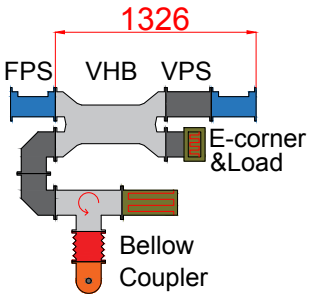

(f) #5 concept for compact LPDS.

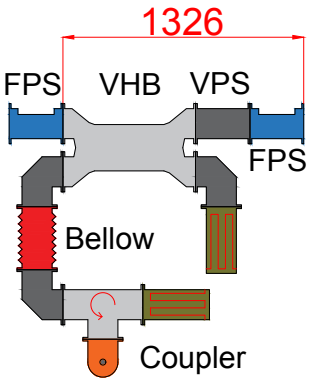

(g) #6 concept for compact LPDS.

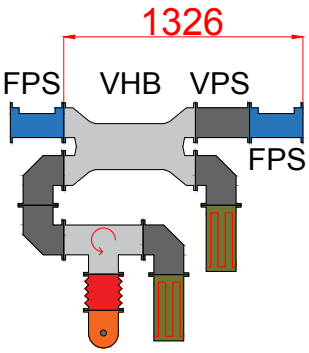

(h) #7 concept for compact LPDS.

Figure 3.2: Candidate concepts for the compact LPDS. VHB is a variable hybrid. VPS is a variable phase shifter. FPS is a fixed phase shifter. WG is a straight waveguide.

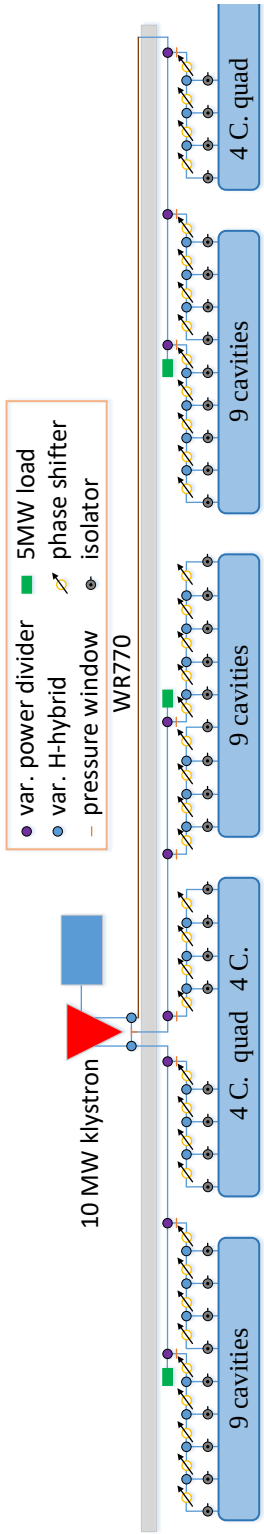

Figure 3.3: The PDS based on the compact LPDS.

The #1 concept has the least number of RF components. Figure 3.4 shows the compact LPDS for the five cavities based on the #1 concept [28]. There are nine 9-cell cavities in one cryomodule, but there is not enough space for the next compact LPDS for four cavities. Two solutions are considered. The first solution is to rotate the first variable phase shifter that is closest to the power divider from the horizontal direction to the vertical direction, and to use one E-corner to rotate the dummy load of the power divider. Figure 3.5 shows the modified compact LPDS for five cavities based on the #1 concept. The height of the compact LPDS and PDS is increased. The second solution involves another concept and may reduce the height of the center of gravity of the compact LPDS. For the first solution, the advantage is a reduction of the number of RF components, and the disadvantage is an increase in the height of the compact LPDS and PDS. For the second solution, the advantage is a reduction of the height of the compact LPDS and PDS, and the disadvantage is at least an additional H-corner is necessary for each cavity.

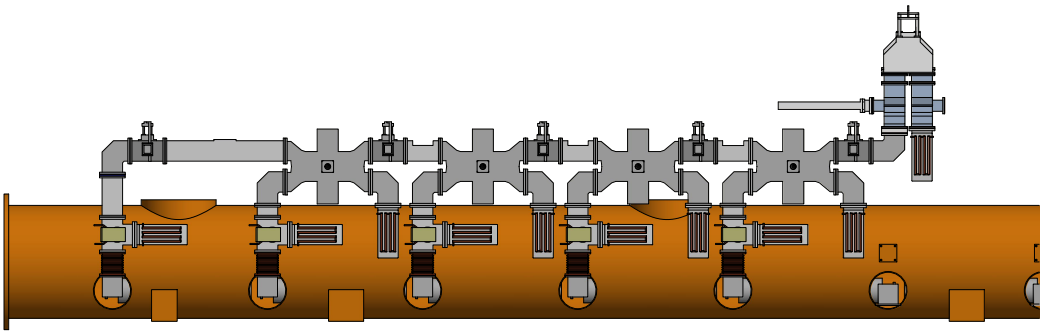

Figure 3.4: Compact LPDS for five cavities based on the #1 concept [28].

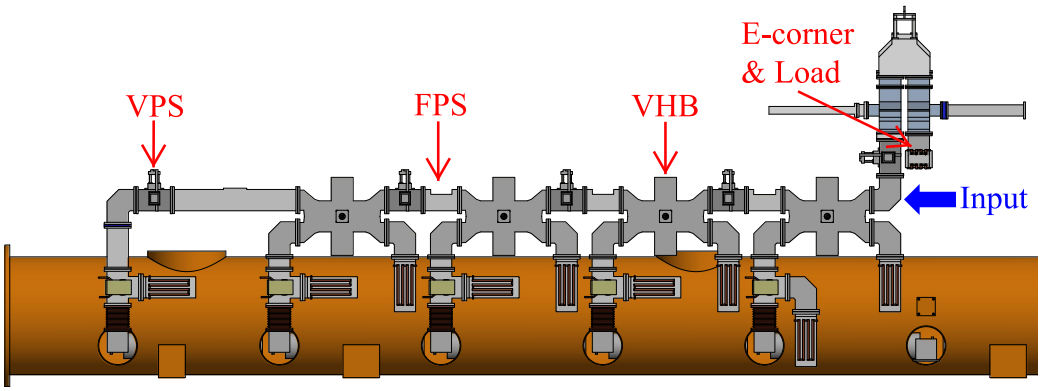

Figure 3.5: Modified compact LPDS for five cavities based on the #1 concept.

The #2 and #3 concepts can satisfy the space requirement and reduce the height of the compact LPDS. Figure 3.6 shows the compact LPDS for five cavities based on the #3 concept. The number of RF components required for the #3 concept is less than that required for #2 concept for one straight waveguide. The height of the #3 concept is also less than that of the #2 concept. In the case of the #3 concept, the bellow is not directly connected to the input coupler. The lowest position of #3 is the dummy load, and may be lower than the cryomodule, which requires installation of the dummy load in the tunnel after the installation of the compact LPDS and the cryomodule.

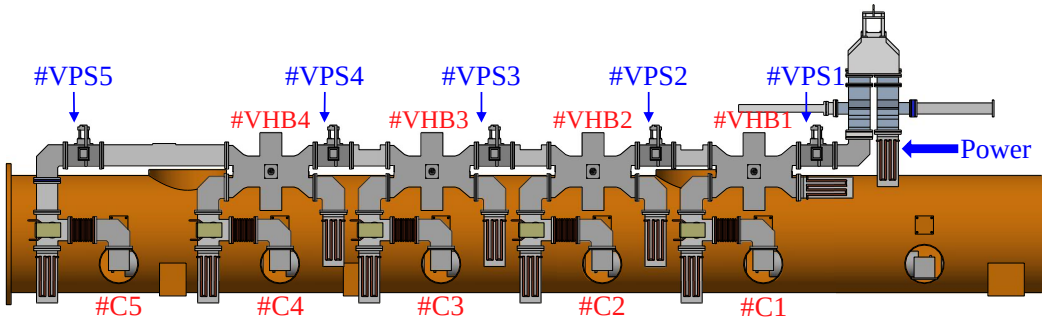

Figure 3.6: Compact LPDS for five cavities based on the #3 concept.

The #4 and #5 concepts require the E-corner to connect the variable hybrid and dummy load, thus, more horizontal space is needed. The height of #4 is less than that of #5, but it requires that the bellow is not directly connected to the input coupler. Figure 3.7 shows the compact LPDS for 5 cavities based on the #4 concept. The support system of the compact

LPDS may be more complicated. The #6 concept requires a longer bellow to generate enough space for the two dummy loads. The #7 concept requires the most H-corners of all the seven concepts.

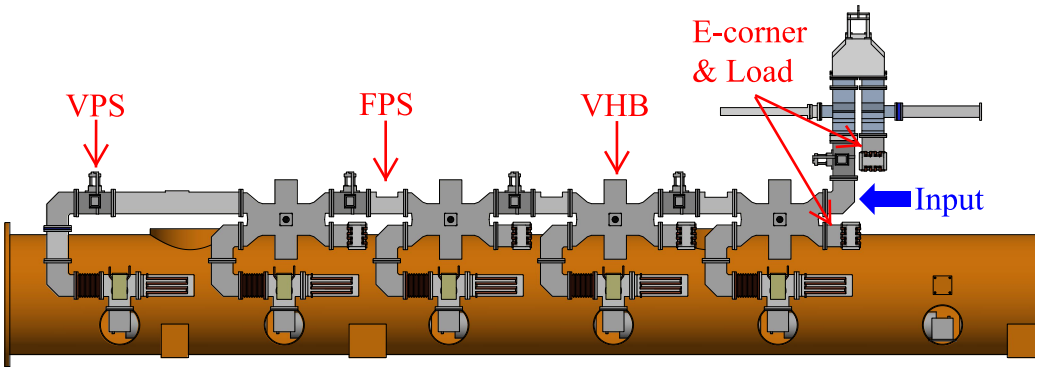

Figure 3.7: Compact LPDS for 5 cavities based on the #4 concept.

Based on the preceding discussion, the first choice is the #1 concept because it requires the least RF components, the second choice is the #4 or #5 concept because it facilitates horizontal space and a possible support system, and the third choice is the #2 or #3 concept.

3.4 Design of RF Components for the Compact LPDS

To realize a compact LPDS, a compact variable hybrid and a compact variable phase shifter are designed. In addition, fixed phase shifters are designed to adjust the phase difference between adjacent cavities for beam acceleration.

3.4.1 Phase Shifter of the Plate and the Fin Type

The typical waveguide phase shifter is a straight waveguide with an inserted movable conductor to change the guide wavelength λ_g. The phase can be shifted by varying the wavelength. For the traveling wave system, only the TE_{10} mode, which is the fundamental mode, is usually generated in the rectangular waveguide. The λ_g for TE_{10} is expressed with the permittivity ϵ, the permeability μ, the RF frequency f, and the width of the cross section of the waveguide a [8].

$$\lambda_g = \frac{2\pi}{\sqrt{(4\pi^2 f^2 \epsilon\mu) - \left(\frac{\pi}{a}\right)^2}} \tag{3.2}$$

In the case of 1.3 GHz RF frequency, the waveguide is the WR650 type. The width a and height b of the cross section are 165.1 mm and 82.5 mm, respectively. The minimal value of a is 115.3 mm, otherwise, the TE_{10} will be cut off. The λ_g can be changed with a variation of a. The simplest approach is to insert a movable conductive plate into the waveguide. Figure 3.8 shows a plate type model of a variable phase shifter. In the simulated model, the movable plate has a thickness of 1 mm, a height H and a Length L. The thin plate will be moved along the width of the waveguide to change the effective width. There are two reflection points in this variable phase shifter, which are the start point and end point of the plate. The superposition of the two reflected waves is the total reflection of the variable phase shifter. The phase difference between the two reflected waves is dependent on the length of the plate and the moving distance of the plate. Thus, the total reflection changes when the plate is moved. Total reflection can be reduced by judicious selection of the height and length of the plate.

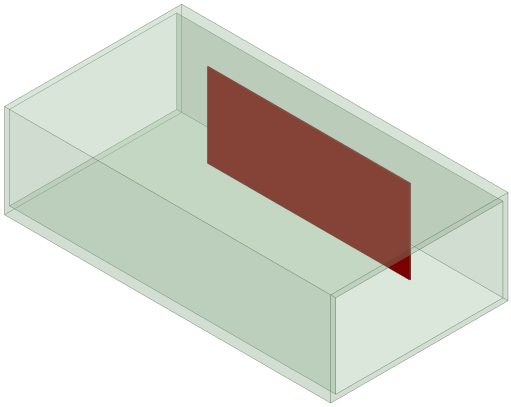

(a) Simulated model.

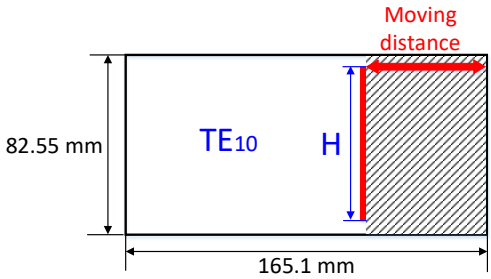

(b) Front view.

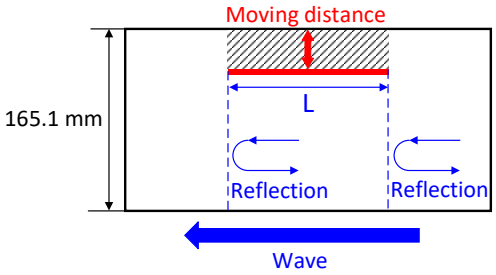

(c) Top view.

Figure 3.8: Model of the plate type variable phase shifter.

Figure 3.9 shows the simulated $|S_{11}|$ and S_{21} phase of the plate type variable phase shifter. The height of plate (H) is chosen as 82.55mm, 70 mm, 60 mm, 50 mm and 40 mm. The length of plate (L) is optimized such that the $|S_{11}|$ is less than -30 dB within the maximal moving range of the plate. For the case when H is 82.55 mm, the height of the plate is the same as the height of the waveguide. The effective width of the waveguide decreases as the plate is moved towards the center of the waveguide. This leads to a decrease in the propagation constant β and an increase of the guide wavelength λ_g. Thus, the transmitted phase is increased as the plate is moved toward the center of the waveguide. For the case when H is less than 82.55 mm, the waveguide behaves similar to a coaxial cable as the plate is moved towards the center of the waveguide. The propagation constant of a coaxial cable is larger than that of a waveguide. However, the guide wavelength of a coaxial cable is smaller than that of a waveguide. Thus, the transmitted phase is decreased as the plate is moved towards the center of the waveguide.

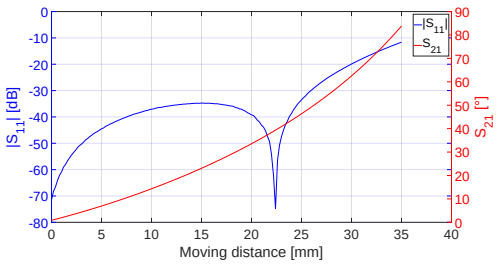

(a) H=82.55 mm, L=159 mm. The transmitted phase is shifted from 0.9° to 49.0° and $|S_{11}|$ is less than -30 dB as the plate is moved from 0.0 mm to 25.9 mm.

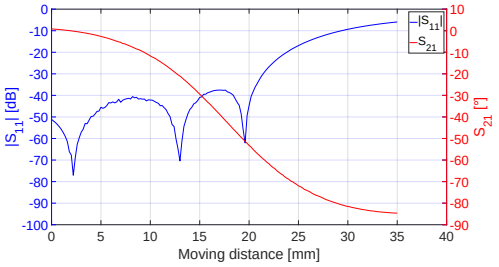

(b) H=70 mm, L=187 mm. The transmitted phase is shifted from 0.8° to −59.4° and $|S_{11}|$ is less than -30 dB as the plate is moved from 0.0 mm to 21.4 mm.

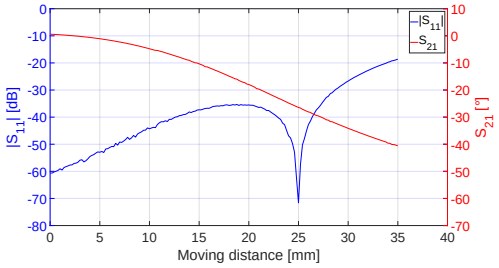

(c) H=60 mm, L=168 mm. The transmitted phase is shifted from 0.6° to −32.1° and $|S_{11}|$ is less than -30 dB as the plate is moved from 0.0 mm to 28.6 mm.

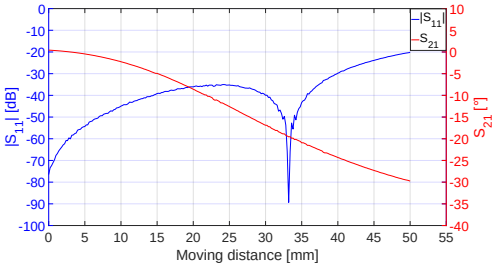

(d) H=50 mm, L=159 mm. The transmitted phase is shifted from 0.4° to −24.2° and $|S_{11}|$ is less than -30 dB as the plate is moved from 0.0 mm to 39.8 mm.

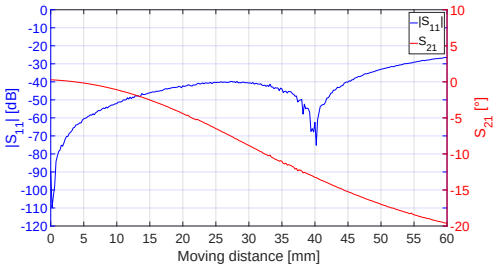

(e) H=40 mm, L=156 mm. The transmitted phase is shifted from 0.3° to −18.0° and $|S_{11}|$ is less than -30 dB as the plate is moved from 0.0 mm to 53.5 mm.

Figure 3.9: Simulated $|S_{11}|$ and S_{21} phase of the plate type variable phase shifter.

Table 3.1 shows the simulated result of the plate type variable phase shifter. When H is 82.55 mm, L is 159 mm to reduce the reflection. The transmitted phase is shifted from 0.9° to 49° and $|S_{11}|$ is less than -30 dB as the plate is moved from 0.0 mm to 25.9 mm. The phase shifted range is 48.1° and the average phase shifted rate is 1.9 [°/mm].

When H is 70 mm, L is 187 mm to reduce the reflection. The transmitted phase is shifted from 0.8° to −59.4° and $|S_{11}|$ is less than -30 dB as the plate is moved from 0.0 mm to 21.4 mm. The phase shifted range is 60.2° and the average phase shifted rate is 2.8 [°/mm].

When H is 60 mm, L is 168 mm to reduce the reflection. The transmitted phase is shifted from 0.6° to −32.1° and $|S_{11}|$ is less than -30 dB as the plate is moved from 0.0 mm to 28.6 mm. The phase shifted range is 32.7° and the average phase shifted rate is 1.1 [°/mm].

When H is 50 mm, L is 159 mm to reduce the reflection. The transmitted phase is shifted from 0.4° to −24.2° and $|S_{11}|$ is less than -30 dB as the plate is moved from 0.0 mm to 39.8 mm. The phase shifted range is 24.6° and the average phase shifted rate is 0.6 [°/mm].

For the case when H is 40 mm, L is 156 mm to reduce the reflection. The transmitted phase is shifted from 0.3° to −18.0° and $|S_{11}|$ is less than -30 dB as the plate is moved from 0.0 mm to 53.5 mm. The phase shifted range is 18.3° and the average phase shifted rate is 0.3 [°/mm].

Table 3.1: Simulated result of the plate type variable phase shifter.

H	82.55 mm	70 mm	60 mm
L	159 mm	187 mm	168 mm
Moving range ($\|S_{11}\| \leq -30$dB)	25.9 mm	21.4 mm	28.6 mm
Phase shifted range	49.9°	60.2°	32.7°
Average phase shifted rate	1.9 [°/mm]	2.8 [°/mm]	1.1 [°/mm]
H	50 mm	40 mm	
L	159 mm	156 mm	
Moving range ($\|S_{11}\| \leq -30$dB)	39.8 mm	53.5 mm	
Phase shifted range	24.6°	18.3°	
Average phase shifted rate	0.6 [°/mm]	0.3 [°/mm]	

The simulated results indicate that a decrease of H leads to a smaller phase shifted range and a slower average phase shifted rate. Thus, it is difficult to simultaneously achieve a large phase shifted range and a slow average phase shifted rate for the plate type variable phase shifter. The phase shift should not be too sensitive to the moving distance of the plate. In the case of the compact LPDS, the phase shifted range is expected to be more than 35°. In addition, an average phase shifted rate of less than 1 [°/mm] is be a good parameter. The plate type variable phase shifter cannot satisfy the requirements of the compact LPDS.

The fin type was developed to address this problem [9]. Figure 3.10 shows a model of the fin. The fin consists of one cylinder, two cones, and two

hemispheres. The fin is symmetrical. There are multi-reflection planes on the surface of the cone. Reflection can be reduced by optimizing the radius of the top and bottom circle of the cone, in addition to the length of the cone. The hemisphere is used to reduce the E-field. The simulated result for the fin type variable phase shifter will be discussed in subsection 3.4.3.

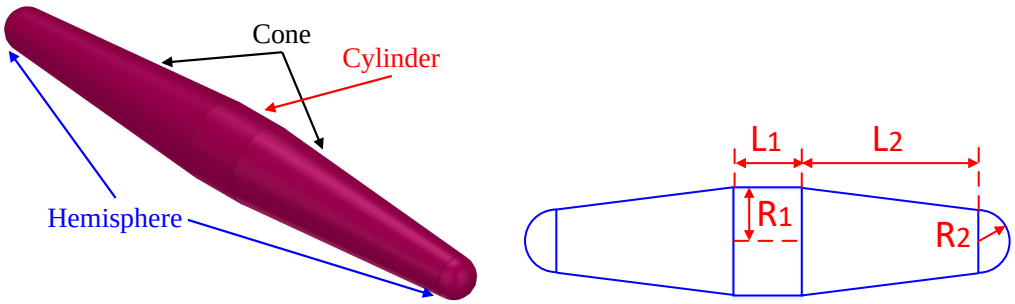

Figure 3.10: Model of fin.

3.4.2 Design of Variable Hybrid

The hybrid is a 4-port RF component that can divide the input power from one port to three ports. Figure 3.11 shows the basic model of hybrid. The power is inputted from port-1 and outputted from port-2, port-3 and port-4. Only the TE_{10} mode is generated in the four ports of the hybrid. There are TE_{10} and TE_{20} modes in the central box of the hybrid [8]. L and W are the length and width of the central box, respectively. For an ideal hybrid, no power is transmitted from port-1 to port-4.

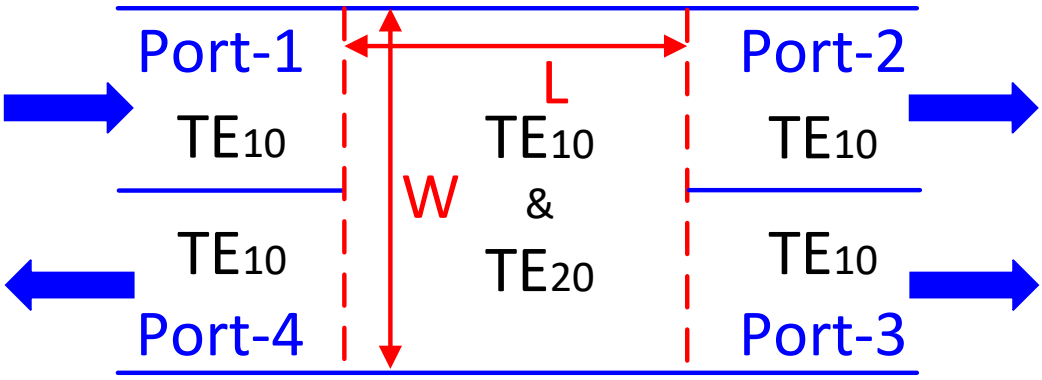

Figure 3.11: Basic model of the hybrid.

Figure 3.12 shows the wave within the hybrid. The incident wave with the TE_{10} mode from port-1 and an amplitude of 2A is equal to the superposition of two parts [21]. The first part is the incident wave with the TE_{10} mode and an amplitude of A from port-1 and port-4 with the same phase. The second part is the incident wave with the TE_{10} mode and an amplitude of A from port-1 and port-4 with a phase difference of 180°. The first part will be transformed to the TE_{20} mode with an amplitude of A in the central box. The second part will maintain the TE_{10} mode with an amplitude of A in the central box. The mixture of the TE_{10} mode and the TE_{20} mode will generate the TE_{10} mode in port-2 and port-3, with a phase difference of 90°.

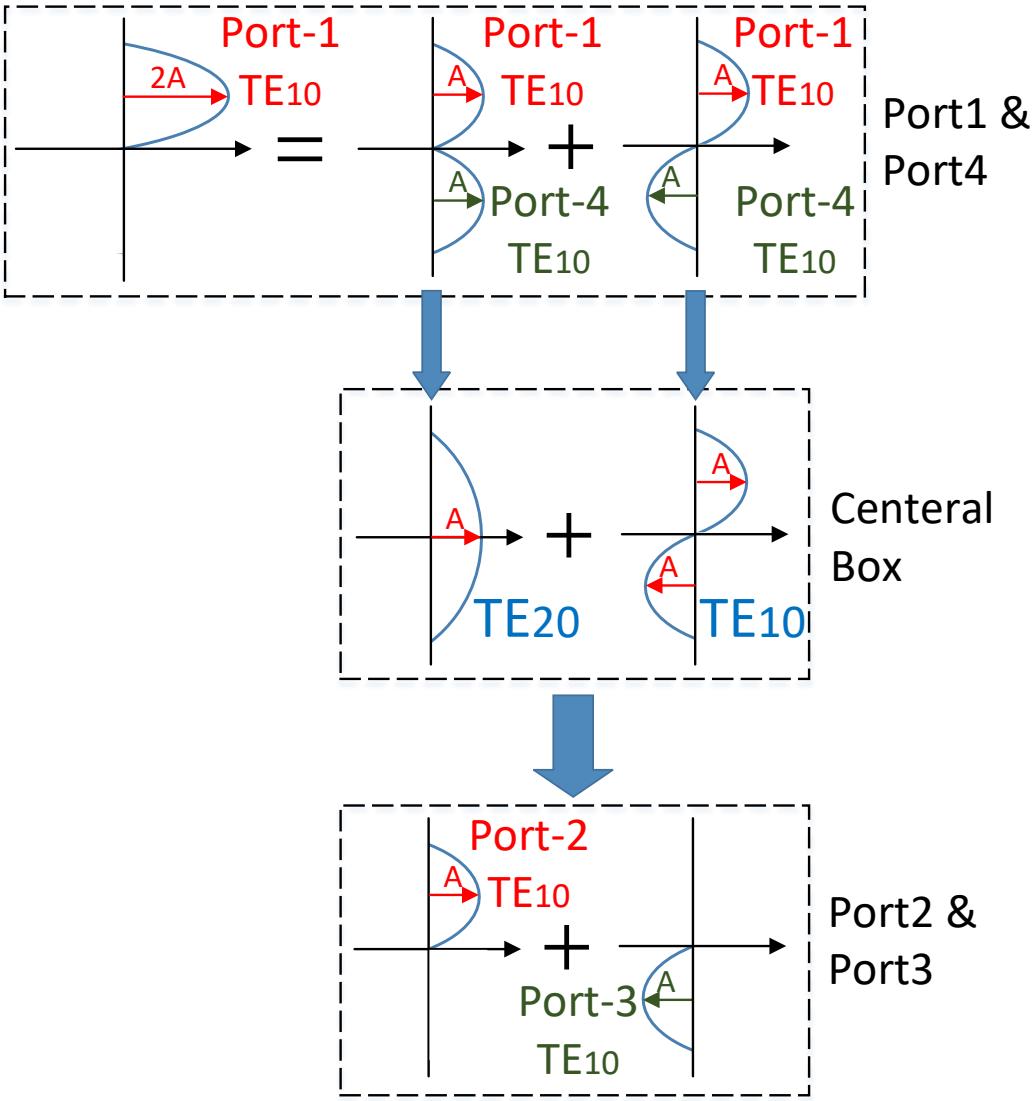

Figure 3.12: Wave within the hybrid.

Based on the Fig. 3.12, the power dividing ratio from port-1 to port-2 and port-3 can be expressed.

$$
\begin{aligned}
|\mathrm{S}_{21}| &= \frac{P_2}{P_1} = \left|\frac{E_2}{E_1}\right|^2 = \left(\cos\frac{\theta}{2}\right)^2 \\
|\mathrm{S}_{31}| &= \frac{P_3}{P_1} = \left|\frac{E_3}{E_1}\right|^2 = \left(\sin\frac{\theta}{2}\right)^2 \\
\frac{E_3}{E_2} &= \left(\tan\frac{\theta}{2}\right)\mathrm{e}^{-\mathrm{j}\frac{\pi}{2}} \\
\theta &= (\beta_{10} - \beta_{20})\,L
\end{aligned}
\tag{3.3}
$$

β_{10} and β_{20} are the propagation constants of the TE_{10} mode and TE_{20} mode, respectively. From equation 3.3, the phase difference between $|\mathrm{S}_{21}|$ and $|\mathrm{S}_{31}|$ is 90°. The power dividing ratio is determined using θ.

The variable hybrid (VHB) is a type of hybrid that can change the power dividing ratio. The power dividing ratio can be changed based on the variation of θ. Figure 3.13 shows the variation of β_{10} and β_{20} compared to W. The variation rate between the propagation constant β and the width of the waveguide W is different for the TE_{10} and TE_{20} modes. θ can be adjusted by changing W. Thus, the power dividing ratio also changes.

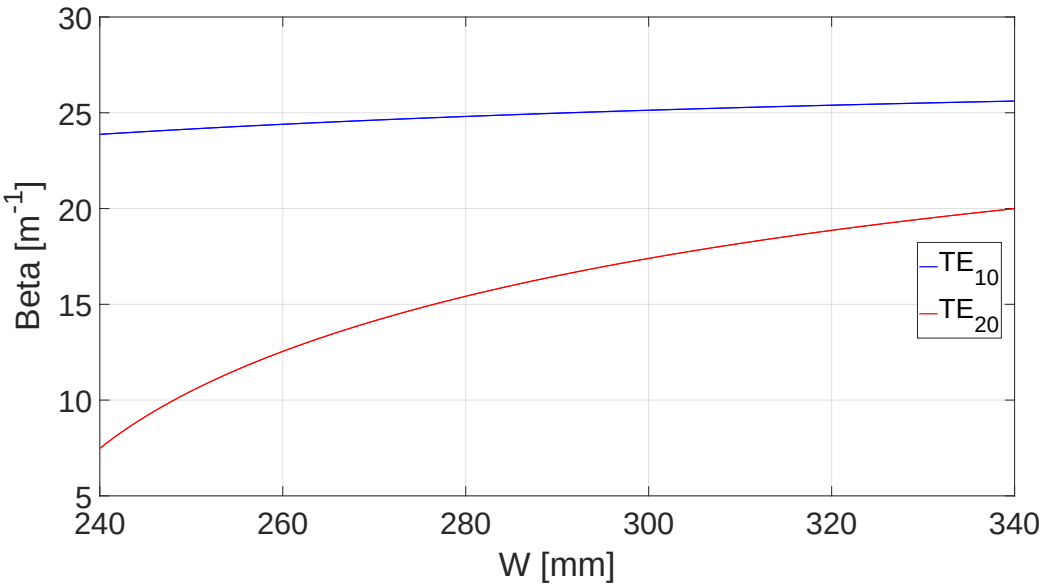

Figure 3.13: Variation of β_{10} and β_{20} compared to W.

As shown in section 3.2, one of the requirements is that the compact LPDS as the input power source of each cavity should have a variation of

±25% to achieve a maximal accelerating gradient. Table 3.2 shows the required adjusted range of the power coupling ratio ($|S_{31}|$) for four variable hybrids (#VHB1 ∼ #VHB4) based on the power distributed margin of ±25%. For the average power distributed condition, the power coupling ratios from #VHB1 to #VHB4 are -6.99 dB, -6.02 dB, -4.77 dB, and -3.01 dB, respectively. In the case of #VHB1, a power coupling ratio of -8.84 dB is calculated as the power of #CAV1 is deviated by -25%, and the power of #CAV2 to #CAV5 is deviated by +25%. The other value in the Table 3.2 can be calculated using the same approach. Thus, the adjusted range of the power coupling ratio ($|S_{31}|$) of the variable hybrid should be from -8.84 dB to -2.04 dB.

Table 3.2: Required adjusted range of the power coupling ratio ($|S_{31}|$) for four variable hybrids (#VHB1 ∼ #VHB4) based on the power distributed margin of ±25%.

$\|S_{31}\|$	Average	-25%	+25%
#VHB1	-6.99 dB (20.0%)	-8.84 dB (13.0%)	-5.31 dB (29.4%)
#VHB2	-6.02 dB (25.0%)	-7.78 dB (16.7%)	-4.47 dB (35.7%)
#VHB3	-4.77 dB (33.3%)	-6.37 dB (23.1%)	-3.42 dB (45.5%)
#VHB4	-3.01 dB (50.0%)	-4.26 dB (37.5%)	-2.04 dB (62.5%)

By considering the fin type variable phase shifter, a variable hybrid can be designed. Figure 3.14 shows the model of a variable hybrid. Its length is decreased from 1100 mm to 730 mm [9] [28]. Two identical metallic fins are moved symmetrically, and two robs are used to support each fin. Four identical metallic posts are set symmetrically in the variable hybrid to reduce the reflection of each port. The shape of the two fins, and the position and radius of the posts are optimized to reduce the reflection of each port and the power transmitted from port-1 to port-4. The moving distance is defined as the minimal distance between the cylinder of the fin and the wall of the waveguide.

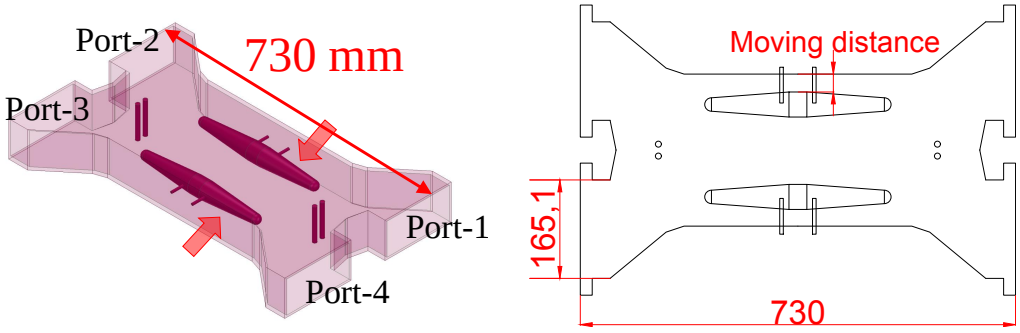

(a) Simulated model. (b) Top view

Figure 3.14: Model of the variable hybrid.

Figure 3.15 shows the simulated S parameters of the variable hybrid. $|S_{31}|$ is changed from -8.84 dB to -2.04 dB and $|S_{21}|$ is changed from -0.62 dB to -4.31 dB as the fin is moved from 1.1 mm to 14.7 mm. The maximal $|S_{11}|$ and $|S_{41}|$ are -30.00 dB and -29.60 dB respectively for this movement of the fin.

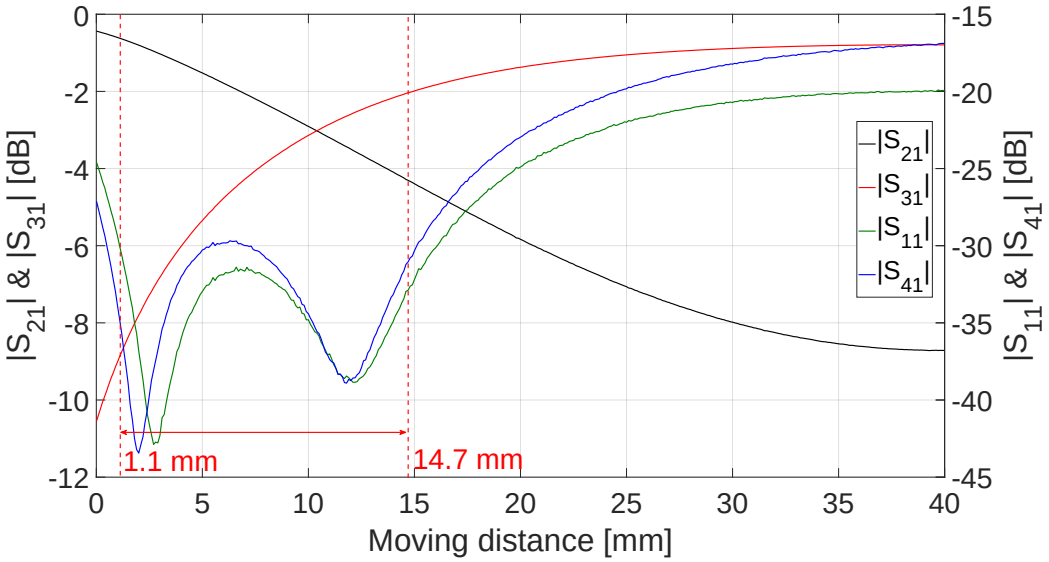

Figure 3.15: Simulated S parameter of the variable hybrid. The $|S_{31}|$ is changed from -8.84 dB to -2.04 dB, $|S_{11}|$ is less than -30.00 dB and $|S_{41}|$ is less than -29.60 dB as the fin is moved from 1.1 mm to 14.7 mm.

Figure 3.16 shows the simulated phase of S_{21} and S_{31} of the variable hybrid. The maximal phase shift of S_{31} of the variable hybrid is 17.00° when $|S_{31}|$ is adjusted from -2.04 dB to -4.26 dB for #VHB4.

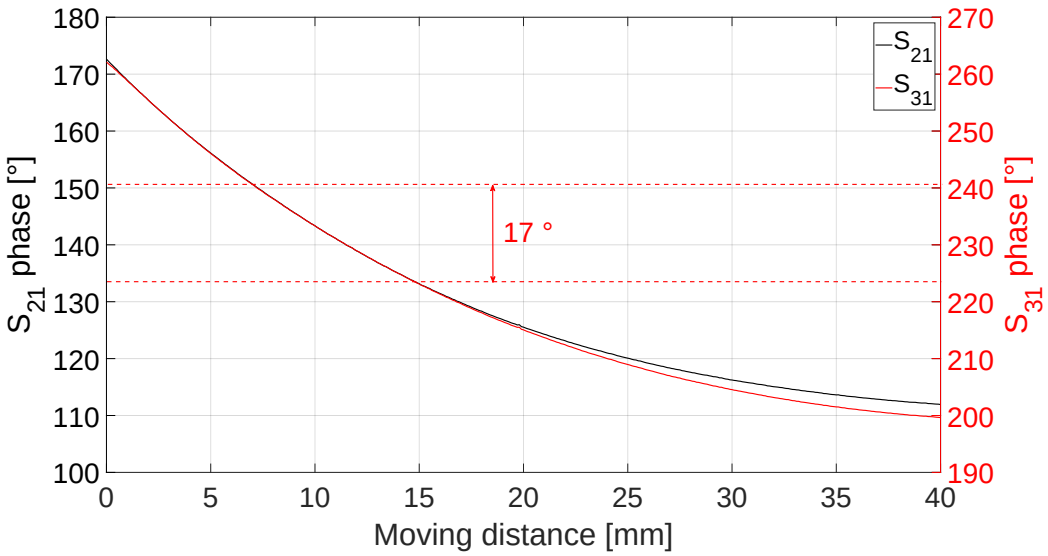

Figure 3.16: Simulated phase of S_{21} and S_{31} of variable hybrid. The maximal phase shift is 17° while the $|S_{31}|$ is changed of ±25%.

Figure 3.17 shows the simulated phase difference between S_{21} and S_{31} of variable hybrid. The phase difference between S_{21} and S_{31} is from 89.89° to 90.04° while the fin is moved from 1.1 mm to 14.7 mm. The maximal deviation between this phase difference and 90° is 0.11°.

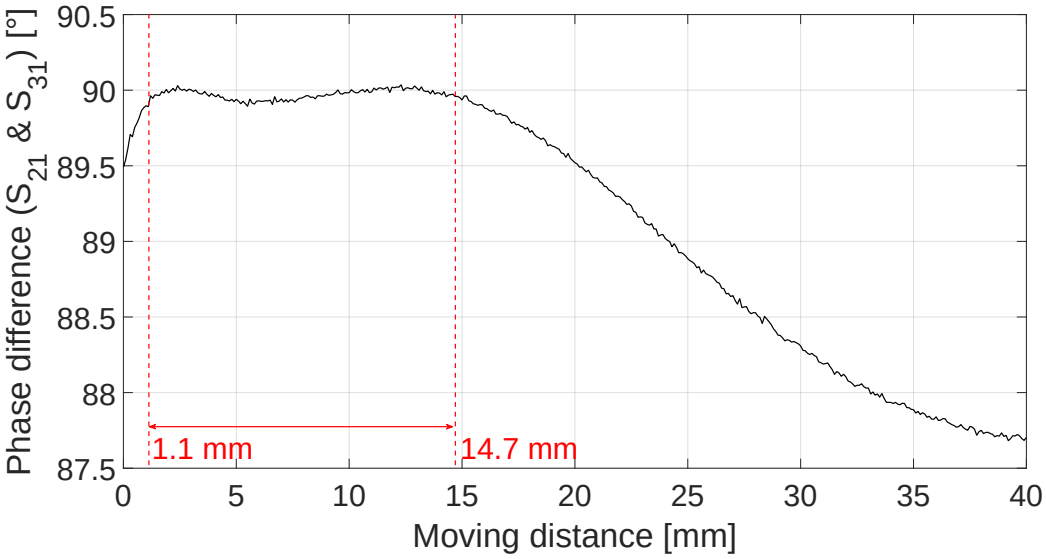

Figure 3.17: Simulated phase difference between S_{21} and S_{31} of variable hybrid.

Figure 3.18 shows the simulated maximal E-field of the variable hybrid compared to the moving distance of the fin. The maximal E-field in the variable hybrid is 0.93 MV/m while the fin is moved from 1.1 mm to 14.7 mm.

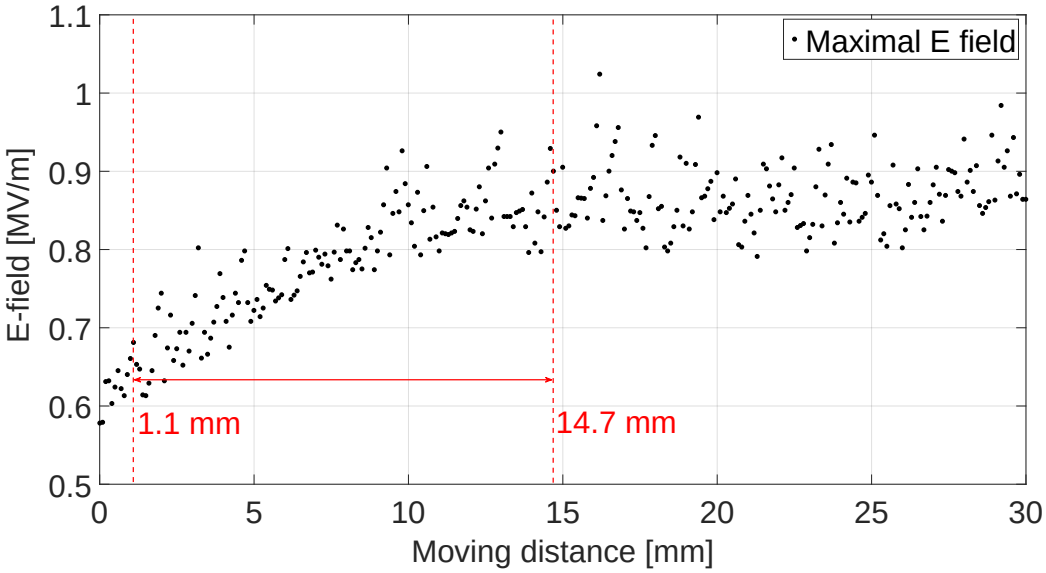

Figure 3.18: Simulated maximal E-field of the variable hybrid compared to the moving distance of the fin. The maximal E-field in the variable hybrid is 0.93 MV/m while the fin is moved from 1.1 mm to 14.7 mm

Figure 3.19 shows the simulated E field in the variable hybrid. The power dividing ratio is changed as the fin is moved. The phase difference between the output signal of port-2 and port-3 is approximately 90°. The position of the maximal E field in the variable hybrid is in the vicinity of the post and the fin near the input port.

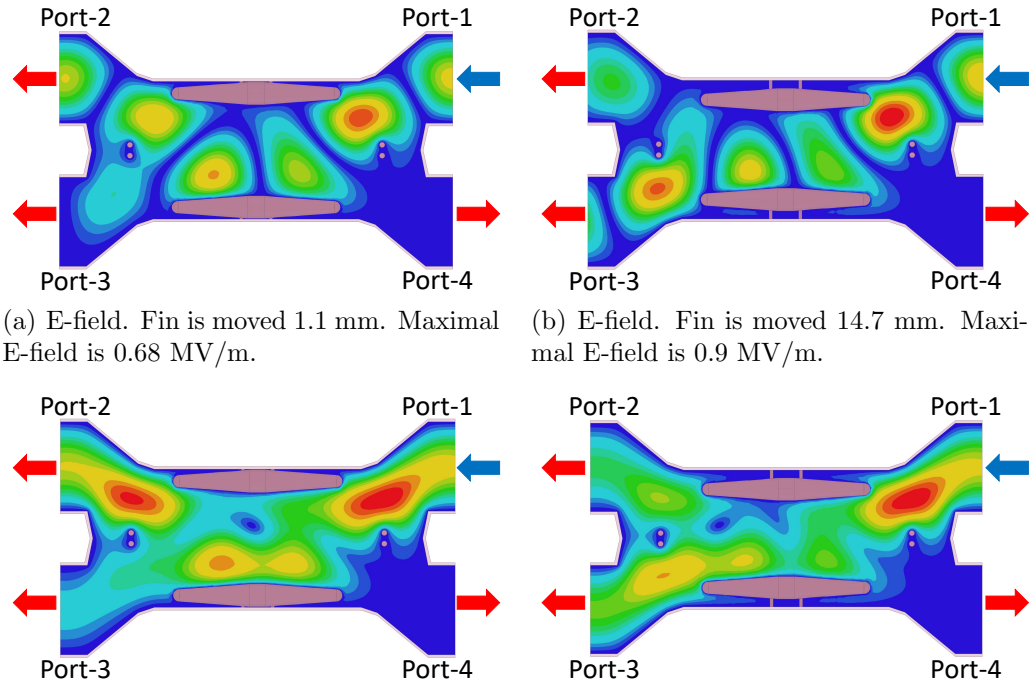

(a) E-field. Fin is moved 1.1 mm. Maximal E-field is 0.68 MV/m.

(b) E-field. Fin is moved 14.7 mm. Maximal E-field is 0.9 MV/m.

(c) Magnitude of E-field. Fin is moved 1.1 mm.

(d) Magnitude of E-field. Fin is moved 14.7 mm.

Figure 3.19: Simulated E field in the variable hybrid.

Table 3.3 shows the simulated S parameter of the variable hybrid. The simulated result of the variable hybrid can satisfy the requirements of the compact LPDS.

Table 3.3: Simulated S parameter of the variable hybrid.

Length	730 mm
Moving range of fin	1.1 mm $\sim$ 14.7 mm
$\lvert S_{31} \rvert$	-8.84 dB $\sim$ -2.04 dB
$\lvert S_{21} \rvert$	-0.62 dB $\sim$ -4.31 dB
Maximal $\lvert S_{11} \rvert$	-30.00 dB
Maximal $\lvert S_{41} \rvert$	-29.60 dB
Maximal phase shift of S_{31}	17.00°
Phase difference between S_{21} and S_{31}	89.89° $\sim$ 90.04°
Maximal E-field	0.93 MV/m

3.4.3 Design of the Variable Phase shifter

The variable phase shifter of the compact LPDS is designed to compensate for the phase shift of the variable hybrid. This phase shift of the variable hybrid is 17°. Considering a margin of 15°, the required phase shifted length of the variable phase shifter is at least 32°. The reflection of the variable phase shifter is expected to be less than -30 dB. Table 3.4 summarizes the requirements of the variable phase shifter.

Table 3.4: Requirement of the variable phase shifter.

Phase shifted range	$\geq 32°$
Reflection	$\leq$ -30 dB

The design of the fin type variable phase shifter is presented in subsection 3.4.1. Figure 3.20 shows the simulated model of the variable phase shifter. The geometric length of this variable phase shifter decreased from 600 mm (ILC-TDR) to 300 mm [9] [28]. One metallic fin is supported by two metallic robs. The fin is moved to shift the transmitted phase. The shape of the fin is optimized to extend the phase shifted range and reduce reflection.

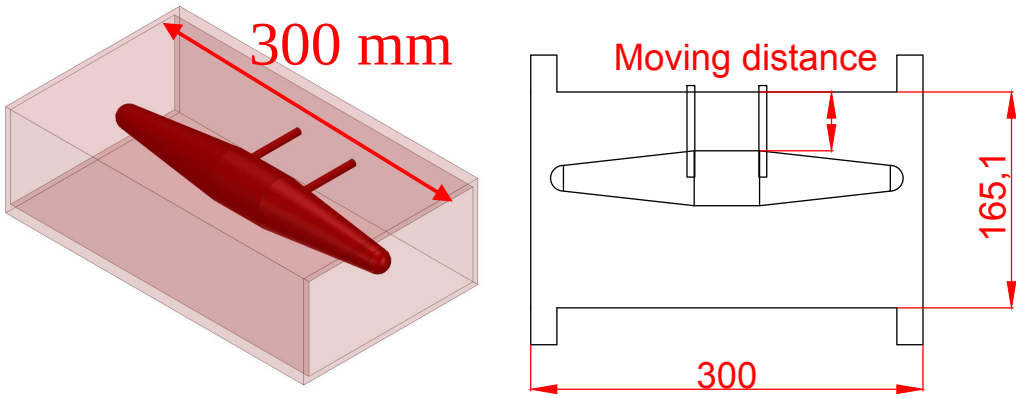

(a) Simulated model. (b) Top view

Figure 3.20: Model of the variable phase shifter.

Figure 3.21 shows the simulated transmitted phase (S_{21}) and reflection ($|S_{11}|$) of the variable phase shifter. The transmitted phase is shifted from 35.9° to $-1.9°$ and the reflection is less than -30.00 dB as the fin is moved from 0.0 mm to 46.0 mm. The phase shifted length is 37.8°.

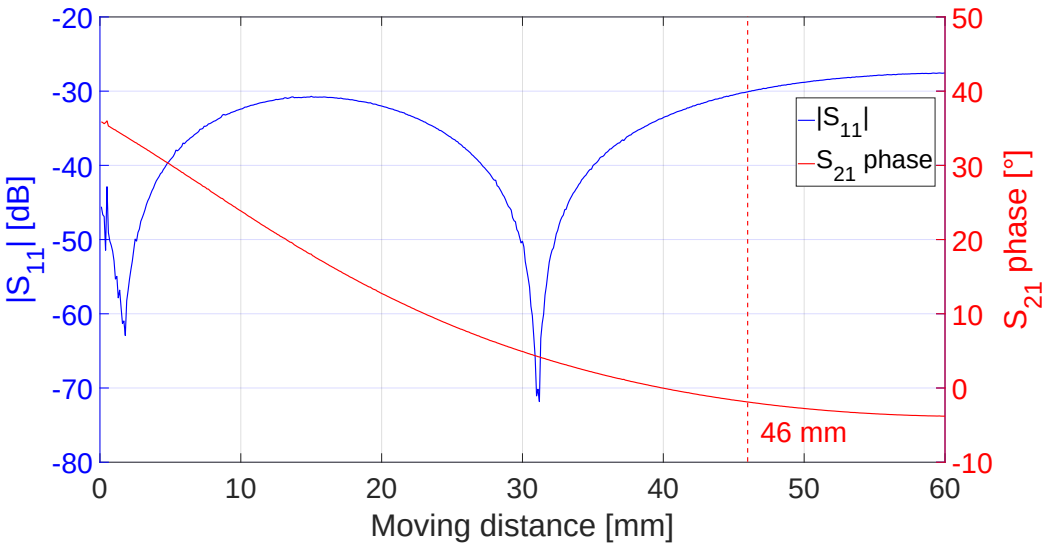

Figure 3.21: Simulated transmitted phase (S_{21}) and reflection ($|S_{11}|$) of the variable phase shifter. The transmitted phase is shifted from 35.9° to −1.9° and the reflection is less than -30.00 dB as the fin is moved from 0.0 mm to 46.0 mm.

Figure 3.22 shows the simulated maximal E-field of the variable phase shifter compared to the moving distance of the fin. The maximal E-field is 1.08 MV/m while the fin is moved from 0.0 mm to 46.0 mm.

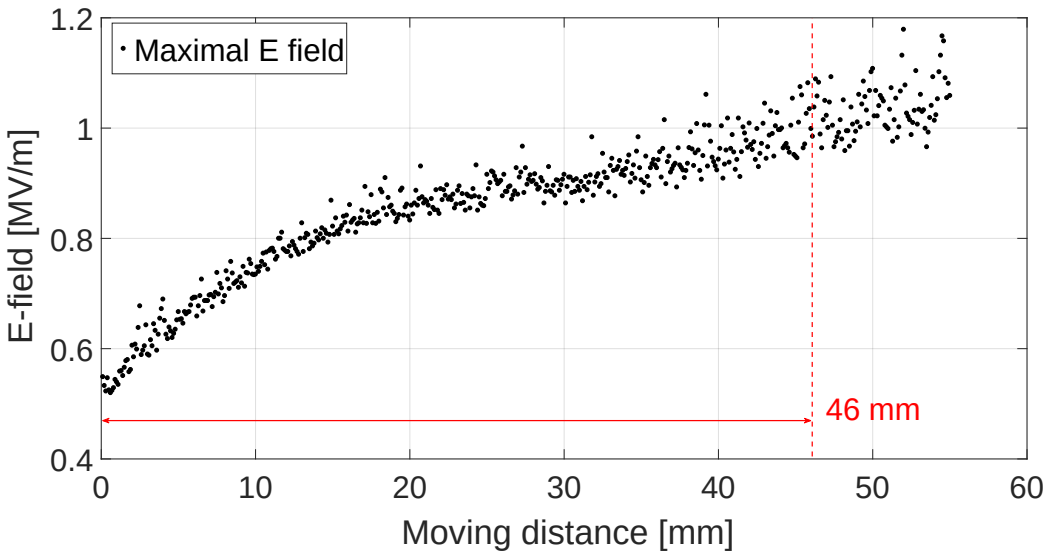

Figure 3.22: Simulated maximal E-field of the variable phase shifter compared to the moving distance of fin. The maximal E-field in the variable phase shifter is 1.08 MV/m while the fin is moved from 0.0 mm to 46.0 mm

Figure 3.23 shows the simulated E-field in the variable phase shifter. The phase is shifted as the fin is moved. The position of the maximal E-field in the variable hybrid is in the vicinity of the fin when it is closed to the center of the waveguide.

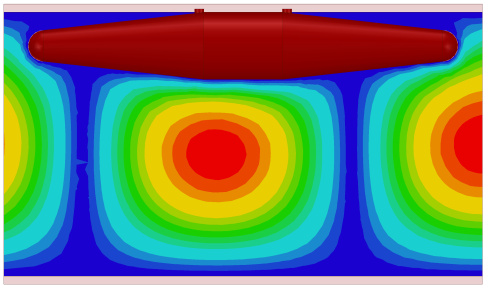

(a) E-field. Fin is moved 0.0 mm. Maximal E-field is 0.55 MV/m.

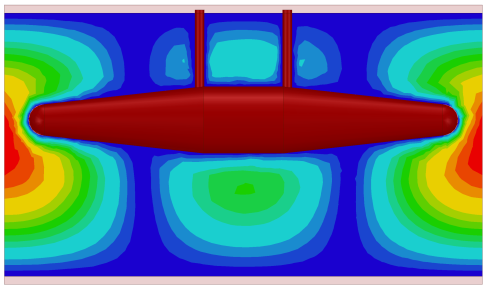

(b) E-field. Fin is moved 46.0 mm. Maximal E-field is 1.08 MV/m.

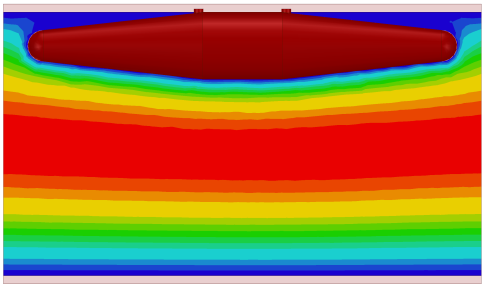

(c) Magnitude of E-field. Fin is moved 0.0 mm.

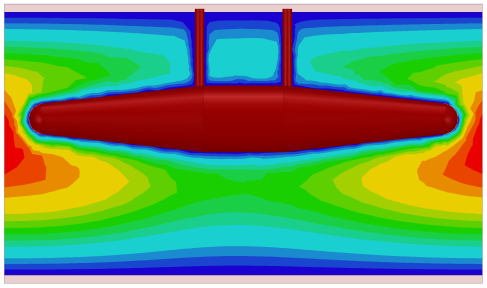

(d) Magnitude of E-field. Fin is moved 46.0 mm.

Figure 3.23: Simulated E-field in the variable phase shifter.

Table 3.5 shows the simulated S parameter of the variable phase shifter. The simulated result of this variable phase shifter can satisfy the requirements of the compact LPDS.

Table 3.5: Simulated S parameter of the variable phase shifter.

Length	300 mm
Moving range of fin	0.0 mm $\sim$ 46.0 mm
Phase shift range	$35.9^\circ \sim -1.9^\circ$
Phase shift length	37.8°
Maximal $\lvert S_{11} \rvert$	-30.00 dB
Maximal E-field	1.08 MV/m

As shown in Fig. 3.21, the magnitude of the reflection is increased to more than -30.00 dB when the transmitted phase is decreased to less than -1.9°. Usually, the reflection of the manufactured components is higher compared to the simulated results. Thus, the phase range of the variable phase shifter is 17.5° with a variation of $\pm 17.5^\circ$. Based on the phase range of the variable

phase shifter and the shifted phase of the variable hybrid, the phase margin of the variable phase shifter can be calculated in detail. This phase margin can compensate for the phase difference between the connected RF components of different cavities such as the circulator, bellow, and input coupler. It can also compensate for the phase difference between the simulated and the manufactured components for the compact LPDS. Thus, this phase margin corresponds to the required uniformity of the phase for the compact LPDS. Table 3.6 displays the phase margin of the variable phase shifter.

Table 3.6: Phase margin of the variable phase shifter.

	Simulated phase margin
#VPS1	$-11.86^\circ \sim 10.44^\circ$
#VPS2	$-11.06^\circ \sim 10.12^\circ$
#VPS3	$-10.21^\circ \sim 9.65^\circ$
#VPS4	$-9.27^\circ \sim 8.79^\circ$
#VPS5	$-17.5^\circ \sim 17.5^\circ$

3.4.4 Design of Fixed Phase shifter

For the average power distributed condition, the power transmitted to each cavity is adjusted by the variable hybrid to be equal. The variable phase shifter is set to the center of the phase shift range. In this case, the fixed phase shifter is designed to adjust the phase difference between adjacent cavities as 90°. Figure 3.24 shows the fixed phase shifter for downstream and upstream of the compact LPDS.

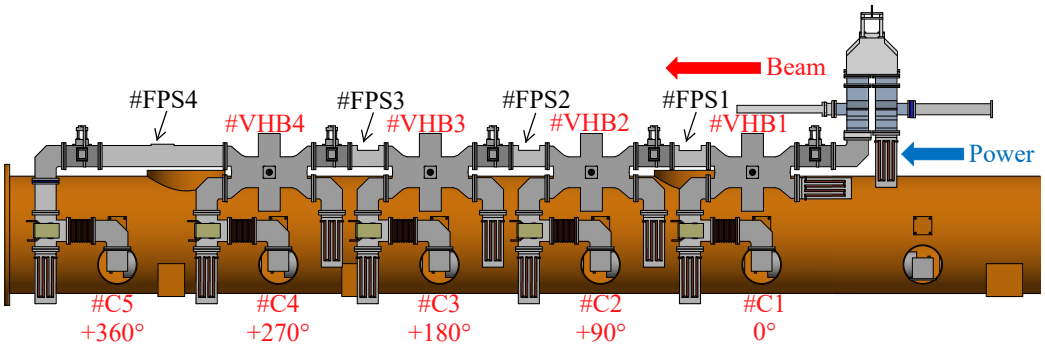

(a) Downstream of compact LPDS.

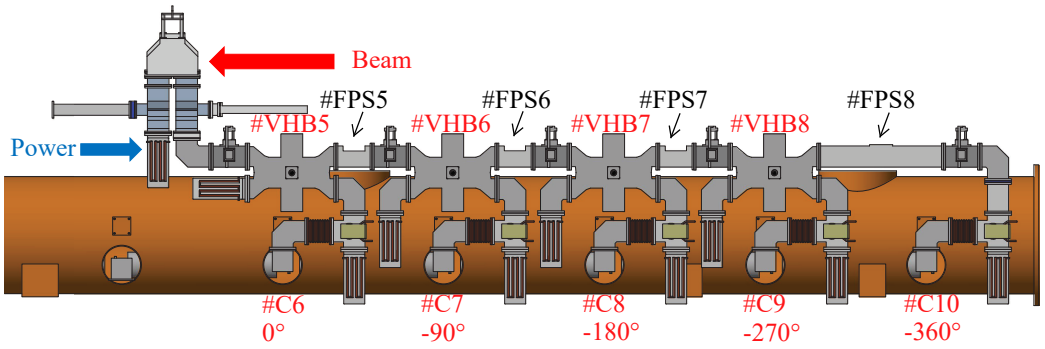

(b) Upstream of compact LPDS.

Figure 3.24: Fixed phase shifter for downstream and upstream of the compact LPDS.

The center of the phase range of variable phase shifter is 17.5°. Table 3.7 shows the simulated S parameters of eight variable hybrids (#VHB1 ∼ #VHB8) for the average power distributed condition. The required phase of the fixed phase shifter can be calculated based on the phase of the variable phase shifter and the variable hybrid. Tab 3.8 shows the required phase of eight fixed phase shifters. The lengths of the variable hybrid and the variable phase shifter are 730 mm and 300 mm respectively. Considering the geometric length between adjacent cavities of 1326 mm, the length of the fixed phase shifter should be 296 mm or 1026 mm.

Table 3.7: Simulated S parameters of eight variable hybrids (#VHB1 ∼ #VHB8) for the average power distributed condition.

	$\lvert S_{31}\rvert$	Position of fin	S_{21} phase	S_{31} phase
#VHB1&5	-6.99 dB (20.0%)	2.8 mm	162.84°	−107.17°
#VHB2&6	-6.02 dB (25.0%)	4.0 mm	159.04°	−110.99°
#VHB3&7	-4.77 dB (33.3%)	6.0 mm	153.33°	−116.74°
#VHB4&8	-3.01 dB (50.0%)	10.4 mm	142.40°	−127.62°

Table 3.8: Required phase of eight fixed phase shifters (#FPS1 ∼ #FPS8).

		Phase	Length
Downstream LPDS	#FPS1	−86.52°	296 mm
	#FPS2	−80.79°	296 mm
	#FPS3	−69.95°	296 mm
	#FPS4	98.68°	1026 mm
Upstream LPDS	#FPS5	93.48°	296 mm
	#FPS6	99.21°	296 mm
	#FPS7	110.05°	296 mm
	#FPS8	−81.32°	1026 mm

The guide wavelength λ_g of the TE_{10} mode in the waveguide is determined by the width of the waveguide. Thus, the phase of the waveguide can be changed according to the width of the waveguide. The simplest approach designing the fixed phase shifter is to change the width W of the waveguide. The phase of the 296 mm straight waveguide is 29.27° for the WR650 type. Figure 3.25 shows the two models of the fixed phase shifters. L and W are the length and width of the waveguide with variable width, respectively. The narrow fixed phase shifter has the narrow part of the waveguide. Within the narrow part, W is reduced, and λ_g is increased. Thus, the phase is increased. The phase of the narrow fixed phase shifter is greater than 29.27°. The wide fixed phase shifter includes wide part of the waveguide. Within the wide part, W is increased, and λ_g is reduced. Thus, the phase is reduced. The phase of the wide fixed phase shifter is smaller than 29.27°.

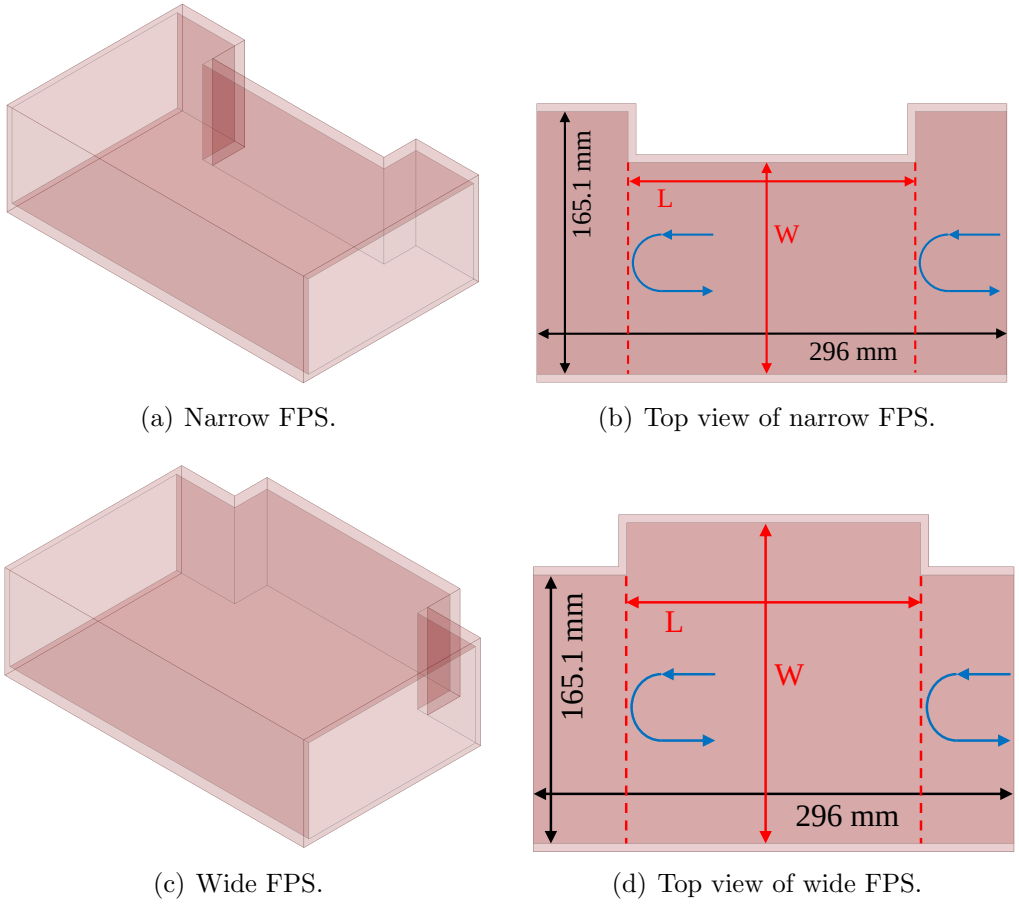

(a) Narrow FPS.

(b) Top view of narrow FPS.

(c) Wide FPS.

(d) Top view of wide FPS.

Figure 3.25: Two models of fixed phase shifters (FPS).

As shown in Fig. 3.25, there are two reflected waves existed in the fixed phase shifter. The phase difference between the two reflected waves is determined by L and W. The superposition of these two reflected waves can lead to cancellation by optimizing L and W. Thus, the reflection of the fixed phase shifter can be reduced. To ensure that only TE_{10} is generated in the fixed phase shifter, W should have a range from 115 mm to 230 mm. Considering the thickness of the wall of the waveguide and the space of the flanges, L should be less than 220 mm for a 296 mm fixed phase shifter. Figure 3.26 shows the relationship between L and ΔW, and the minimal reflection for the 296 mm fixed phase shifter. $\Delta W = W - 165.1\text{mm}$. ΔW can only be changed from -42 mm to 45 mm due to the limit of L. The minimal reflection is less than -58.0 dB for the optimized fixed phase shifter. The optimized L is very sensitive to ΔW when ΔW is decreased to -42 mm. Thus, W cannot be very low for the narrow fixed phase shifter. In addition, the margin of

L is decreases with an increase of $|\Delta W|$ such that $|S_{11}|$ is less than -30.0 dB. Figure 3.27 shows the simulated transmitted phase compared to ΔW for the optimized 296 mm fixed phase shifter. For the optimized fixed phase shifter, the phase can be shifted from -5.74° to 229.98°. Table 3.9 displays the simulated result for the optimized 296 mm fixed phase shifter.

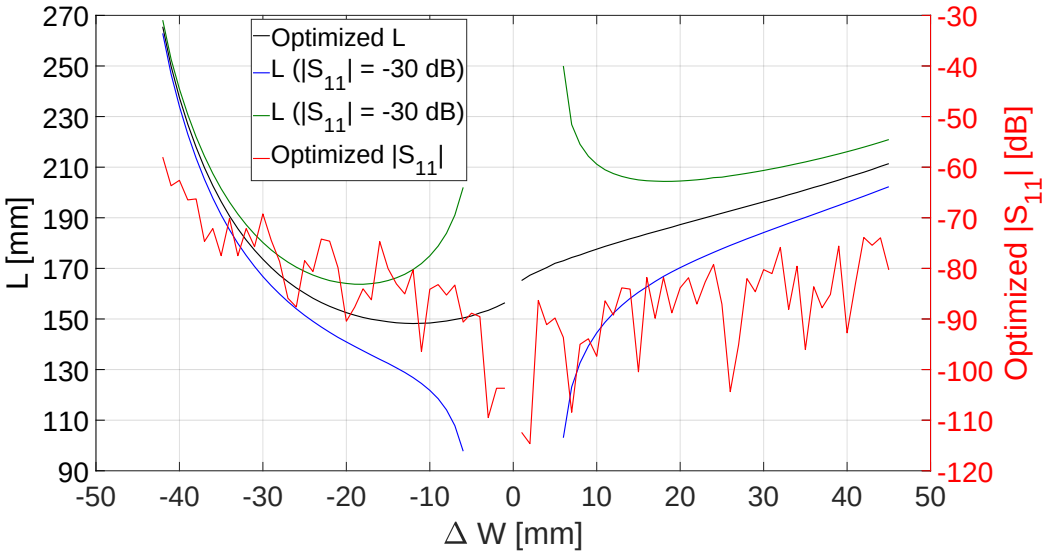

Figure 3.26: Relationship between L and ΔW, and the minimal reflection for the 296 mm fixed phase shifter. The variable range of ΔW is from -42 mm to 45 mm due to the limit of L.

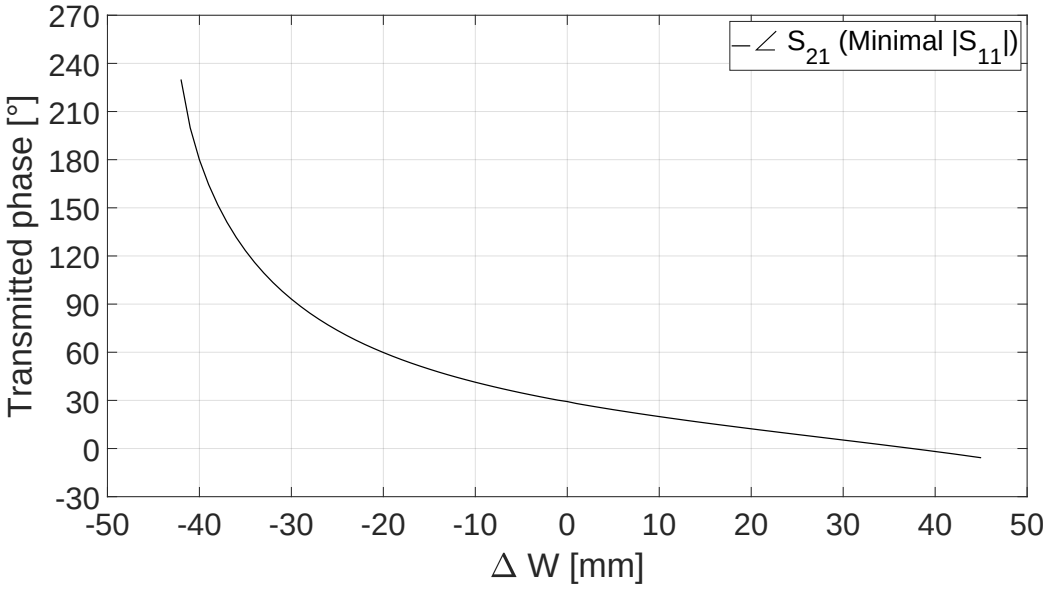

Figure 3.27: Simulated transmitted phase ($\angle S_{21}$) compared to ΔW for the optimized 296 mm fixed phase shifter. $\Delta W = W - 165.1$mm.

Table 3.9: Simulated result for the optimized 296 mm fixed phase shifter

ΔW	-42 $\sim$ 45 mm
S_{11}	$<$ -58.0 dB
$\angle S_{21}$	$229.98^\circ \sim -5.74^\circ$

For the required phase of the 296 mm fixed phase shifter shown in Table 3.8, #FPS5$\sim$7 for the upstream compact LPDS can be realized using the narrow fixed phase shifter. Figure 3.28 shows the simulated model for the upstream compact LPDS for five cavities. Three 296 mm fixed phase shifters and one wide fixed phase shifter of 1,026 mm are used for the compact LPDS for five cavities. Table 3.10 displays the designed parameters of the fixed phase shifter for the compact LPDS for five cavities.

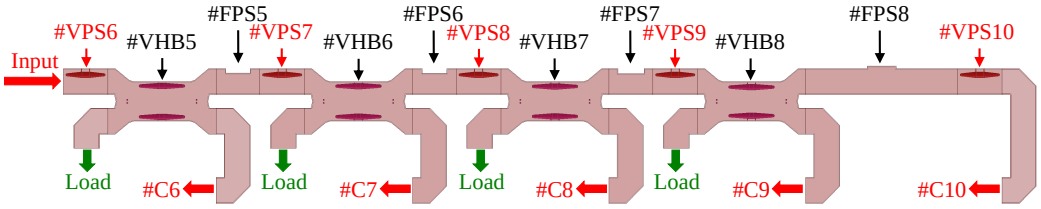

Figure 3.28: Simulated model for the upstream compact LPDS for five cavities.

Table 3.10: Designed parameters of the fixed phase shifter for the upstream compact LPDS for five cavities.

	Length	ΔW	L	Sim. Phase	Req. Phase
#FPS5	296 mm	-30.0 mm	173.6 mm	93.14°	93.48°
#FPS6	296 mm	-31.2 mm	178.0 mm	99.10°	99.21°
#FPS7	296 mm	-33.1 mm	186.2 mm	110.03°	110.05°
#FPS8	1026 mm	17.0 mm	184.4 mm	−81.66°	−81.32°

However, the #FPS1∼3 cannot be realized by the narrow or wide fixed phase shifter. One possible solution is to use a wide fixed phase shifter with an additional straight waveguide with a specific length. Figure 3.29 shows the simulated model for the downstream compact LPDS for five cavities. Three identical 296 mm wide fixed phase shifters are used to reduce the production cost. Table 3.11 displays the designed parameters of the fixed phase shifter for the downstream compact LPDS for five cavities. L and ΔW for the wide fixed phase shifter are 205.0 mm and 39.0 mm, respectively, and the transmitted phase is −1.09°. Table 3.12 displays the length of additional straight waveguide for the downstream compact LPDS for five cavities.

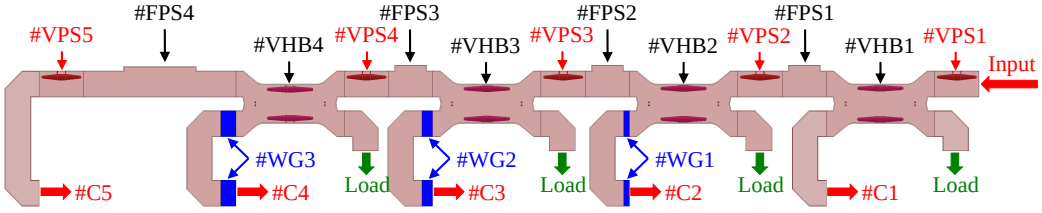

Figure 3.29: Simulated model for the downstream compact LPDS for five cavities.

Table 3.11: Designed parameters of the fixed phase shifter for the downstream compact LPDS for five cavities.

	Length	ΔW	L	Sim. Phase
#FPS1&2&3	296 mm	39.0 mm	205.0 mm	$-1.09°$
#FPS4	1026 mm	30.0 mm	480.6 mm	$-131.22°$

Table 3.12: Length of additional straight waveguide for the downstream compact LPDS for five cavities.

#WG1	38 mm
#WG2	73 mm
#WG3	103 mm

3.5 Simulation of compact LPDS

After the design of the variable hybrid, the variable phase shifter and the fixed phase shifter, the compact LPDS can be evaluated via simulation. Figure 3.30 shows the simulated E-field of the downstream compact LPDS for five cavities and the average power distributed condition. In this case, the simulated power transmitted to each cavity is in the range of -6.96 dB to -7.10 dB, and close to each other. The total power transmitted to the five cavities is 98.64% of the input power. In addition, the simulated phase of each cavity is deviated from the target value by less than 0.7°. The reflection to the input of the compact LPDS is -26.16 dB. The maximal E–field in this system is 0.62 MV/m, with an input power of 1.3 MW. Table 3.13 displays the simulated result of the downstream compact LPDS for five cavities under the average power distributed condition.

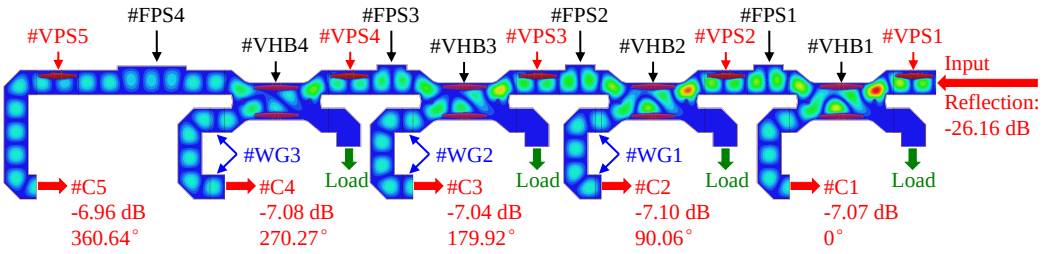

Figure 3.30: Simulation of downstream compact LPDS for the five cavities under the average power distributed condition.

Table 3.13: Simulated result of the downstream compact LPDS for five cavities under the average power distributed condition.

	#C5	#C4	#C3	#C2	#C1
target phase	360°	270°	180°	90°	0°
Sim. phase	360.64°	270.27°	179.92°	90.06°	0°
Sim. power	-6.96 dB	-7.08 dB	-7.04 dB	-7.10 dB	-7.07 dB
5 cavities' power	98.64%				
Reflection to input	-26.16 dB				
Maximal E–field	0.62 MV/m (1.3 MW)				

Figure 3.31 shows the simulated E-field of the upstream compact LPDS for five cavities under the average power distributed condition. In this case, the simulated power transmitted to each cavity is in the range of -6.99 dB to -7.12 dB and close to each other. The total power transmitted to the five cavities is 98.71% of the input power. In addition, the simulated phase of each cavity is deviated from the target value by less than 0.5°. The reflection to the input of the compact LPDS is -30.66 dB. The maximal E–field in this system is 0.63 MV/m, with an input power of 1.3 MW. Table 3.14 displays the simulated result of the upstream compact LPDS under the five cavities in average power distributed condition.

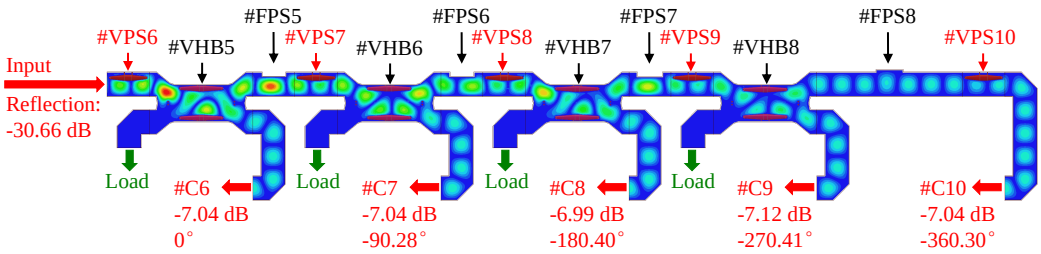

Figure 3.31: Simulation of the upstream compact LPDS for five cavities under the average power distributed condition.

Table 3.14: Simulated result of the upstream compact LPDS for five cavities under the average power distributed condition.

	#C6	#C7	#C8	#C9	#C10
target phase	0°	−90°	−180°	−270°	−360°
Sim. phase	0°	−90.28°	−180.40°	−270.41°	−360.30°
Sim. power	-7.04 dB	-7.04 dB	-6.99 dB	-7.12 dB	-7.04 dB
5 cavities' power	98.71%				
Reflection to input	-30.66 dB				
Maximal E–field	0.63 MV/m (1.3 MW)				

The simulated results indicate that both upstream and downstream of the compact LPDS can realize the average power distributed condition and adjust the phase difference between adjacent cavities for 90°. The maximal E–field in the compact LPDS is 0.63 MV/m, with an input power of 1.3 MW, which is less than 25% of 3 MV/m (breakdown field in air) [27].

Chapter 4

Probabilistic Analysis of Compact LPDS

In the previous chapter, ±25% variation of the input power of the cavity is proposed to satisfy the ±20% variation of the accelerating gradient of the cavity, based on the situation of optimal tuning. In this chapter, the probabilistic analysis of the compact LPDS will be introduced for equal Q_L and $P_k Q_L$ control [20]. In the case of the 250 GeV ILC, the quantity of the SC cavity is approximately 8,000. Thus, the simulated random events of 10^7 are determined to evaluate the feasibility of the compact LPDS.

4.1 Probabilistic Analysis for equal Q_L

In this section, the probabilistic analysis of the compact LPDS is based on the equal Q_L. As previously mentioned, the accelerating gradient of the SC cavity for the ILC is 31.5 MV/m, with a variation of ±20%, depending on the cavity's performance. The uniform distribution of the accelerating gradient from 25.2 MV/m to 37.8 MV/m is taken into account. Figure 4.1 shows the uniform distribution of the accelerating gradient of the SC cavity for the ILC. In the case of an accelerating gradient of 31.5 MV/m and a beam current of 5.8 mA, the optimal loaded Q_L is calculated to be 5.44×10^6 from equation (B.17). This Q_L of 5.44×10^6 is used for the analysis in this section.

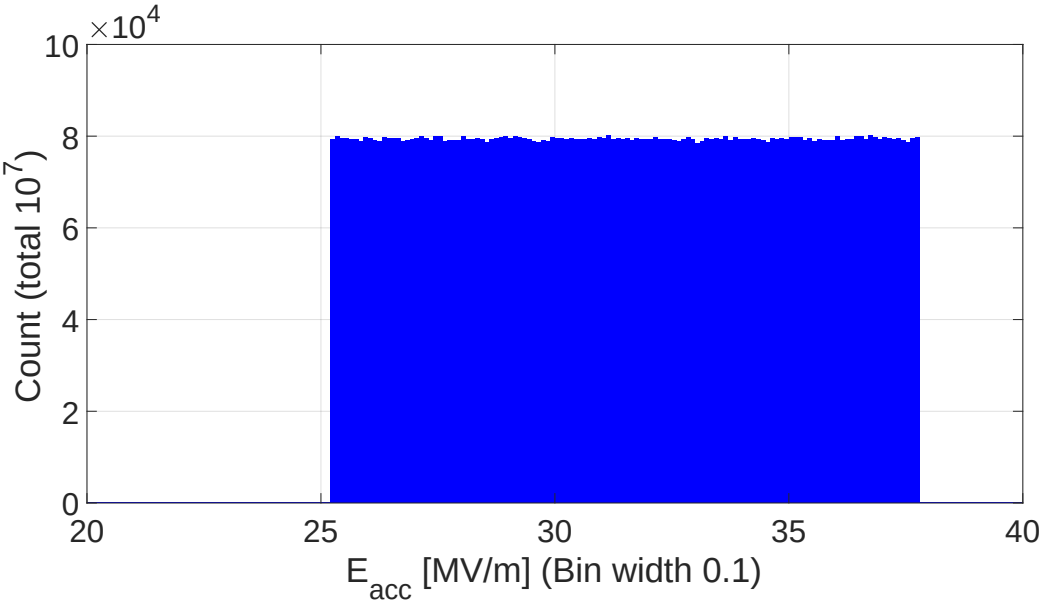

Figure 4.1: Uniform distribution of the accelerating gradient of the SC cavity for the ILC. The E_{acc} is distributed from 25.2 MV/m to 37.8 MV/m.

When the beam is accelerated on the crest of the RF field, the generator power of the SC cavity is [17]

$$P_g = \frac{V_{cav}^2}{4Q_L\left(\frac{r}{Q}\right)}\left(\left[1+\frac{\left(\frac{r}{Q}\right)Q_L I_{b0}}{V_{cav}}\right]^2+\left[\frac{\Delta f}{f}\right]^2\right) \tag{4.1}$$

The bandwidth $f_{1/2}$ of the SC cavity is calculated of 120 Hz.

$$f_{1/2} = \frac{f}{2Q_L} \tag{4.2}$$

During long time beam operation, the detuning of the SC cavity randomly deviates from 0 Hz [19]. The required generator power is increased to maintain the maximal accelerating gradient if detuning occurs. Thus, detuning should be controlled within a maximal detuning range Δf_{max} based on the feedback of the Low Level RF Control System (LLRF). The uniform distribution of detuning from $-\Delta f_{max}$ to Δf_{max} is considered. Referring to the ILC-TDR, the total input power P_{sum} of 39 cavities is less than 8.25 MW due to the power loss of the PDS and the overhead of the LLRF control. Table 4.1 displays the covered probability of the 10 MW MBK for the case of detuning. Considering that the number of RF stations is approximately 236,

the Δf_{max} should be less than 45 Hz to ensure that the 10 MW MBK can supply enough power for all the SC cavities. Figure 4.2 shows the distribution of the generator power for one cavity (P_g) and 39 cavities (P_{sum}) with a maximal detuning of $\pm$45 Hz. In the case of detuning within $\pm$45 Hz, P_g is distributed from 153.6 kW to 239.4 kW and P_{sum} is distributed from 6.800 MW to 8.303 MW.

Table 4.1: Covered probability of the 10 MW MBK for the case of detuning. Detuning is uniformly distributed from $-\Delta f_{max}$ to Δf_{max}. P_{sum} is the total input power of the 39 cavities, which should be less than 8.25 MW. $Q_L = 5.44 \times 10^6$.

Δf_{max}	$P_{sum} \leq 8.25$ MW
0 Hz	100.00%
25 Hz	100.00%
40 Hz	99.81%
45 Hz	99.70%
50 Hz	99.50%
55 Hz	99.16%
60 Hz	98.59%
65 Hz	97.62%
70 Hz	96.08%
75 Hz	93.64%
100 Hz	59.93%

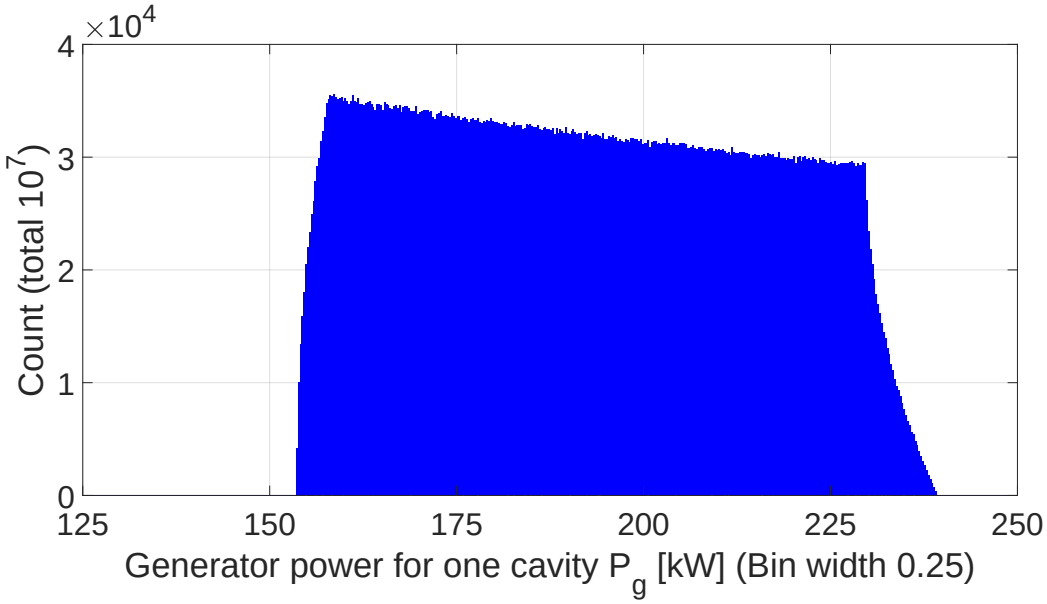

(a) Generator power for one cavity (P_g). P_g is distributed from 153.6 kW to 239.4 kW.

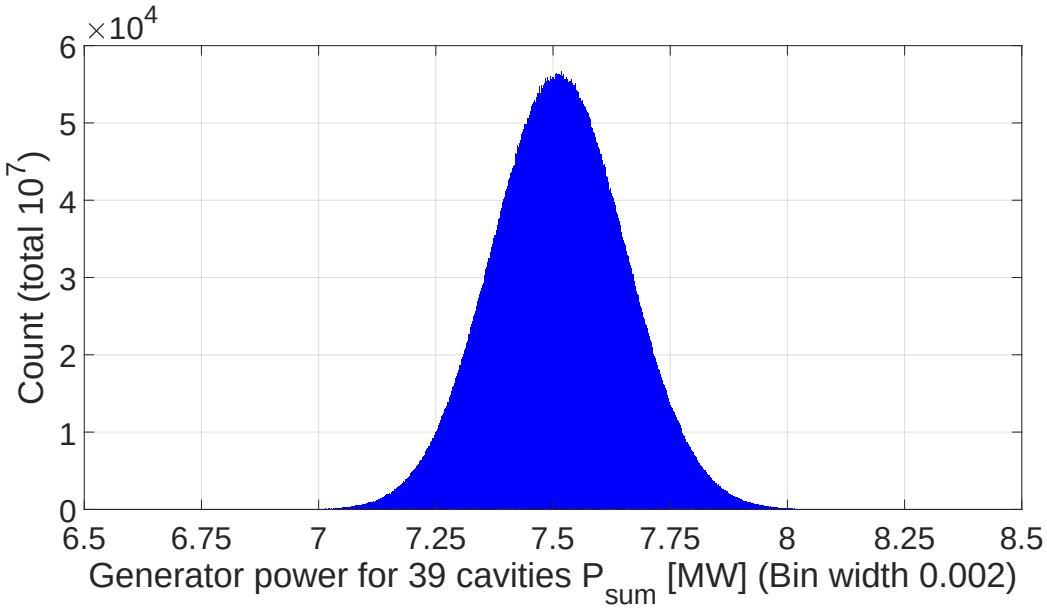

(b) Generator power for 39 cavity (P_{sum}). P_{sum} is distributed from 6.800 MW to 8.303 MW.

Figure 4.2: Distribution of the generator power for one cavity and 39 cavities with a maximal detuning of ±45 Hz.

Table 4.2 displays the covered probability of the four variable hybrids of the compact LPDS for the case of detuning. If detuning is controlled within

±125 Hz, the four variable hybrids can adjust the input power of all the cavities to the required level.

Table 4.2: Covered probability of the four variable hybrids of the compact LPDS for the case of detuning. Detuning is uniformly distributed from $-\Delta f_{max}$ to Δf_{max}. $Q_L = 5.44 \times 10^6$.

Δf_{max}	Covered probability			
	$\|S_{31}\|$-#VHB1 -8.85 -5.31 dB	$\|S_{31}$-#VHB2 -7.78 -4.47 dB	$\|S_{31}$-#VHB3 -6.37 -3.42dB	$\|S_{31}\|$-#VHB4 -4.26 -2.04dB
0 Hz	100.00%	100.00%	100.00%	100.00%
25 Hz	100.00%	100.00%	100.00%	100.00%
50 Hz	100.00%	100.00%	100.00%	100.00%
75 Hz	100.00%	100.00%	100.00%	100.00%
100 Hz	100.00%	100.00%	100.00%	99.90%
125 Hz	99.99%	99.96%	99.96%	99.87%
150 Hz	99.82%	99.68%	99.28%	97.57%

In the case of the same $Q_L(5.44 \times 10^6)$ for the 39 cavities, taking into account the total power for the 39 cavities and the available power dividing ratio of the variable hybrids, the detuning of the SC cavities should be controlled within ±45 Hz using the feedback of the LLRF system to satisfy the required power for each cavity. Figure 4.3 shows the distribution of the coupling ratio of the four variable hybrids in the case of detuning within ±45 Hz. Furthermore, considering the phase shift of the cavity caused by detuning and a phase margin of 15° for the variable phase shifter, the tolerance of detuning should be controlled within ±16 Hz (the bandwidth of the SC cavity is 120 Hz) for the same Q_L operation.

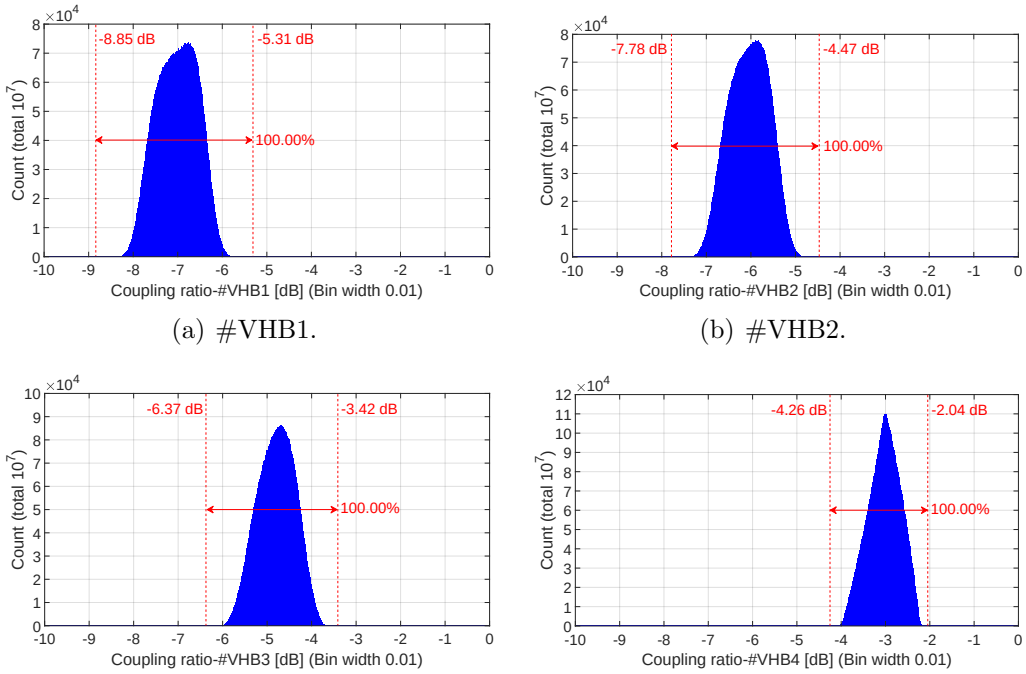

(a) #VHB1. (b) #VHB2.

(c) #VHB3. (d) #VHB4.

Figure 4.3: Distribution of the coupling ratio of four variable hybrids in the case of detuning within ±45 Hz.

4.2 Probabilistic Analysis for P_kQ_L control

In this section, the probabilistic analysis of the compact LPDS is based on P_kQ_L control [20]. In the case of P_kQ_L control, the loaded quality factor Q_L of each cavity is adjusted based on its maximal accelerating gradient to maintain the flattop of the accelerating field. The simplest assumption that operate on resonance (0 Hz detuning) is took in account in the discussion of this section. Figure 4.4 shows the relationship between the loaded quality Q_L, generator power P_g, and the accelerating gradient E_{acc} for P_kQ_L control (injection time T_{inj} is 924 μs and beam current I_{b0} is 5.8 mA). The Q_L for P_kQ_L control can be determined from the following equation [20]

$$V_{cav(flat)} = E_{acc} \cdot l = I_{b0} \left(\frac{r}{Q}\right) Q_L \left(e^{\frac{T_{inj}\omega_0}{2Q_L}} - 1\right) \tag{4.3}$$

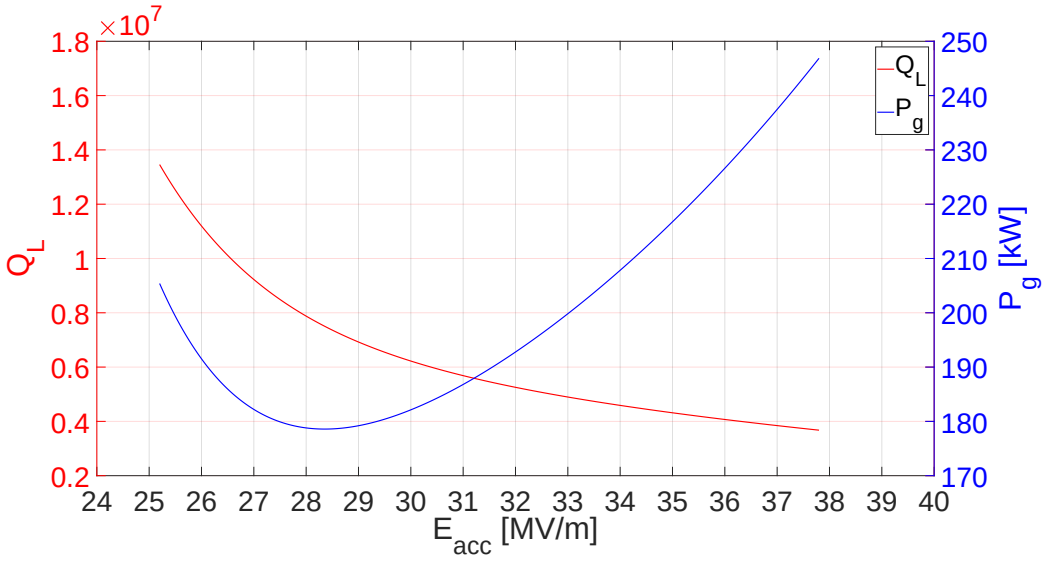

Figure 4.4: Relationship between loaded quality Q_L, generator power P_g and accelerating gradient E_{acc} for P_kQ_L control. $T_{inj} = 924$ µs. $I_{b0} = 5.8$ mA.

For P_kQ_L control, a lower loaded quality Q_L is required for a cavity with a higher accelerating gradient, which leads to a narrower bandwidth. The wider tolerance of detuning is due to the narrower bandwidth for the cavity with a higher accelerating gradient. Considering the highest accelerating field of 37.8 MV/m, the loaded quality Q_L and bandwidth $f_{1/2}$ are 3.68×10^6 and 177 Hz, respectively. The maximal tolerance of detuning is ±23 Hz for a cavity of with an accelerating field of 37.8 MV/m.

The E_{acc} is also considered as a uniform distribution with a center of 31.5 MV/m and a fluctuation of ±20%. Figure 4.5 shows the distribution of Q_L for P_kQ_L control. The simulated Q_L is distributed from 3.68×10^6 to 1.35×10^7.

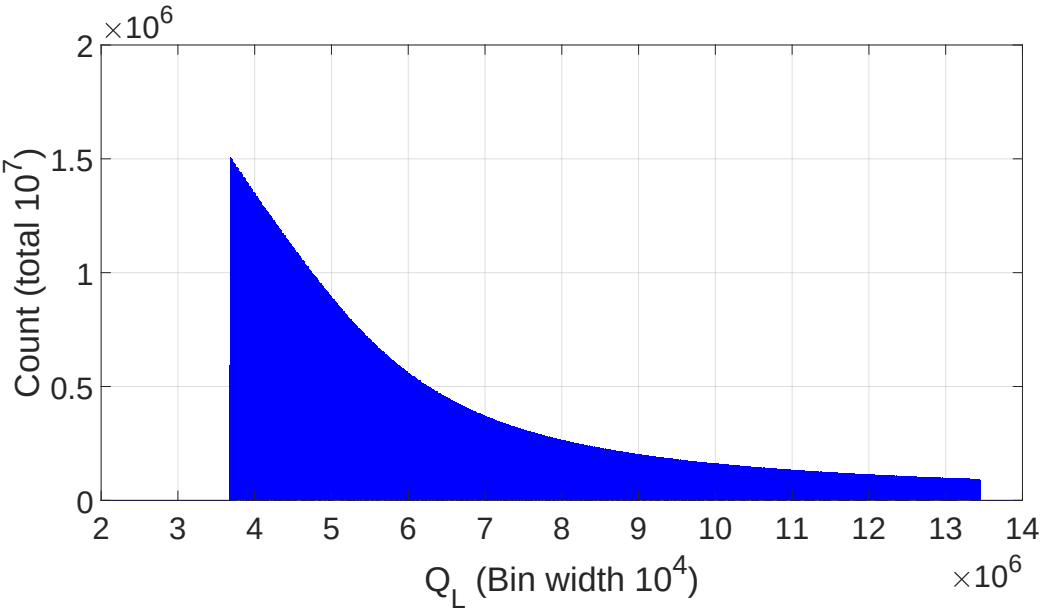

Figure 4.5: Distribution of Q_L for P_kQ_L control. E_{acc} has uniform distribution with center of 31.5 MV/m and a fluctuation of $\pm 20\%$. Q_L is distributed from 3.68×10^6 to 1.35×10^7.

Figure 4.6 shows the distribution of the generator power for one cavity (P_g) and 39 cavities (P_{sum}) for P_kQ_L control. In the case of P_kQ_L control, the P_g is distributed from 178.6 kW to 247.1 kW and the P_{sum} is distributed from 7.250 MW to 8.506 MW. The generator power for one cavity at 178.6 kW has the maximal probability. As previously indicated, the maximal input power of the 39 cavities is 8.25 MW. The probability that P_{sum} is less than 8.25 MW is 99.96%. Thus, it can be concluded that the 10 MW MBK can supply sufficient power for 39 cavities for P_kQ_L control.

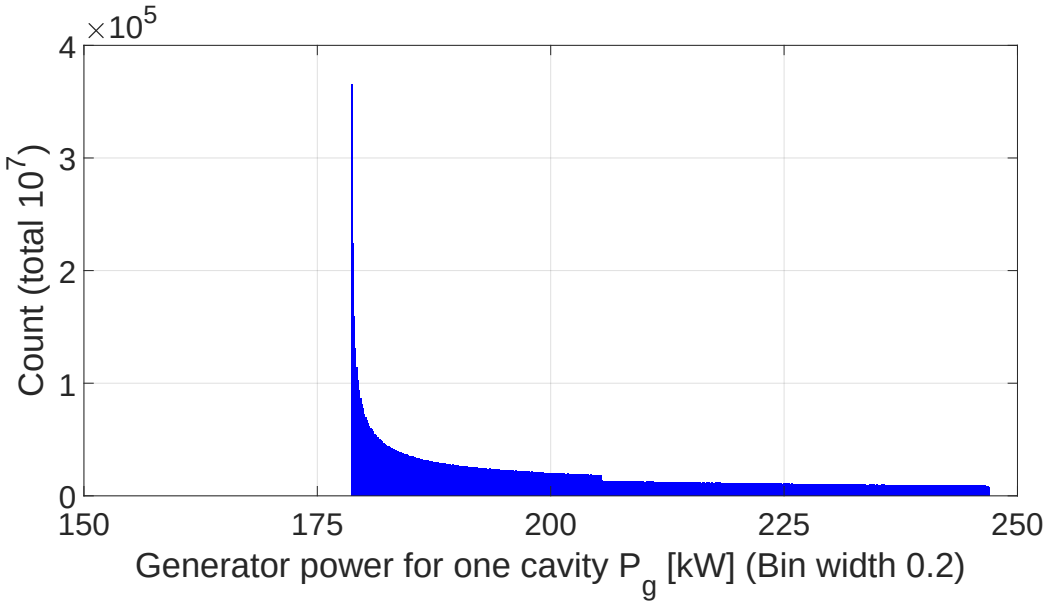

(a) Generator power for one cavity (P_g). P_g is distributed from 178.6 to 247.1 kW.

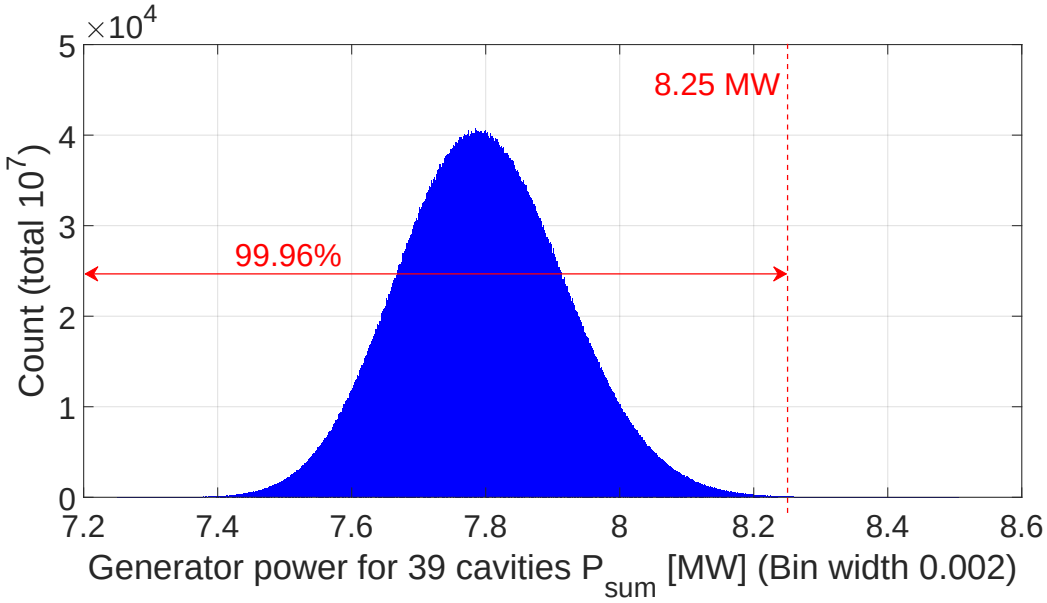

(b) Generator power for 39 cavity (P_{sum}). P_{sum} is distributed from 7.250 to 8.506 MW

Figure 4.6: Distribution of generator power for one cavity and 39 cavities for P_kQ_L control.

Figure 4.7 shows the distribution of the coupling ratio of four variable hybrids for P_kQ_L control. In the case of P_kQ_L control, the four variable hybrids can adjust the input power of the cavity to the required level with

a probability of 100%. Table 4.3 displays the distributed range and the probability associated with compact LPDS for P_kQ_L control.

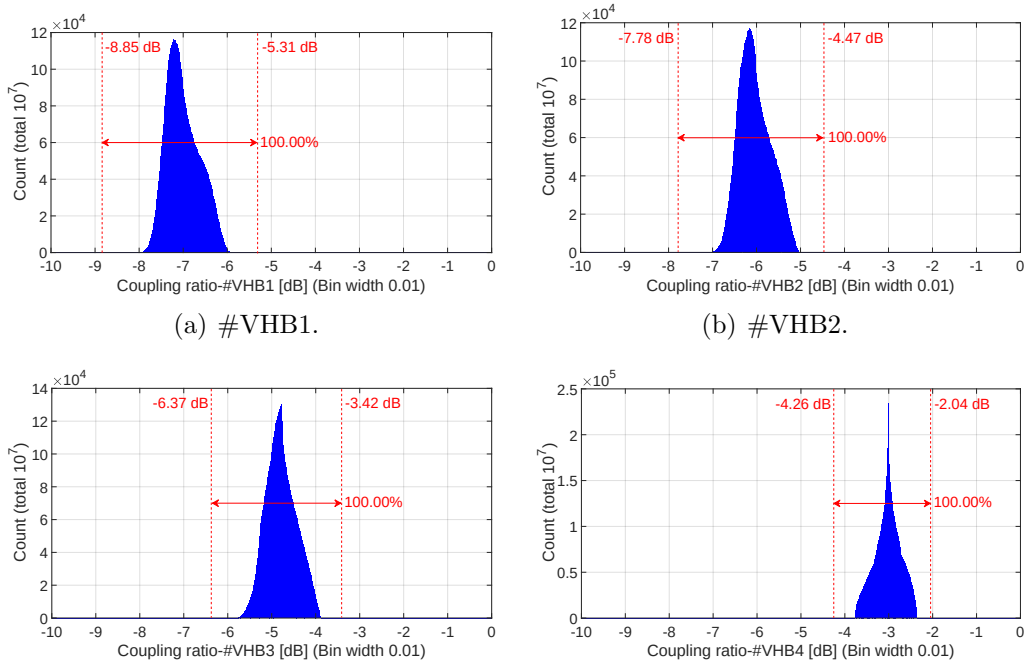

(a) #VHB1. (b) #VHB2.

(c) #VHB3. (d) #VHB4.

Figure 4.7: Distribution of coupling ratio of four variable hybrids for P_kQ_L control.

Table 4.3: Distributed range and probability associated with compact LPDS for P_kQ_L control.

Distributed range		
	Min	Max
E_{acc}	25.2 MV/m	37.8 MV/m
Q_L	3.68×10^6	1.35×10^7
P_g for one cavity	178.6 kW	247.1 kW
P_g for 39 cavities	7.25 MW	8.51 MW
Distributed Probability		
P_g for 39 cavities ($\leq$ 8.25 MW)	99.96%	
#VHB1 (-8.85 $\sim$ -5.31 dB)	100.00%	
#VHB2 (-7.78 $\sim$ -4.47 dB)	100.00%	
#VHB3 (-6.37 $\sim$ -3.42 dB)	100.00%	
#VHB4 (-4.26 $\sim$ -2.04 dB)	100.00%	

In this chapter, the simulated probability of compact LPDS is introduced based on the assumption of ±25% adjusted variation of the input power of the cavity. For the same Q_L operation, the detuning should be controlled within ±16 Hz to ensure that the 10 MW MBK supplies sufficient power for 39 cavities. All the cavities are operated at the maximal accelerating gradient and with a variable phase shifter to compensate for the phase shift due to detuning. For $P_k Q_L$ control with detuning of 0 Hz, the same simulated result is achieved and a wider tolerance of detuning is adopted for a cavity with a higher accelerating gradient. In the case of the highest accelerating field of 37.8 MV/m, the loaded quality Q_L and maximal tolerance of detuning are 3.68×10^6 and ±23 Hz, respectively. It is concluded that the ±25% adjusted variation of the input power of the cavity is an appropriate value for the operation of the SC cavity with a maximal accelerating gradient for the limited detuning of the SC cavity. The introduction, design, and simulation of the compact LPDS have been presented. The test of the RF components and compact LPDS will be introduced in the following chapters.

Chapter 5

Design and Operation of L-band Resonant Ring

In this chapter, the construction of L-band resonant ring in the STF is discussed including the theory, low power test, and high power operation of the resonant ring. The test plan of the RF components using resonant ring is also developed.

5.1 Motivation behind L-band Resonant Ring

The maximal input power of the RF components of the compact LPDS is approximately 1.3 MW with a pulse width of 1.65 ms and a repetition rate of 5 Hz. Considering the worst condition of total reflection, the E-field may be double and the power may be quadrupled, with a value of 5.2 MW. Thus, the power handling capability of the RF components should be 5.2 MW. A 5.2 MW circulator is difficult to manufacture due to the arcing problem. Although the 10 MW multi-beam klystron is installed in the STF, it cannot be used as the power source to directly test the RF components without the use of the circulator to protect the klystron from possible reflected power.

A resonant ring is commonly used in high power test of RF components due to its power amplification property [22]. An 800 kW modulated-anode klystron (CETD Co., Ltd. E37501) was developed in the STF, and is employed in the distributed RF system for the ILC. A 500 kW circulator was also manufactured. If the power gain of the resonant ring is more than a factor of 10, 5.2 MW circular power can be generated in the resonant ring using the 800 kW klystron as a power source and the 500 kW circulator to protect the 800 kW klystron from possible reflection.

5.2 Theory of Resonant Ring

The resonant ring is a closed loop of a waveguide system that can amplify power [22]. Figure 5.1 shows the basic structure of such a ring. It consists of a power source, hybrid, dummy load, and is a specific length of the waveguide system.

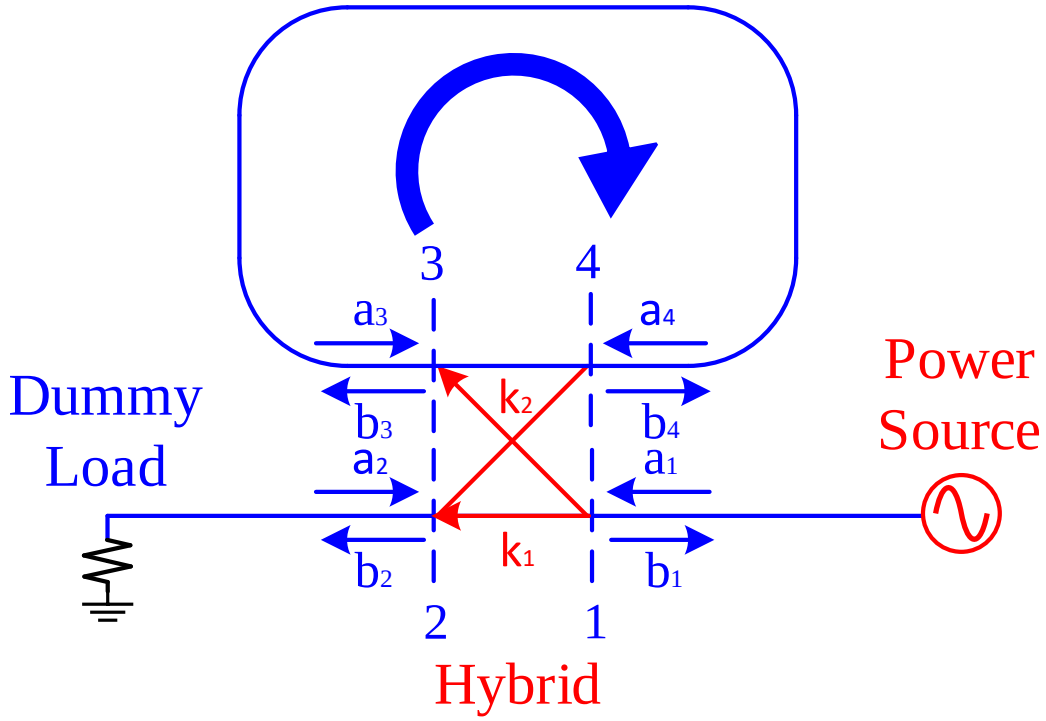

Figure 5.1: Basic structure of resonant ring.

The amplitude of the signal input to the hybrid is $a_1 \sim a_4$ and the amplitude of the signal output from the hybrid is $b_1 \sim b_4$. The relationship between the input and output signals of the hybrid is

$$[b] = [S][a] \tag{5.1}$$

The scattering matrix of the hybrid is $[S]$. If the hybrid is assumed to be lossless and symmetrical, $[S]$ is

$$[S] = \begin{bmatrix} 0 & k_1 & jk_2 & 0 \\ k_1 & 0 & 0 & jk_2 \\ jk_2 & 0 & 0 & k_1 \\ 0 & jk_2 & k1 & 0 \end{bmatrix} \tag{5.2}$$

The transmitted and coupling coefficients of hybrid at voltage are k_1 and k_2, respectively. For energy conversation, k_1 and k_2 have the relationship

$$k_1{}^2 + k_2{}^2 = 1 \tag{5.3}$$

For the simple assumption that no reflection occurs in the resonant ring, this implies that $b_1 = a_2 = a_3 = b_4 = 0$. Considering the scattering matrix, b_3 can be calculated as

$$b_3 = jk_2a_1 + k_1a_4 \tag{5.4}$$

Considering the circular region of the resonant ring from plane 3 to plane 4, the attenuation coefficient is α, the propagation constant is β and the geometric length of the circular region is L. The transmitted coefficient A can be expressed as

$$A = e^{-\alpha L}e^{-j\beta L} \tag{5.5}$$

The a_4 can be calculated from b_3 using the transmitted coefficient A

$$a_4 = A \times b_3 = b_3e^{-\alpha L}e^{-j\beta L} \tag{5.6}$$

Using the result for the scattering matrix and the transmitted coefficient, the b_3 is

$$b_3 = jk_2a_1 + k_1b_3e^{-\alpha L}e^{-j\beta L} \Rightarrow (1 - k_1e^{-\alpha L}e^{-j\beta L})b_3 = jk_2a_1 \tag{5.7}$$

The power gain G is

$$G = \frac{|b_3|^2}{|a_1|^2} = \frac{k_2{}^2}{1 + k_1^2e^{-2\alpha L} - 2k_1e^{-\alpha L}\cos(\beta L)} \tag{5.8}$$

The power gain can reach a maximal value when the one turn phase has the relationship $\beta L = 2N\pi$, where N is an integer. This means that a superposition of multiple signals in the circular region is at the optimum condition. Thus the maximal power gain $G_{\max}$ is given by [23]

$$G_{\max} = \frac{k_2{}^2}{1 + k_1^2e^{-2\alpha L} - 2k_1e^{-\alpha L}} = \frac{1 - k_1^2}{(1 - k_1e^{-\alpha L})^2} \tag{5.9}$$

If the transmitted coefficient k_1 is a variable that corresponds to the variable hybrid, the eventual maximal power gain $G'_{\max}$ can be achieved when k_1 is adjusted to be consistent with one turn attenuation of the amplitude of the wave $e^{-\alpha L}$, or the square root of the one turn power loss P_l

$$
\begin{aligned}
k_1 &= e^{-\alpha L} = \sqrt{P_l} \\
\Rightarrow G'_{\max} &= \frac{1-k_1^2}{(1-k_1 e^{-\alpha L})^2} = \frac{1}{1-e^{-2\alpha L}} = \frac{1}{1-P_l}
\end{aligned}
\tag{5.10}
$$

Based on accumulation, the same result can be deduced. $w^{(n)}$ is the wave at the n^{th} turn in the circular region and I is the input wave from the power source. The simulation of the forward power in the resonant ring is based on the calculation of accumulation.

$$
\begin{aligned}
w^{(n)} &= k_1 A w^{(n-1)} + j k_2 I \\
&= j k_2 I[1 + (k_1 A) + \cdots + (k_1 A)^{(n-1)}] \\
&= j k_2 I \frac{1-(k_1 A)^n}{1-(k_1 A)} \\
&\xrightarrow{n \Rightarrow \infty} \frac{j k_2 I}{1-(k_1 A)} \\
G &= \frac{|w^{(n)}|^2}{|I|^2} = \frac{k_2^2}{|1-k_1 A|^2} \\
&= \frac{{k_2}^2}{1+k_1^2 e^{-2\alpha L} - 2k_1 e^{-\alpha L}\cos(\beta L)}
\end{aligned}
\tag{5.11}
$$

5.3 Low Power Test of Resonant Ring

To predict the power gain of the resonant ring, a model was constructed in the STF to perform low power tests. Figure 5.2 shows the construction process and an image of the L-band resonant ring used for low power test. The 500 W solid state amplifier is used as the power source. Figure 5.3 shows the RF components of the L-band resonant ring for low power tests. There are two coupling output ports on the circulator to facilitate forward and backward monitoring in the waveguide. Thus, a directional coupler is not required in the circular region. The 850 mm variable hybrid is used to change the coupling ratio from the power source to the resonant ring. The transmitted coefficient at a power of k_1^2 can be adjusted from -0.06 dB to -6.29 dB, and the coupling coefficient at a power of k_2^2 can be adjusted from -23.68 dB to -1.23 dB. The 500 mm phase shifter is installed to adjust the one turn phase of the resonant ring to optimize the condition. The maximal adjustment phase range of the phase shifter is 73.71° and the power loss is -0.03 dB.

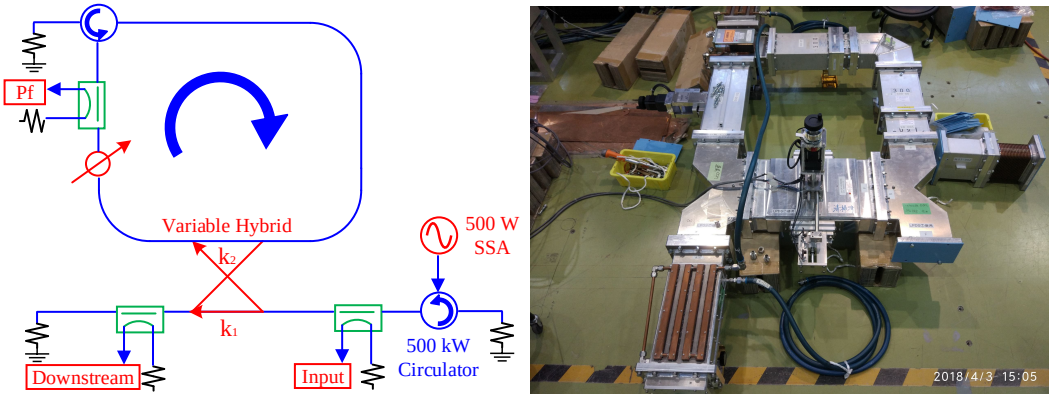

(a) Construction. (b) Image.

Figure 5.2: Construction process and image of L-band resonant ring used for low power test.

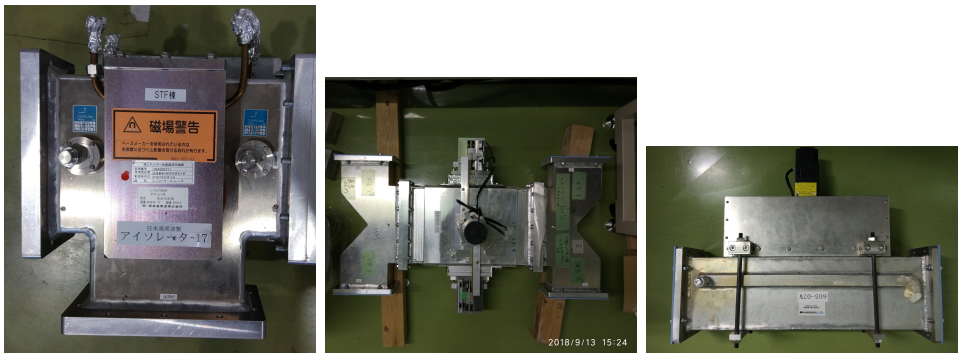

(a) Circulator. (b) 850 mm variable hybrid. (c) 500 mm phase shifter.

Figure 5.3: RF components of L-band resonant ring for low power tests.

The power loss of the circular region was determined to be -0.21 dB using network analyzer. A simulation was then performed based on the measured power loss. Figure 5.4 shows the measured and simulated power gain compared to the transmitted coefficient k_1^2. On the simulated curve, the power gain has a maximal value of 13.3 dB when k_1^2 is equal to the power loss of -0.21 dB. On the measured curve, the maximal power gain is 14.1 dB when k_1^2 is -0.25 dB. The calculated power loss is -0.17 dB with a power gain of 14.1 dB and k_1^2 of -0.25 dB. The calculated power loss is close to the measured value. The difference in power gain between the measurement and simulation may be due to the measured error of the power loss of the circular region. The power gain decreases rapidly when k_1^2 is larger than the power

loss P_l. Based on the simulation and measurement, the power gain of the L-band resonant ring can be more than 13 dB. A circular power of 5.2 MW can be achieved using an input power of 260 kW, which is available to the 800 kW klystron installed in the STF.

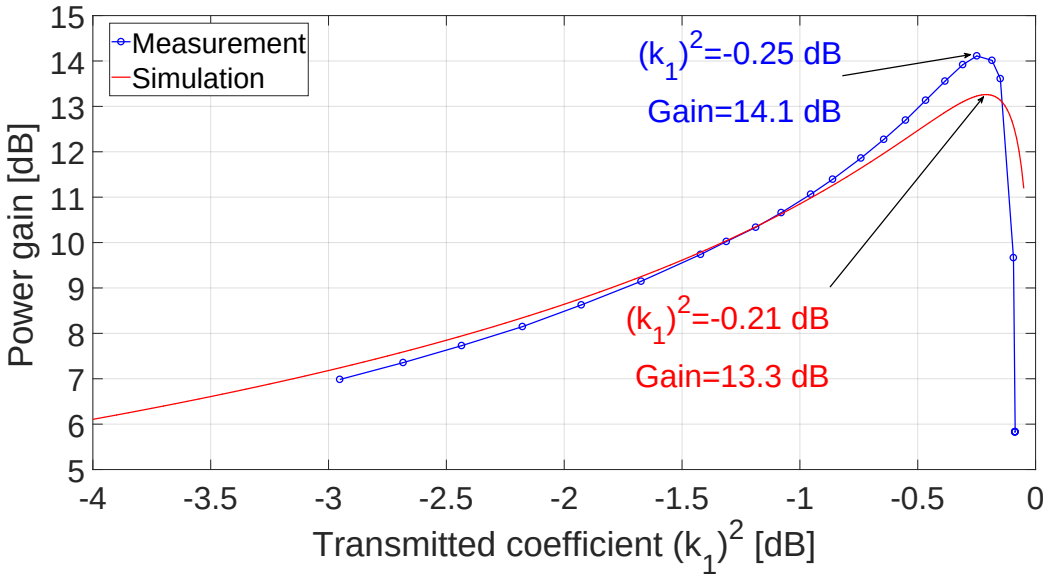

Figure 5.4: Measured and simulated power gain compared to the transmitted coefficient k_1^2. Maximal simulated power gain is 13.3 dB when k_1^2 is -0.21 dB. Maximal measured power gain is 14.1 dB when k_1^2 is -0.25 dB.

Figure 5.5 shows the measured and simulated power gain compared to the phase difference relative to the optimal condition. A phase difference of 0° corresponds to the maximal power gain. The 3 dB bandwidth is 5.4° for the simulation and 4.0° for the measurement. The phase shifter is effective and necessary to adjust the resonant ring.

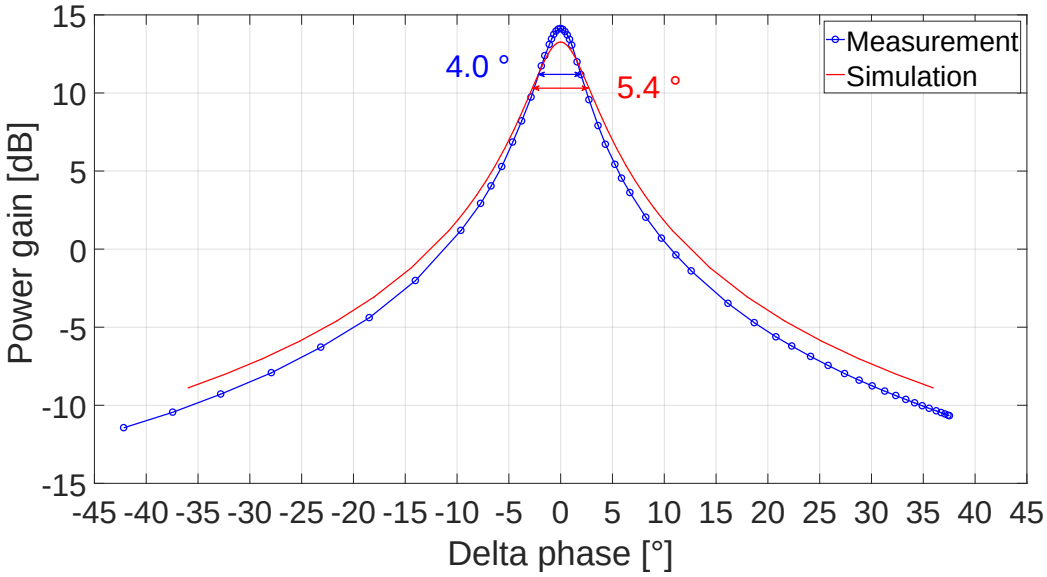

Figure 5.5: Measured and simulated power gain compared to the phase difference relative to the optimal condition. The simulated 3 dB width is 5.4°. The measured 3 dB width is 4.0°.

Figure 5.6 and Figure 5.7 show the measured and simulated downstream power divided by the input power. The downstream power is the power delivered to the dummy load. The measurement is consistent with the simulated result. The downstream power is very low when the resonant ring is operated near the optimal condition, which means that almost all the input power is stored and dissipated in the circular region of the resonant ring.

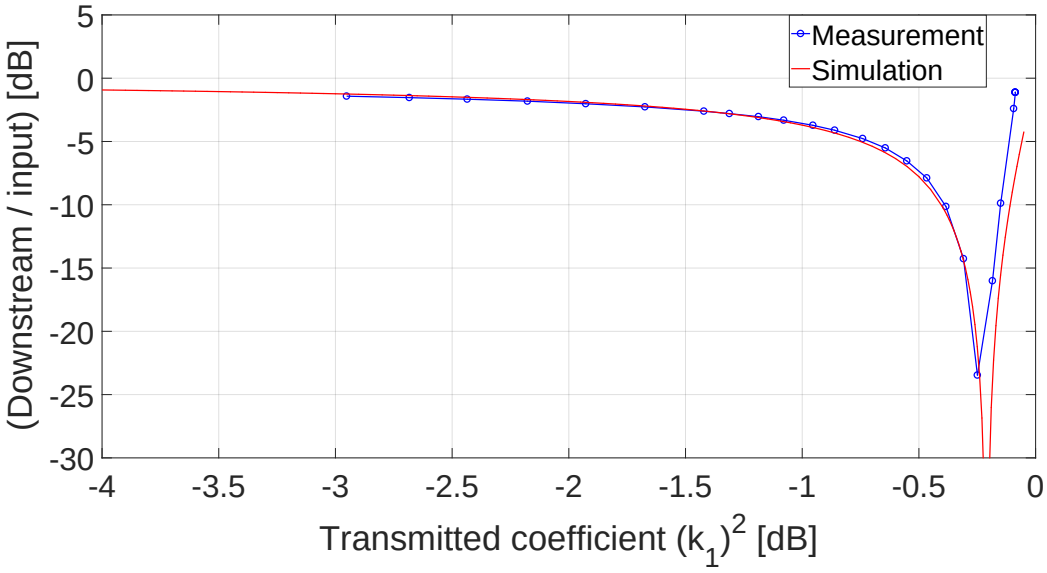

Figure 5.6: Measured and simulated power gain compared with the transmitted coefficient ${k_1}^2$.

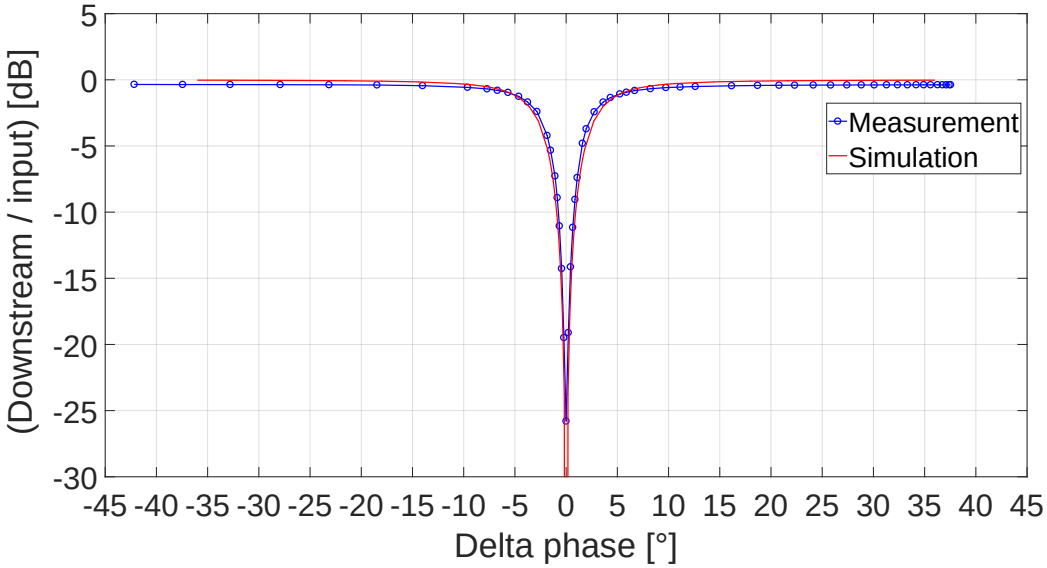

Figure 5.7: Measured and simulated downstream power divided by input power compared with the phase difference from optimal condition.

Based on the previous test with low power, the behavior of the L-band

resonant ring is consistent with the simulated result and power gain is demonstrated. In the plan involving high power operation at 5.2 MW, the resonant ring is expected to be pressurized with SF_6 of one atmosphere to prevent arcing [24]. The variable hybrid and variable phase shifter are not the pressurized type. The 11 dB hybrid is already manufactured, and the pressurized variable phase shifter is under production. The resonant ring is re-built for the 11 dB hybrid and without a variable phase shifter for low power test. The geometric length of the resonant ring is adjusted to be close to that at the optimal condition at a frequency of 1.3 GHz. It is possible to shift the operating frequency at approximately 1.3 GHz to precisely adjust the resonant ring at the optimal condition. Figure 5.8 shows the construction details and an image of resonant ring with the pressurized components. Five signals are measured. The 'Pf' and 'Pb' are the forward and backward power in the resonant ring. The 'Input' and 'Input-r' are the input power of the resonant ring and the reflected power from the resonant ring to the power source. The 'Downstream' is the power delivered to the dummy load after the 11 dB hybrid. Figure 5.9 shows the measured and simulated power ratio to the input power of the resonant ring compared to the operating frequency. The maximal power gain is 12.23 dB at a frequency of 1.2995 GHz, and the corresponding power ratio to input of 'Pb', 'Downstream' and 'Input-r' are -14.73 dB, -12.43 dB and -34.01 dB respectively. The calculated maximal power gain is 13.1 dB, with a measured one turn power loss of -0.14 dB [25].

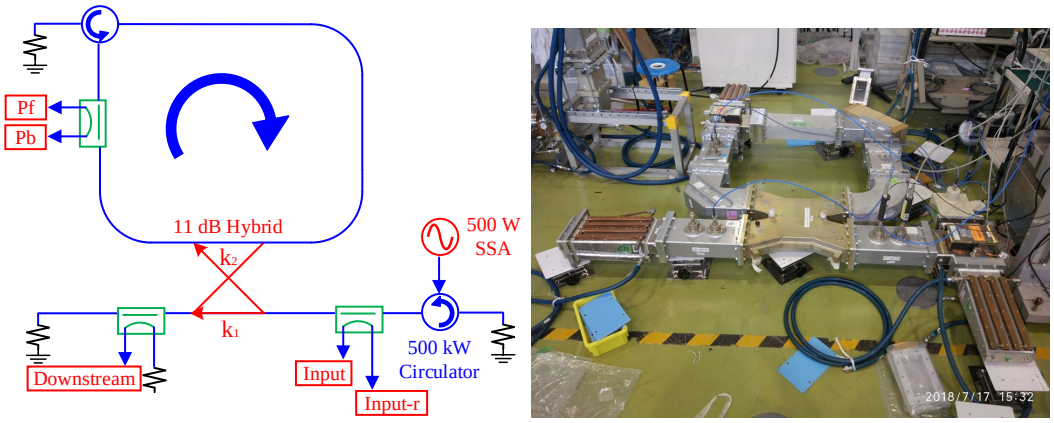

(a) Construction. k_1^2 is -0.41 dB and k_2^2 is -11.17 dB.

(b) Image

Figure 5.8: Construction details and image of the resonant ring with pressurized components.

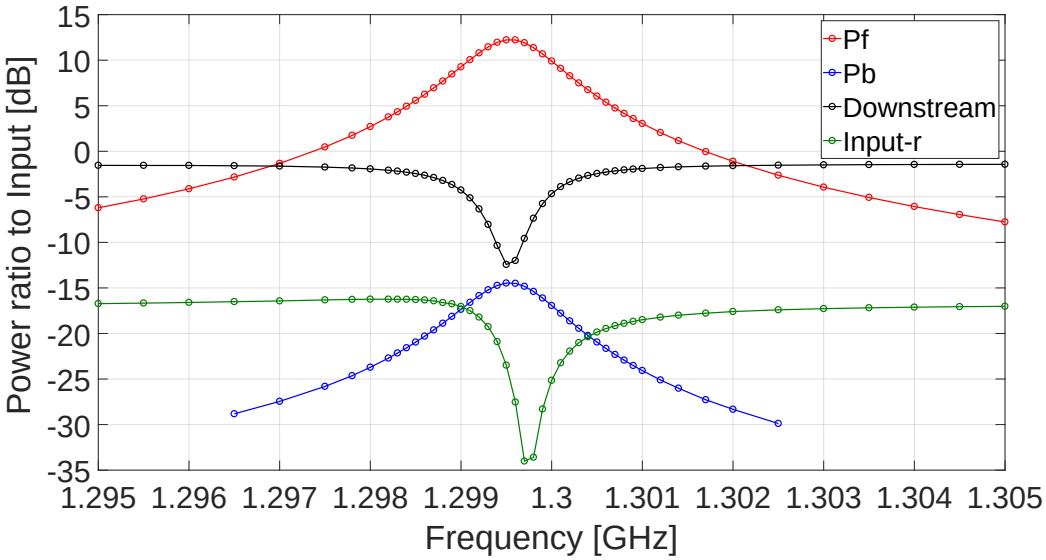

Figure 5.9: Measured power ratio to input power of the resonant ring compared to the operating frequency. The maximal power gain is 12.2 dB at a frequency of 1.2995 GHz and the corresponding power ratio to input of 'Pb', 'Downstream' and 'Input-r' are -14.7 dB, -12.4 dB and -34.0 dB respectively.

The 500 kW circulator cannot be used for the high power operation. Moreover, it is difficult to design the 5 MW circulator due to the arcing problem. The circulator in the resonant ring is removed and the low power test is performed again. Figure 5.10 shows the construction details and an image of the resonant ring without the circulator. The geometric length of the resonant ring is adjusted to be close to optimal condition at frequency of 1.3 GHz. Figure 5.11 shows the measured and simulated power ratio to input power of the resonant ring compared to the operating frequency. Two peaks of 'Pf' are generated when the frequency is shifted in the vicinity of 1.3 GHz. The left peak of the power gain is 9.2 dB at a frequency of 1.2988 GHz, and the corresponding power ratio to input of 'Pb' and 'Downstream' are 7.9 dB and -15.0 dB, respectively. The right peak of the power gain is 9.9 dB at a frequency of 1.3017 GHz, and the corresponding power ratio to input of 'Pb' and 'Downstream' are 9.0 dB and -16.5 dB, respectively. The test result is evidently different when a circulator is inserted. The calculated power gain is 14.6 dB based on the power loss of -0.05 dB, k_1^2 of -0.41 dB and k_2^2 of -11.17 dB. The maximal power gain is reduced from the simulated value of 14.6 dB to the measured value of 9.9 dB. Compared to the case with the circulator, the relative 'Pb' increased from -14.7 dB to 9.0 dB, and the optimal frequency shifted from 1.2995 GHz to 1.3017 GHz. The deviated

value between the optimal frequency and 1.3 GHz is larger. The test result indicates that the power gain exhibits a pronounced decrease, whereas the backward power is increased significantly without the circulator. A high standing wave is generated due to the high backward power. Given that the resonant ring is the traveling wave system for the high power test, the high standing wave will cause an error in the tested power.

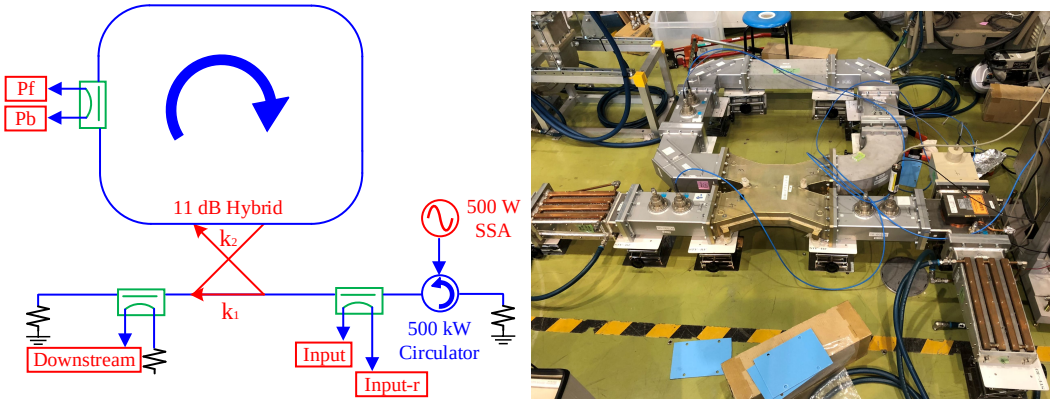

(a) Construction. k_1^2 is -0.41 dB and k_2^2 is -11.17 dB.

(b) Image.

Figure 5.10: Construction details and image of resonant ring without circulator.

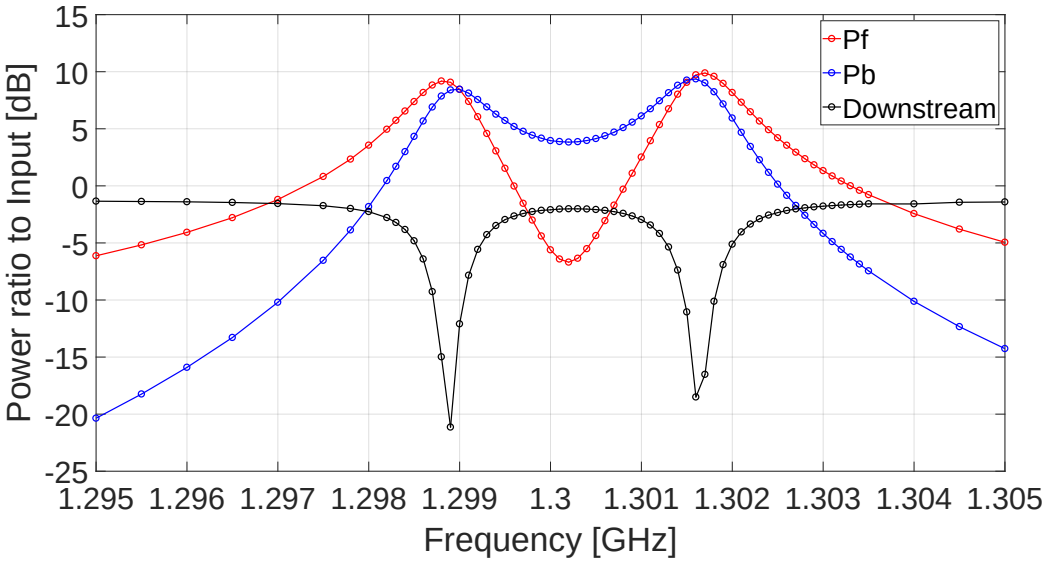

Figure 5.11: Measured power ratio to input power of the resonant ring compared to the operating frequency. The left peak of the power gain is 9.2 dB at a frequency of 1.2988 GHz, and the corresponding power ratio to input of 'Pb' and 'Downstream' are 7.9 dB and -15.0 dB, respectively. The right peak of the power gain is 9.9 dB at a frequency of 1.3017 GHz, and the corresponding power ratio to input of 'Pb' and 'Downstream' are 9.0 dB and -16.5 dB, respectively.

Figure 5.12 is simulated 'Pf' and 'Pb' with a reflected coefficient of -20 dB in the resonant ring. Using the simplest assumptions, only one reflected point with a reflected coefficient of -20 dB is set in the simulation. The simulation indicates that even the reflected coefficient of -23 dB will generate high backward power in the resonant ring and the 'Pf' and 'Pb' will be two peaks near the expected frequency of 1.3 GHz. Although the simulation is not consistent with the measurement, the tendency of the two curves is similar. The measurement and simulation emphasize the importance of inserting RF components in the resonant ring to suppress the backward power.

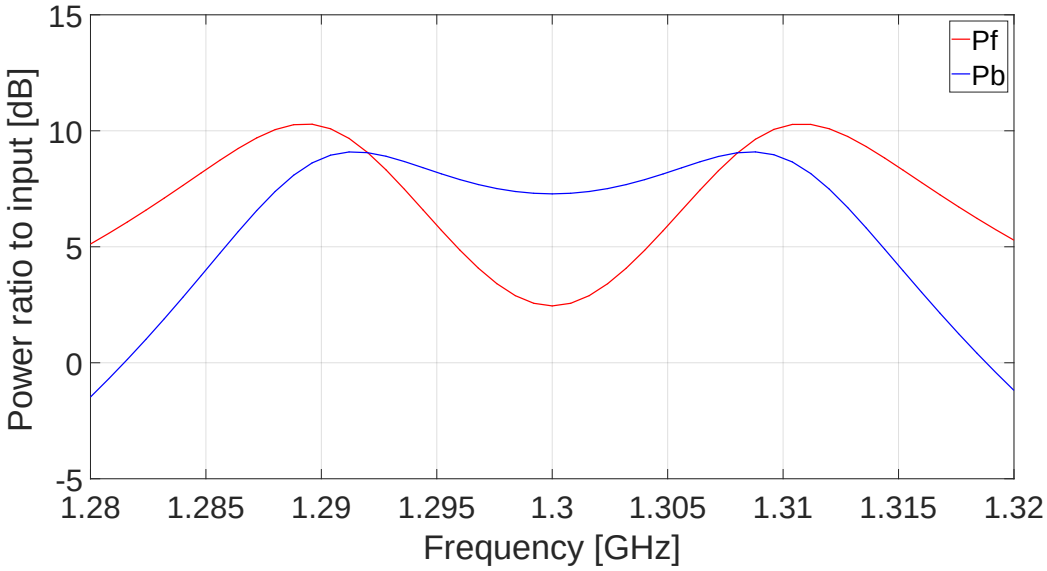

Figure 5.12: Simulated 'Pf' and 'Pb' with a reflected coefficient of -20 dB in the resonant ring.

The 3-stub tuner is widely used in the high power RF system to suppress reflection [8]. Compared to the circulator, the 3-stub tuner has the advantage of high power handling capability, and the disadvantage of a complicated operation. Figure 5.13 shows the structure and equivalent circuit of the 3-stub tuner. The three stubs are arranged on the center line of the waveguide. The space between each stub is usually $\lambda_g/8$, where the λ_g is the guide wavelength at the operating frequency. The admittance of each stub can be changed by adjusting the inserted depth. When represented as an equivalent circuit, each stub is a short-circuited transmission line with an adjustable length that is connected in parallel with the main transmission line. The parallel circuit is usually analyzed from the view of admittance.

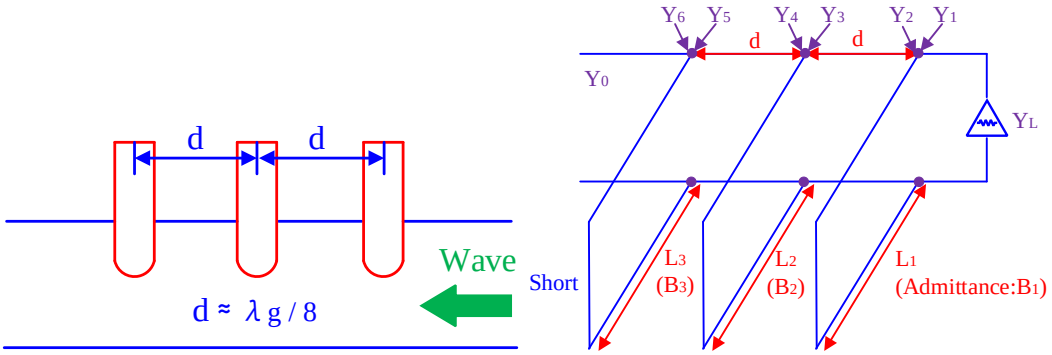

(a) Structure. (b) Equivalent circuit.

Figure 5.13: Structure and equivalent circuit of 3-stub tuner.

The Y_L is the admittance of the load which includes a conductance of G_L and a susceptance of B_L.

$$Y_L = G_L + jB_L \tag{5.12}$$

The B_1, B_2 and B_3 are the susceptance of three stubs. Based on a simple assumption, the stub is pure susceptance. Y_0 is the admittance of the transmission line. Y_1 to Y_6 are the admittance seen looking into the main transmission line.

$$\begin{aligned}
Y_1 &= Y_L = G_L + jB_L \\
Y_2 &= Y_L + jB_1 \\
Y_3 &= Y_0 \frac{Y_1 + jY_0 t}{Y_0 + jY_1 t} \\
Y_4 &= Y_3 + jB_2 \\
Y_5 &= Y_0 \frac{Y_4 + jY_0 t}{Y_0 + jY_4 t} \\
&= Y_0 \frac{j(B_2 + tY_0) + Y_0 \dfrac{j(B_L + B_1 + tY_0) + G_L}{Y_0 - t(B_1 + B_L - jG_L)}}{Y_0 - t(B_2 + Y_0 \dfrac{(B_L + B_1 + tY_0 - jG_L)}{Y_0 - t(B_L + B_1 - jG_L)})} \\
Y_6 &= Y_5 + jB_3
\end{aligned} \tag{5.13}$$

When the load is matched to the transmission line by the 3-stub tuner, Y_6 is equal to Y_0. B_1, B_2 and B_3 then be determined from this relationship.

$$Y_6 = Y_5 + jB_3 = Y_0 \Rightarrow \begin{cases} Re(Y_5) = Y_0 \\ Im(Y_5) = -B_3 \end{cases} \tag{5.14}$$

Three stubs are required to avoid the forbidden region. The forbidden region can be easily explained using a the Smith chart. Figure 5.14 shows the Smith chart solutions for the 2-stub tuner. The admittance is normalized by the admittance of the transmission line, Y_0. The red circle is the '$1+jB$' circle. All the points on the circle have the same normalization conductance of 1. The green circle is the '$1+jB$' circle rotated by 90°, which is consistent with the $\lambda_g/8$ in the Smith chart. The first stub rotates Y_L to Y_1 (or $Y_1{}'$) along the G circle (conductance circle). The transmission line of $\lambda_g/8$ rotates Y_1 (or $Y_1{}'$) to Y_2 (or $Y_2{}'$). Finally, the second stub rotates Y_2 (or $Y_2{}'$) to Y_0, which is the center of the Smith chart along the G circle. The shadow circle is the forbidden region. If Y_L is in this region, the 2-stub tuner can not transform the Y_L to Y_0. For the 3-stub tuner, if the Y_L is in the shadow circle, the first transmission line of $\lambda_g/8$ can rotate Y_L out of the shadow circle. Then, the situation is the same as that of the 2-stub tuner. Thus, there is no forbidden region for the 3-stub tuner, which means that it can transform any admittance to the transmission line.

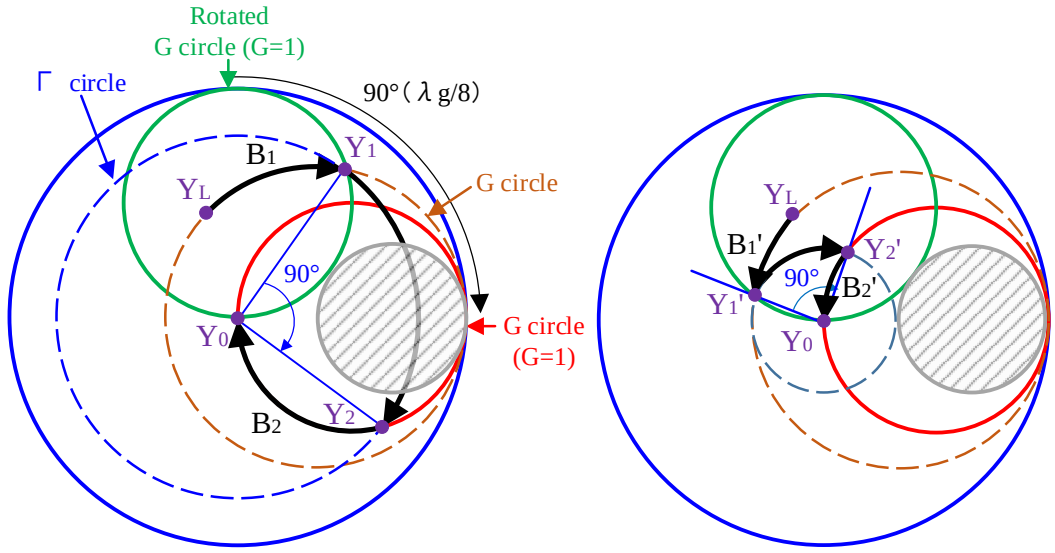

(a) #1 Solution. (b) #2 Solution.

Figure 5.14: Smith chart solutions of the 2-stub tuner. The shadow circle is the forbidden region.

The 3-stub tuner is inserted into the resonant ring and the low power test is again performed. Figure 5.15 shows the construction details and an image of the resonant ring with a 3-stub tuner. Figure 5.16 shows the measured power ratio to input power of the resonant ring compared to the operating frequency. The maximal power gain is 14.8 dB at a frequency of 1.3017

GHz, and the corresponding power ratio to input of 'Pb', 'Downstream' and 'Input-r' are -41.5 dB, -4.2 dB and -15.4 dB respectively. The power gain increased from 9.9 dB to 14.8 dB, and the backward power ratio to input decreased from 9.0 dB to -41.5 dB. The 'Pb'/'Pf' is -56.3 dB. The 3-stub tuner can effectively suppress reflections in the resonant ring. It should be noted that the 3-stub tuner is sensitive to the frequency or the phase of the transmission line. If the frequency or the phase is changed, the suppression effect is adversely affected and the 3-stub tuner should be re-tuned. The calculated maximal power gain is 13.3 dB based on a one turn loss of -0.04 dB, k_1^2 of -0.41 dB and k_2^2 of -11.17 dB. A possible reason is that the 3-stub tuner transforms the reflection of the circular region and the hybrid to forward power. If k_1^2 does not change, and $k_2^2 = 1 - k_1^2 = -10.5$ dB, the calculated power gain is 14.8 dB, which is consistent with the simulated result.

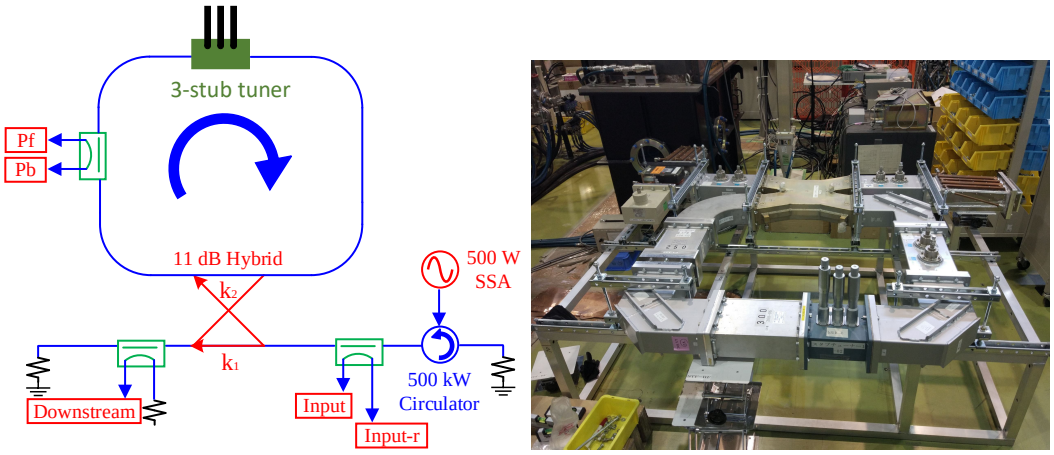

(a) Construction. k_1^2 is -0.41 dB and k_2^2 is -11.17 dB.

(b) Image.

Figure 5.15: Construction details and image of the resonant ring with a 3-stub tuner.

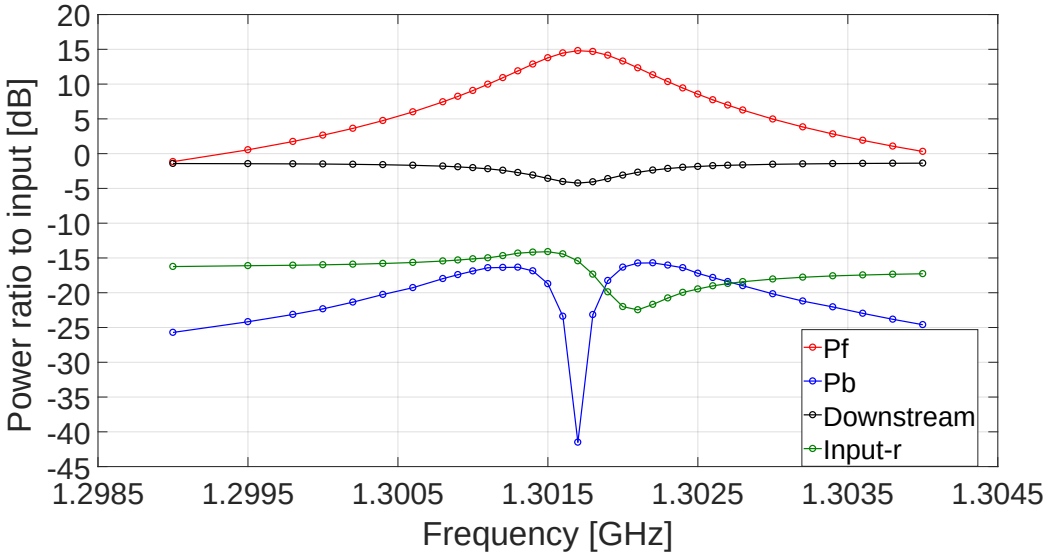

Figure 5.16: Measured power ratio to input power of the resonant ring compared to the operating frequency. The maximal power gain is 14.8 dB at a frequency of 1.3017 GHz and the corresponding power ratio to input of 'Pb', 'Downstream' and 'Input-r' are -41.5 dB, -4.2 dB and -15.4 dB, respectively.

5.4 High Power Operation of L-band Resonant Ring

According to the previous section, the L-band resonant ring will be constructed using pressurized RF components for high power operation. The pressurized 11 dB hybrid is used to couple power into the resonant ring and the 3-stub tuner is used to suppress the backward power. The resonant ring is constructed to test the RF components for the ILC. Thus, the operating frequency should be fixed at 1.3 GHz. The pressurized variable phase shifter is necessary to adjust the resonant ring to the maximal power gain. Figure 5.17 shows the construction details and an image of the 360° phase shifter. This phase shifter consists of one 3 dB hybrid, two WR650 type straight waveguides, and two reflection plates. The length of the two waveguides and the moving distance of the two reflection plates are consistent. In theory, the two reflected waves to port-1 have the same amplitude and phase difference of 180°. Thus, the superposition of the two waves will result in destructive interference. The two reflected waves to port-4 have the same amplitude and the same phase. The input power from port-1 will output from port-4. The

minimum resolution of the moving distance of the reflection plate is 0.1 mm. When the reflection plate is moved 1.0 mm, the effective length of the phase shifter will change by 2.0 mm, and the phase changes 2.2°. The moving range of the reflection plate is 190 mm. Thus, the adjusted range of the phase of this phase shifter can be more than 360°.

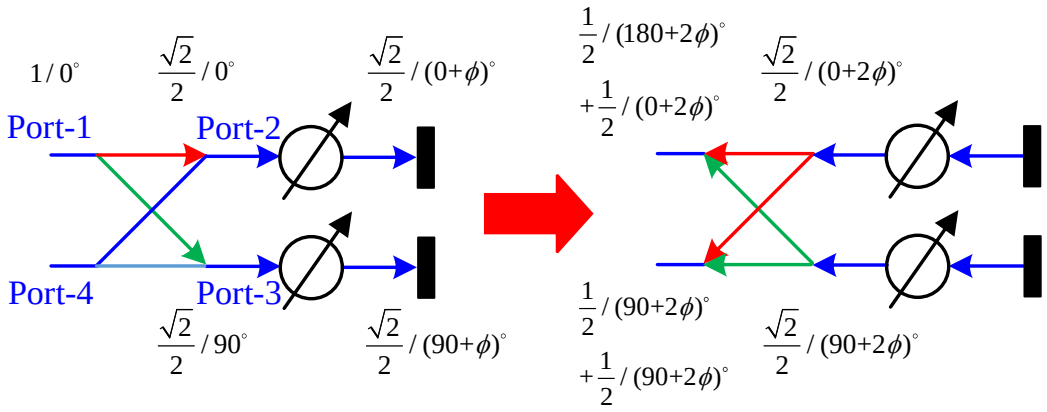

(a) Construction. The note is the amplitude and phase of the wave.

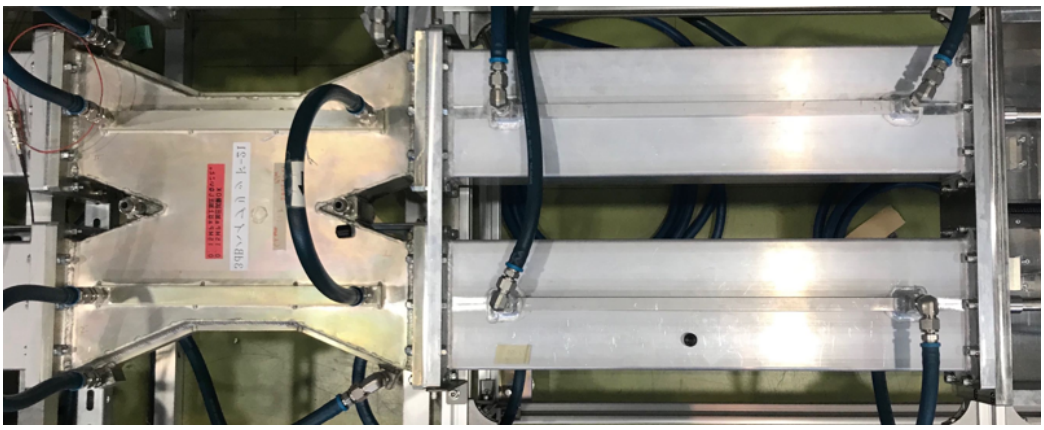

(b) Image.

Figure 5.17: Construction details and image of the 360° phase shifter. The 360° phase shifter consists of one 3 dB hybrid, two WR650 type straight waveguides, and two reflection plates.

Figure 5.18 shows the construction details and an image of the resonant ring for the high power test. Four RF windows are installed in the resonant ring. In the high power test of the resonant ring, the device under test (DUT) is the straight waveguide. The section of DUT is filled with air at standard atmospheric pressure, and the other region of the resonant ring is pressurized using SF_6 gas at 0.1 MPa [26]. The break down voltage can be increased with

the increase of the pressure. The 3 dB hybrid in the 360° phase shifter can only be pressurized to 0.15 MPa, otherwise, leakage of the SF_6 gas occurs. The other components of the resonant ring can be pressurized to more than 0.2 MPa. From a safety standpoint, the resonant ring is pressurized using SF_6 gas at 0.1 MPa. The 800 kW modulated-anode klystron is used as the power source. Based on the low power test of the resonant ring, a power gain of more than 13 dB can be achieved. Thus, an input power of less than 250 kW can generate a forward power of more than 5 MW in the resonant ring. The 500 kW circulator can be used to protect the klystron.

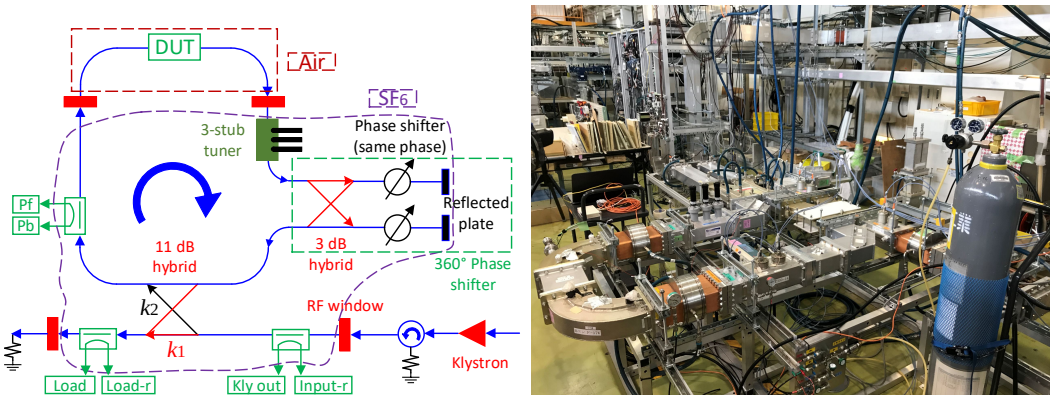

(a) Construction. (b) Image.

Figure 5.18: Construction details and image of the resonant ring for high power test.

Ten acoustic sensors are installed on the different position of the resonant ring. The delay of the waveform of acoustic sensors can approximately indicate the arcing position. The arcing waveguide is cleaned or replaced to improve the operating power. Figure 5.19 shows the calibration for the amplitude of the waveform to the power of the signal for the interlock system in the resonant ring. The waveform of the signal in the resonant ring is monitored using the oscilloscope, and the data are automatically stored. The relationship between the amplitude of the waveform and the power is not linear. Thus, a calibration is performed. Table 5.1 shows the calibrated parameters for the amplitude of the waveform to the power of the signal for the interlock system in the resonant ring. The relationship between the amplitude of the waveform V and the power P can be expressed as $P = a \times V^2 + b \times V + c$.

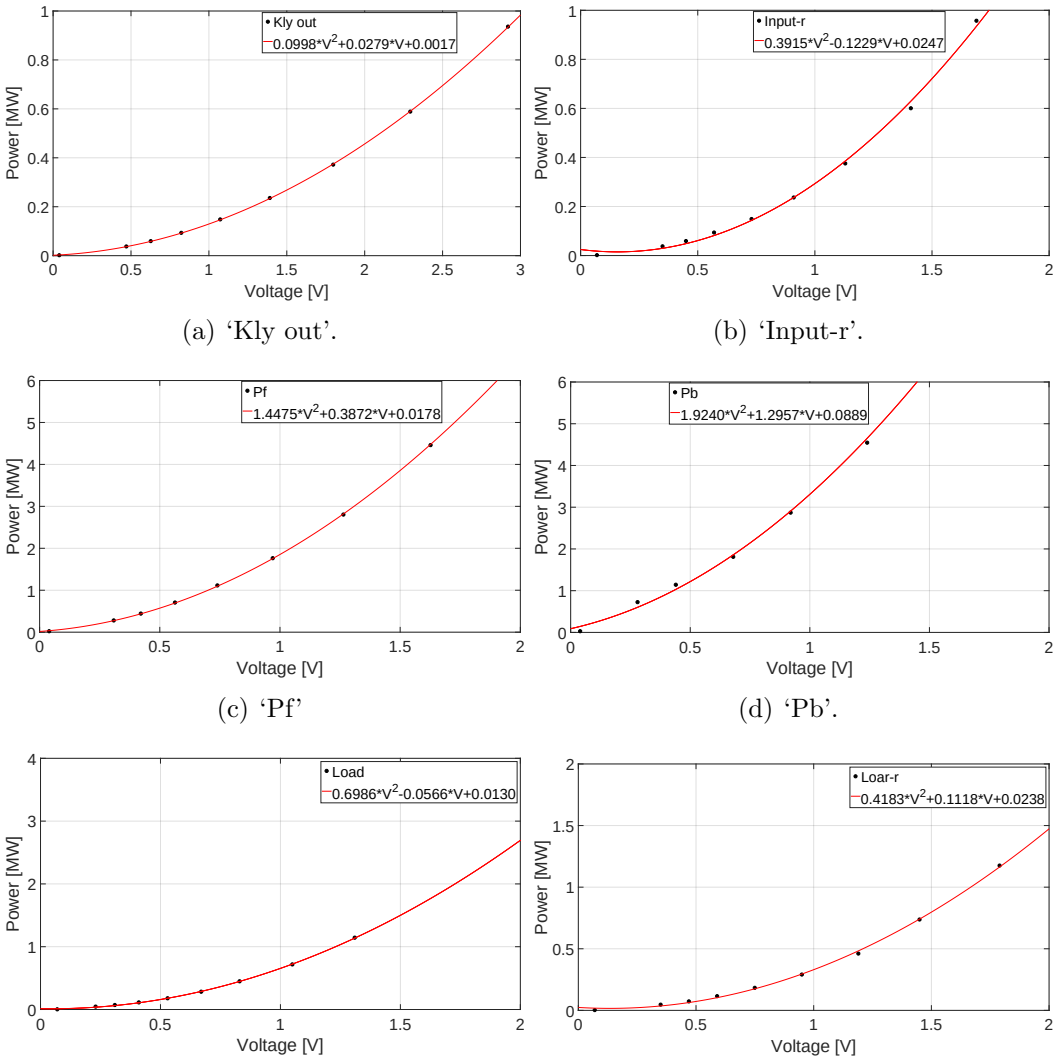

(a) 'Kly out'. (b) 'Input-r'.

(c) 'Pf' (d) 'Pb'.

(e) 'Load'. (f) 'Load-r'.

Figure 5.19: The calibration for the amplitude of the waveform to the power of the signal for the interlock system in the resonant ring.

Table 5.1: The calibrated parameters for the amplitude of the waveform to the power of the signal for the interlock system in the resonant ring. $P = a \times V^2 + b \times V + c$.

	a	b	c
'Kly out'	0.0998	0.0279	0.0017
'Input-r'	0.3915	-0.1229	0.0247
'Pf'	1.4475	0.3872	0.0178
'Pb'	1.9240	1.2957	0.0889
'Load'	0.6986	-0.0566	0.0130
'Load-r'	0.4183	-0.1118	0.0238

Figure 5.20 shows the power of the signal in the resonant ring and the 'RF Status' when arcing occurs. The 'RF status' is the waveform of the RF switch. A arcing happens at approximately -5 μs, 'Pf' decreases and 'Pb' increases. The RF switch is shut down at 0 μs. The output power of the klystron is shut down at approximately 0.5 μs. 'Pf' and 'Pb' are decreased to approximately 0 W at approximately 2 μs. The acoustic sensor can shut down the power in the resonant ring within 7 μs after arcing occurs.

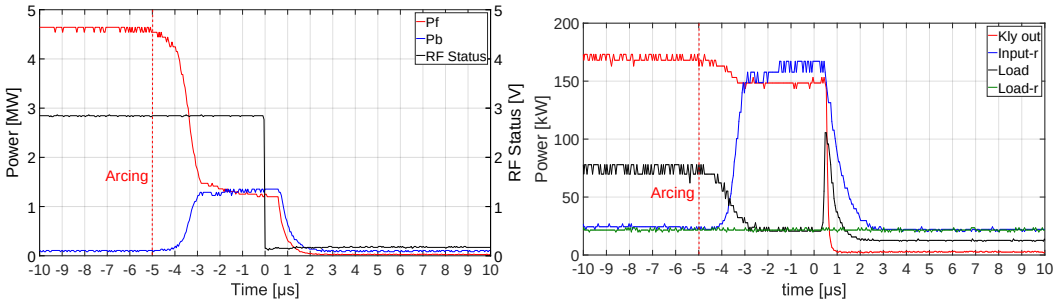

(a) Power and 'RF status'.

(b) Power.

Figure 5.20: The power of the signal in the resonant ring and the 'RF Status' when arcing occurs. The 'RF Status' is the waveform of the RF switch.

Until September of 2019, 4.50 MW with a pulse width of 1.65 ms and a repetition rate of 5 Hz was achieved. Figure 5.21 shows the status of the high power operation of the L-band resonant ring without arcing. Table 5.2 shows the result of the high power operation of the L-band resonant ring without arcing. The resonant ring can be operated with a power of 4.50 MW, and a pulse width of 200 μs for 99 minutes, and a pulse width of 1.65 ms for 120 minutes without arcing. After this operation time, the power source is shut down to complete the test. For the condition when

the forward power is maintained at 4.50 MW with a pulse width of 200 μs, the average power is approximately 4.5 kW and the output power of the klystron is also maintained at 145 kW. In the case of forward power of 4.50 MW with a pulse width of 1.65 ms, the average power is approximately 37 kW. The temperature of the waveguide system increases significantly. The waveguide is deformed, and this deformation causes the one turn phase to be shifted from the optimal condition. Thus, the power gain is decreased. The output power of the klystron is increased to maintain the forward power in the resonant ring at 4.50 MW. During the 120 minutes operation, the output power is increased from 162 kW to 291 kW, and the power gain decreases from 14.4 dB to 11.9 dB.

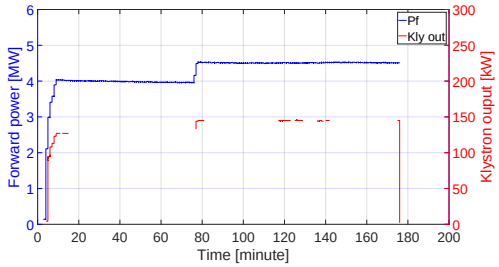

(a) Pulse width of 200 μs. 'Pf' is maintained at 4.50 MW for 99 minutes without arcing. 'Kly out' is maintained at 145 kW.

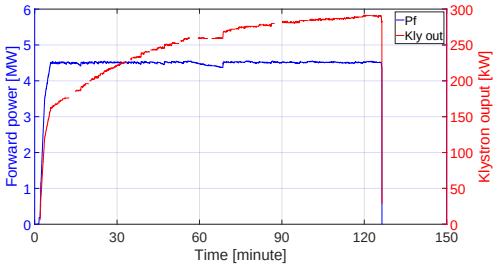

(b) Pules width of 1.65 ms. 'Pf' is maintained at 4.50 MW for 120 minutes without arcing. 'Kly out' is increases from 162 kW to 291 kW.

Figure 5.21: Status of the high power operation of the L-band resonant ring without arcing.

Table 5.2: Result of the high power operation of the L-band resonant ring without arcing. After the operation time, the power source is shut down to complete the test.

Power	Pulse width	Operated time
4.50 MW	200μs	99 minutes
4.50 MW	1.65 ms	120 minutes

5.5 Test Plan of RF Components using resonant ring

The motivation for the use of the resonant ring for high power test of the RF components is to generate more power compared to the power source. Based

on the discussion in the previous section and the shown in Fig. 5.18, the DUT is inserted between the two RF windows in the resonant ring. The maximal power gain of the resonant ring is determined by the one turn power loss of the circular region, and the coupling ratio of the hybrid. Thus, the DUT of the two ports such as that of the phase shifter, can be directly inserted into the resonant ring.

In the case of the hybrid, a component of the power will be coupled to the bypass and the one turn power loss of the resonant ring will be significantly increased if a hybrid is directly inserted into the resonant ring. Figure 5.22 shows the construction details of the resonant ring for testing the variable hybrid. The two variable hybrids are tested together. The phase difference between the main channel and the bypass between the two variable hybrids is 180°. The transmitted (k_1) and coupling (k_2) coefficients of the two variable hybrids are set to the same value [26]. It is assumed that the variable hybrid is an ideal model, which means that there is no power loss and no power is delivered from 'Port-1' to 'Port-4' for each variable hybrid. Thus, all the input power from 'Port-1' of 'VHB-1' is outputted from 'Port-2' of 'VHB-2'.

In a real case, a component of the input power from 'Port-1' will be delivered to 'Port-4'. In addition, the two variable hybrids are not identical, and it is difficult to determine the exact value of k_1 and k_2 of the two variable hybrids. Difficulty is encountered in setting the two variable hybrids. Two directional couplers are installed between the variable hybrids and dummy loads to monitor the power delivered to the dummy load. During the setting of the two variable hybrids, the coupling ratio of the two variable hybrids, 3-stub tuner, and 360° phase shifter are adjusted. The power delivered to the dummy load after 'VHB-2' (signal of 'VHB-L2') and the backward power in the resonant ring (signal of 'Pb') should be very low.

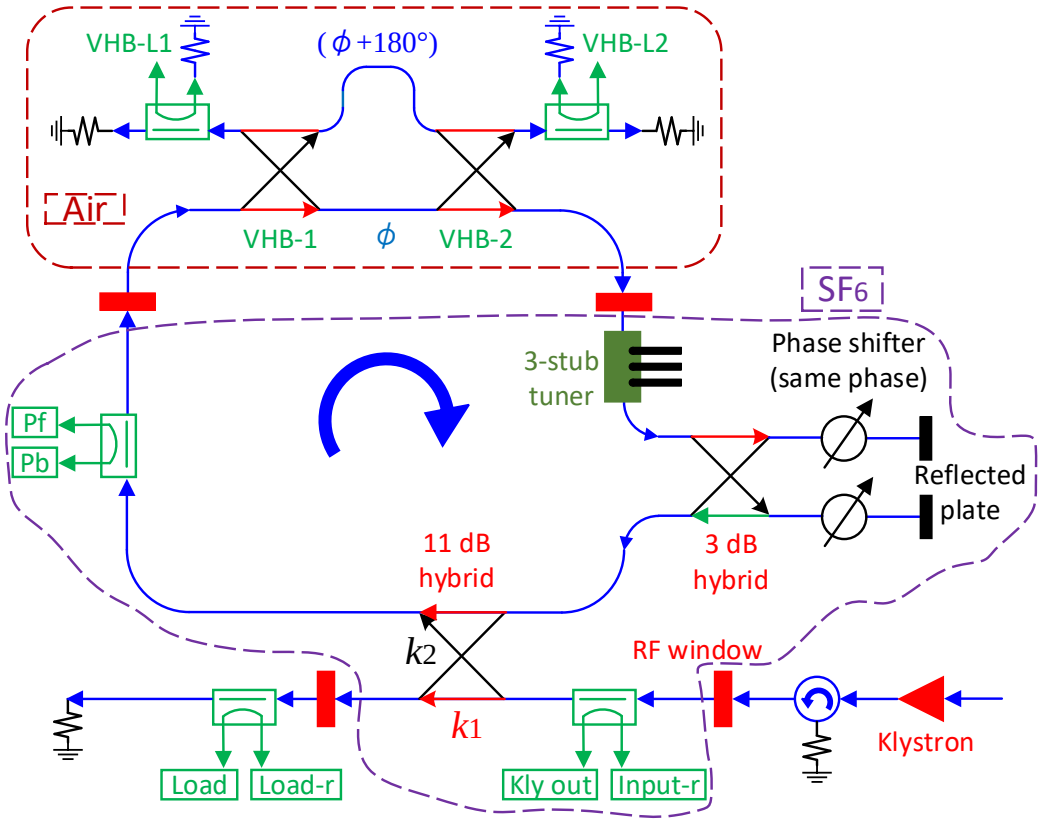

(a) Construction.

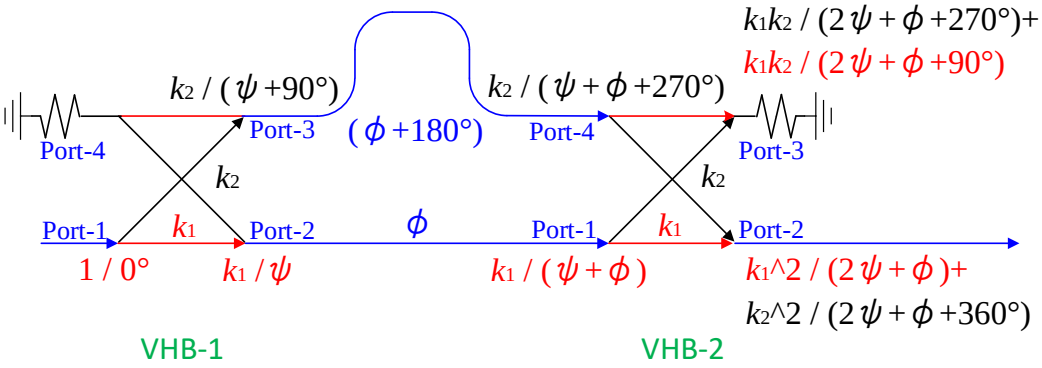

(b) Signal in the two variable hybrids.

Figure 5.22: Construction of a resonant ring for testing the variable hybrid (VHB).

Chapter 6

Evaluation of the RF Components for Compact LPDS

To demonstrate the feasibility of the compact LPDS in the STF at KEK, four variable phase shifters, three variable hybrids, and four fixed phase shifters are manufactured to construct the compact LPDS for four cavities. In this chapter the S parameter and power capability of these RF components are evaluated to satisfy the requirements of the compact LPDS.

6.1 Target of High Power Test

The maximal input power of the compact LPDS is approximately 1.3 MW with a pulse width of 2 ms and a repetition rate of 5 Hz. Considering the worst condition of total reflection, the E-field is double and the power is quadrupled to 5.2 MW. Based on the simulation, the maximal E-field in the variable phase shifter and the variable hybrid can be 1.1 MV/m and 1.0 MV/m, respectively, with a transmitted power of 1.3 MW. These RF components may be damaged at a high power of 5.2 MW with a pulse width of 1.65 ms. The reflected power is monitored as the interlock signal to protect the RF components from arcing. Ten acoustic sensors are installed on the resonant ring to detect the arcing position. As shown in Fig. 5.20, the power is shut down within 7 μs after arcing occurs. Considering some margin of the interlock time, these RF components will be tested at a power of 5.2 MW with a pulse width of more than 50 μs to investigate the situation of total reflection.

Based on the simulation, the reflection of the RF components is less than -29 dB. Considering the margin of reflection, the reflected power is assumed to be 5% of the input power. The magnitude of the E-field of reflection is 22% of the input power. The generated power is 150% of the input power, which is approximately 2 MW if the phase of the reflected signal is the same as that of the input. Thus, these RF components are be tested using a power of 2 MW with a pulse of 2 ms to investigate the situation of normal reflection.

From the previous discussion, these RF components will be tested using a power of 5.2 MW with a pulse width of more than 50 μs, and a power of 2 MW with a pulse width of 2 ms. In the first step of the high power test, the testing time is expected to be more than 30 minutes. Table 6.1 shows the target of the high power test of the RF components of the compact LPDS.

Table 6.1: Target for the high power test of the RF components of the compact LPDS

Power	Pulse Width	Tested time
2 MW	2 ms	$\geq$ 30 minutes
5.2 MW	$\geq$50 μs	$\geq$ 30 minutes

6.2 Evaluation of Variable Hybrid

Figure 6.1 shows an image of the manufactured variable hybrid. The geometric length is measured to be 730 mm. Two aluminum fins are set in the waveguide. Each fin is supported by two aluminum robs. The positions of two fins are adjusted to be symmetrical. A step motor is used to shift the fin.

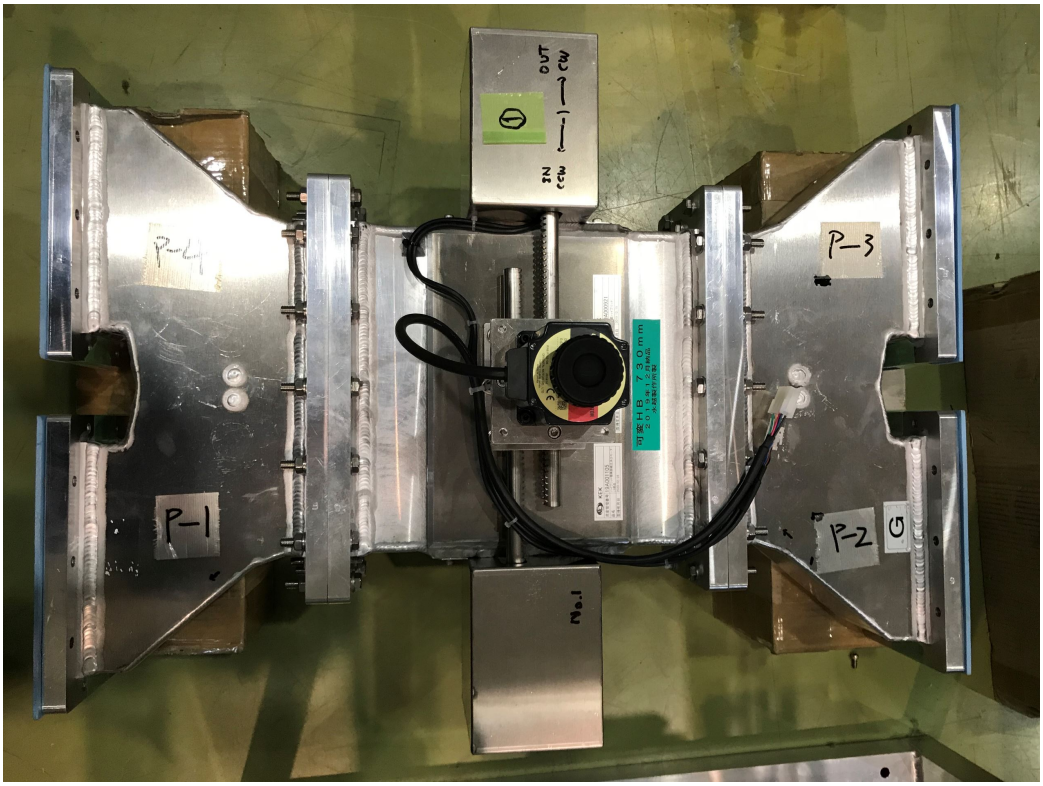

Figure 6.1: Image of the manufactured variable hybrid.

Figure 6.2 shows the measured and simulated magnitude of S_{21} and S_{31} of the variable hybrid. S_{31} can meet the requirement of -8.84 dB to -2.04 dB when the fin is moved from 1.3 mm to 14.8 mm. Figure 6.3 and Figure 6.4 show the measured and simulated magnitude of S_{11} and S_{41} of the variable hybrid, respectively. The measured magnitude of S_{11} and S_{41} are less than -29.00 dB and -26.50 dB respectively when the fin is moved in the required range.

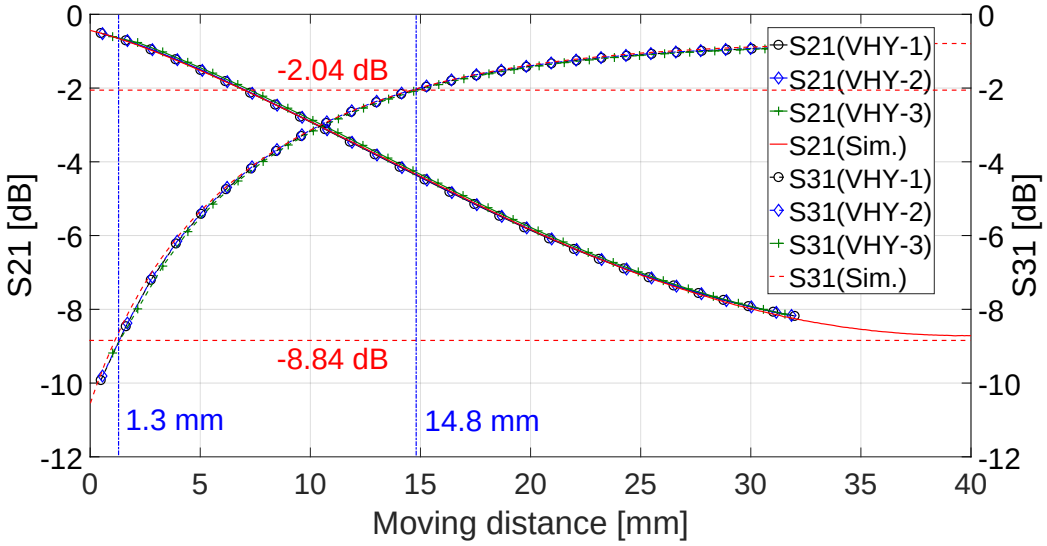

Figure 6.2: Measured and simulated magnitude of S_{21} and S_{31} of the variable hybrid.

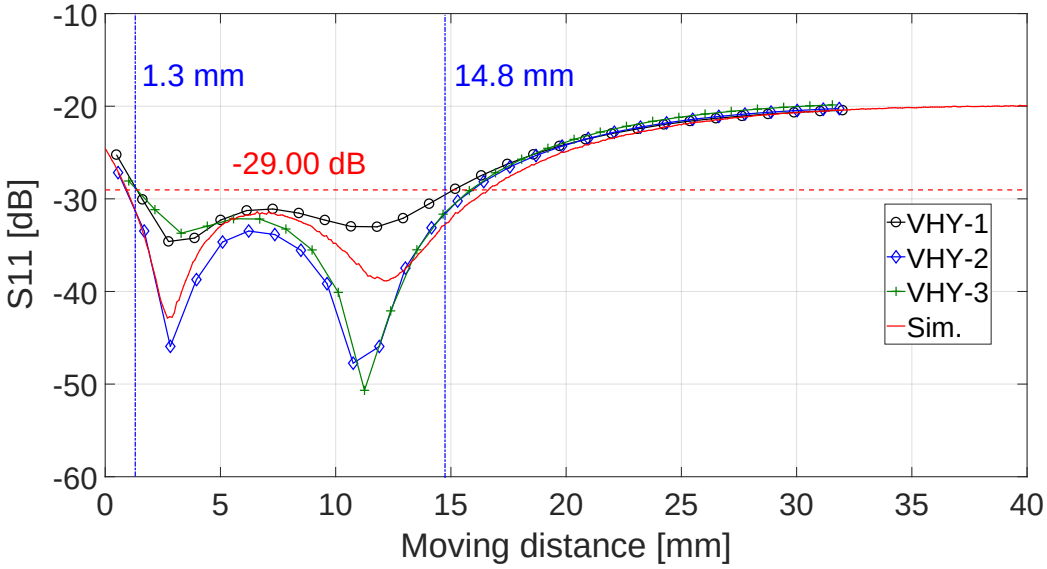

Figure 6.3: Measured and simulated magnitude of S_{11} of the variable hybrid.

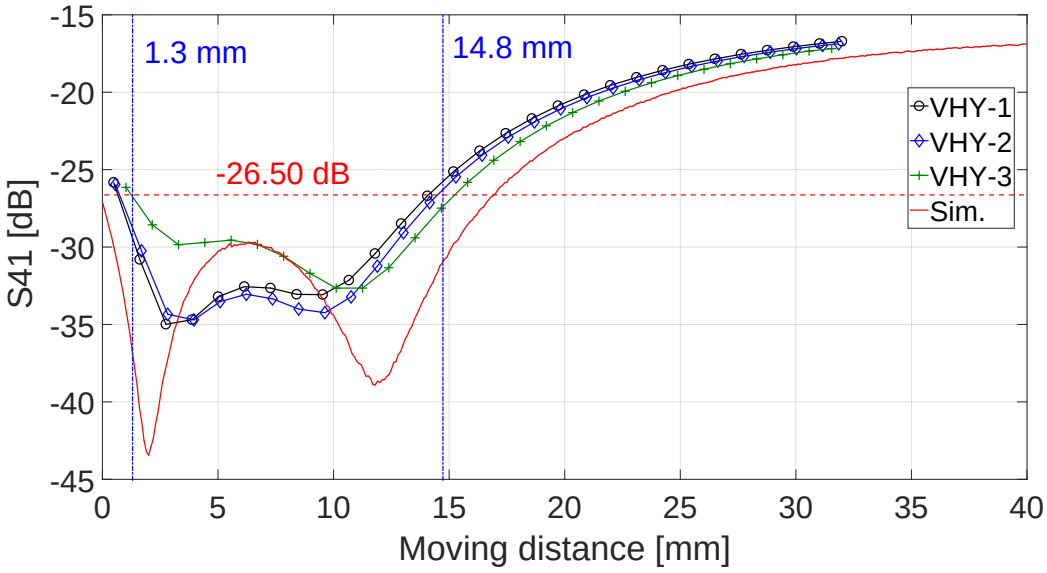

Figure 6.4: Measured and simulated magnitude of S_{41} of the variable hybrid.

Figure 6.5 shows the measured and simulated phase of S_{21} and S_{31} of the variable hybrid compared to the magnitude of S_{31}. The maximal S_{31} phase shift of the three variable hybrids are 17.10°, 17.25° and 16.75° when the power coupling ratio (S_{31}) is changed by ±25% of the average power distributed condition. Compared to the simulated phase shift of 17°, the phase shift of the manufactured variable hybrid can be compensated using the variable phase shifter. The maximal phase difference between the measurement and simulation for S_{21} and S_{31} are 3.3° and 2.3°, respectively, which is within the required range of S_{31}. Considering the 5° margin of the adjusted phase range of the variable phase shifter, this phase difference can also be compensated. The S parameter of the produced variable hybrids can satisfy the requirement of the compact LPDS.

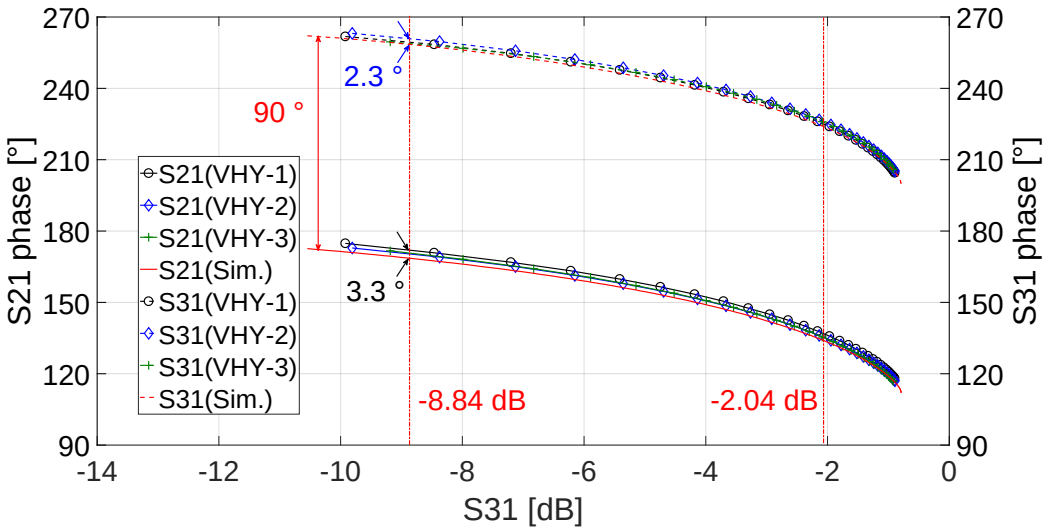

Figure 6.5: Measured and simulated phase of S_{21} and S_{31} of the variable hybrid compared to the magnitude of S_{31}.

Figure 6.6 shows an image depicting the installation of two variable hybrids in the resonant ring. The two variable hybrids are connected by two U-links and a straight waveguide, and are tested together. The geometric length of the bypass is 160 mm longer than that of the main channel between the two variable hybrids to realize a phase difference of 180°. The two directional couplers are installed between the variable hybrid and the dummy load. The coupling ratio of the two variable hybrids can be adjusted according to the power transmitted to the dummy load to increase the power gain of the resonant ring.

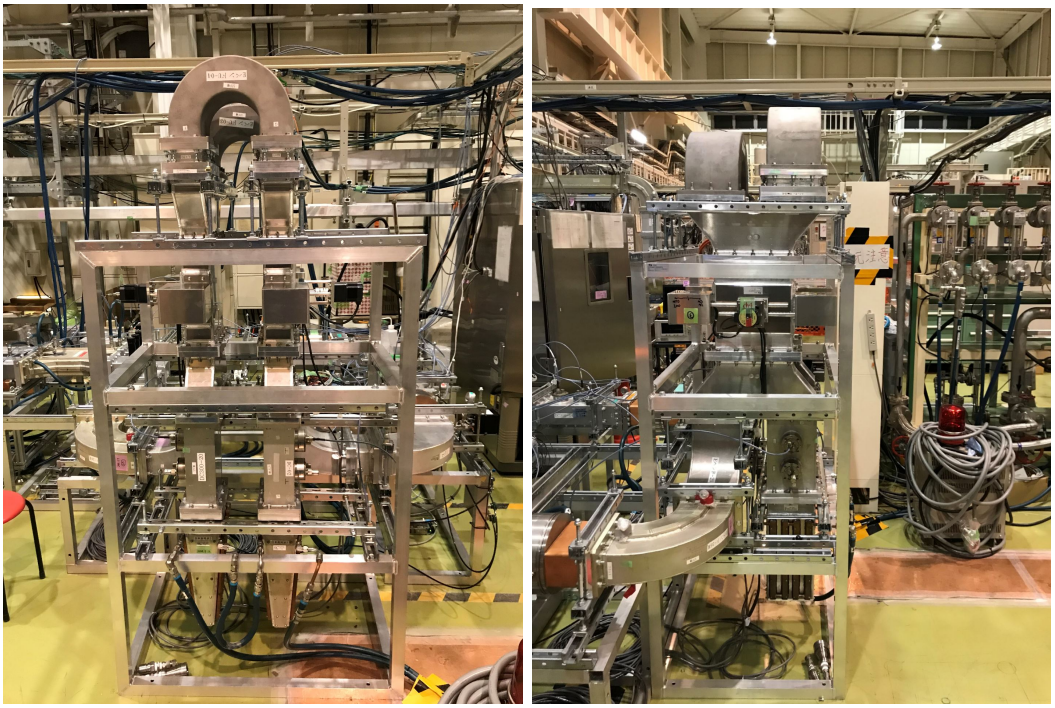

(a) (b)

Figure 6.6: Image depicting the installation of two variable hybrids in the resonant ring.

In the case of the average power distributed condition for a LPDS for five cavities, the coupling ratio (S_{31}) of the variable hybrid is 20%, 25%, 33.3% and 50%. Considering the ±25% margin of power, the maximal coupling ratio is 62.5% when the fin is moved approximately 15 mm. The distance of mechanical limitation should be more than 15 mm. If the distance of mechanical limitation is assumed to be 20 mm, the maximal coupling ratio will be approximately 75%. From the preceding, the high power test of the variable hybrid will focus on the coupling ratio of 20%, 25%, 33.3%, 50%, 62.5% and 75%.

Figure 6.7 shows the high power test of the variable hybrid with a coupling ratio of 20% without arcing. The variable hybrids with a coupling ratio of 20% are operated at a power of 5.2 MW with a pulse width of 200 μs or at 2.0 MW with a pulse width of 2 ms for more than 30 minutes. There is no arcing during the operation. The power source is shut down when the testing time is longer than the target of 30 minutes.

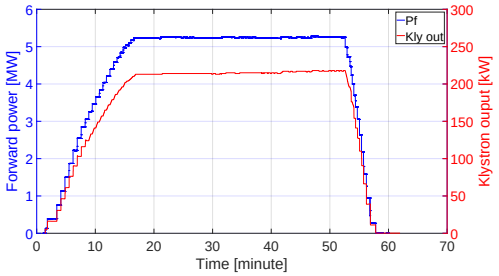

(a) Operation at 5.2 MW power with a pulse width of 200 µs.

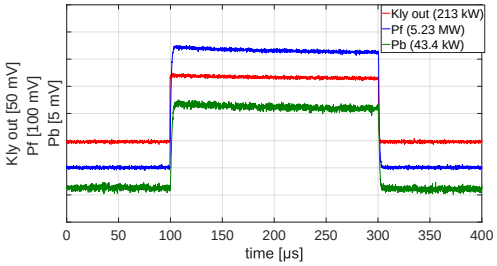

(b) Waveform at 5.2 MW power with a pulse width of 200 µs.

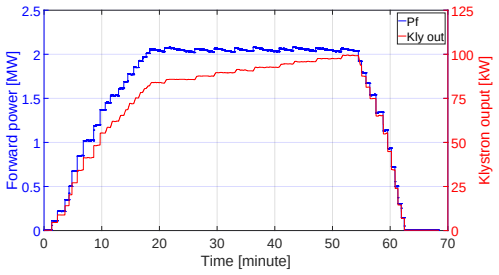

(c) Operation at 2.0 MW power with a pulse width of 2 ms.

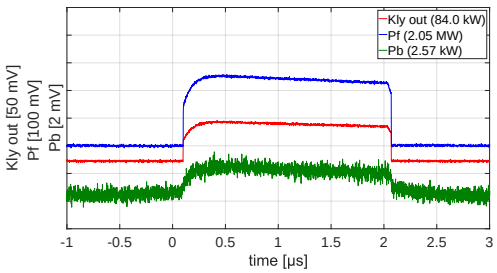

(d) Waveform at 2.0 MW power with a pulse width of 2 ms.

Figure 6.7: High power test of the variable hybrid with a coupling ratio of 20% without arcing. The power source is shut down when the testing time is longer than the target of 30 minutes.

Figure 6.8 shows the high power test of the variable hybrid with a coupling ratio of 25%. The variable hybrid with a coupling ratio of 25% can be operated at a power of 5.2 MW with a pulse width of 200 µs or at 2.0 MW with a pulse width of 2 ms for more than 30 minutes. There is no arcing during the operation. The power source is shut down when the testing time is longer than the target of 30 minutes.

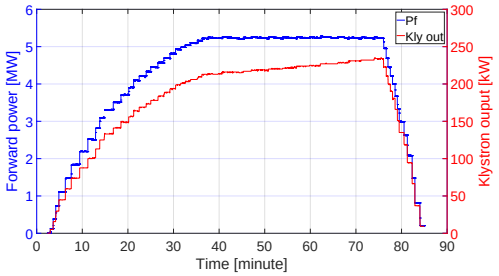

(a) Operation at 5.2 MW with a pulse width of 200 µs.

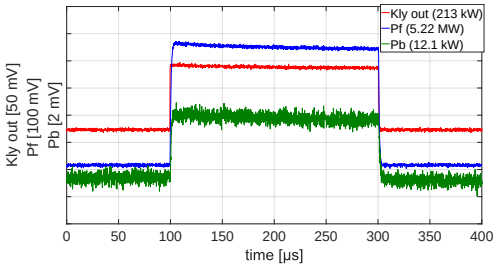

(b) Waveform at 5.2 MW power with a pulse width of 200 µs.

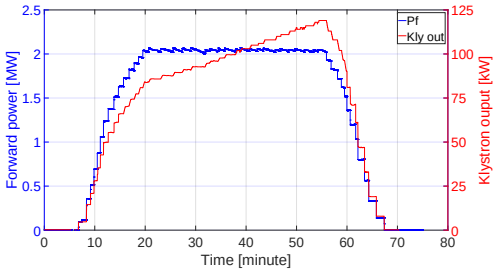

(c) Operation at 2.0 MW power with a pulse width of 2 ms.

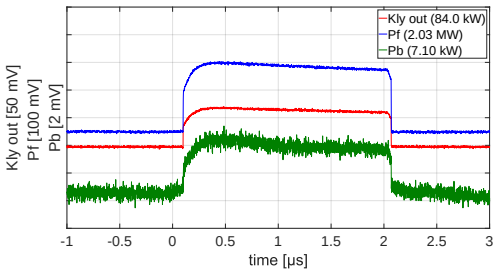

(d) Waveform at 2.0 MW power with a pulse width of 2 ms.

Figure 6.8: High power test of the variable hybrid with a coupling ratio of 25% without arcing. The power source is shut down when the testing time is longer than the target of 30 minutes.

Figure 6.9 shows the high power test of the variable hybrid with a coupling ratio of 33.3% without arcing. The variable hybrid with a coupling ratio of 33.3% can be operated at a power of 5.2 MW with a pulse width of 200 µs or at 2.0 MW with a pulse width of 2 ms for more than 30 minutes. There is no arcing during the operation. The power source is shut down when the testing time is longer than the target of 30 minutes.

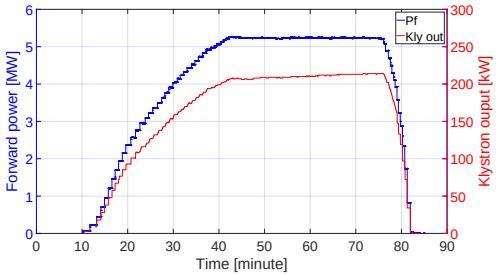

(a) Operation at 5.2 MW power with a pulse width of 200 µs.

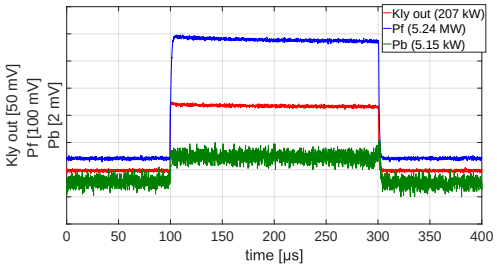

(b) Waveform at 5.2 MW power with a pulse width of 200 µs

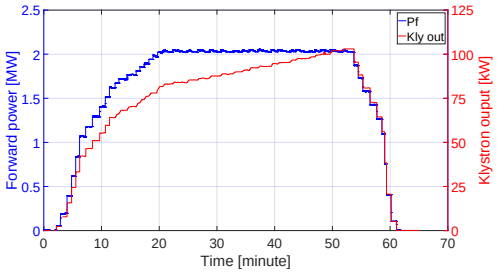

(c) Operation at 2.0 MW power with a pulse width of 2 ms.

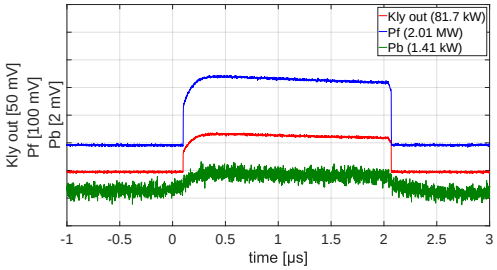

(d) Waveform at 2.0 MW power with a pulse width of 2 ms.

Figure 6.9: High power test of the variable hybrid with a coupling ratio of 33.3% without arcing. The power source is shut down when the testing time is longer than the target of 30 minutes.

Figure 6.10 shows the high power test of the variable hybrid with a coupling ratio of 50% without arcing. The variable hybrid with a coupling ratio of 50% can be operated at a power of 5.2 MW with a pulse width of 200 µs or at 2.0 MW with a pulse width of 2 ms for more than 30 minutes. There is no arcing during the operation. The power source is shut down when the testing time is longer than the target of 30 minutes.

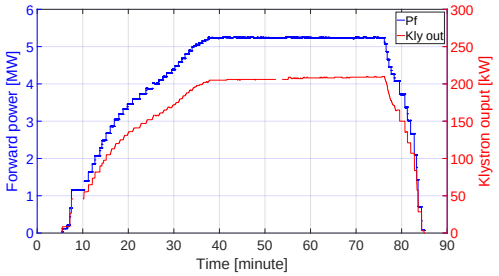

(a) Operation at 5.2 MW power with a pulse width of 200 µs.

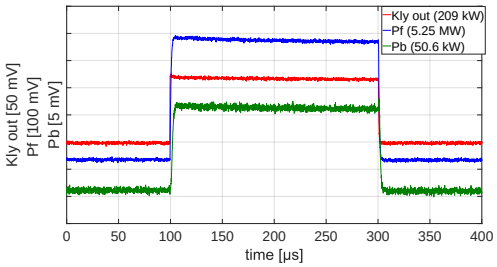

(b) Waveform at 5.2 MW power with a pulse width of 200 µs.

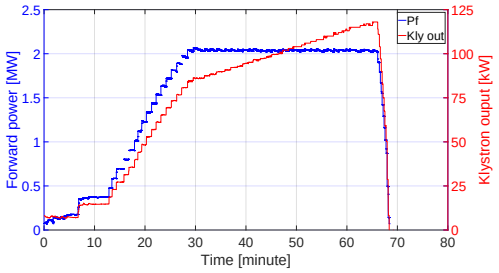

(c) Operation at 2.0 MW power with a pulse width of 2 ms.

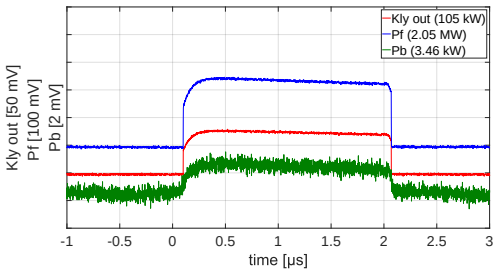

(d) Waveform at 2.0 MW power with a pulse width of 2 ms.

Figure 6.10: High power test of the variable hybrid with coupling ratio of 50% without arcing. The power source is shut down when the testing time is longer than the target of 30 minutes.

Figure 6.11 shows the high power test of the variable hybrid with a coupling ratio of 62.5% without arcing. The variable hybrid with a coupling ratio of 62.5% can be operated at a power of 5.2 MW with a pulse width of 50 µs or at 2.0 MW with a pulse width of 2 ms for more than 30 minutes. There is no arcing during the operation. The power source is shut down when the testing time is longer than the target of 30 minutes. In the case of a power of 5.2 MW with a pulse width of at least 100 µs, arcing occurs in the U-link of the bypass between the two variable hybrids. The 3-stub tuner can only suppress the reflected power in the main road. There, may exist high standing wave in the bypass, leading to arcing.

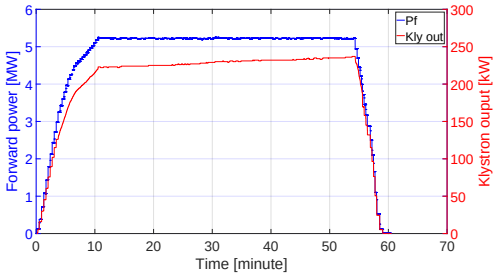

(a) Operation at 5.2 MW power with a pulse width of 50 µs.

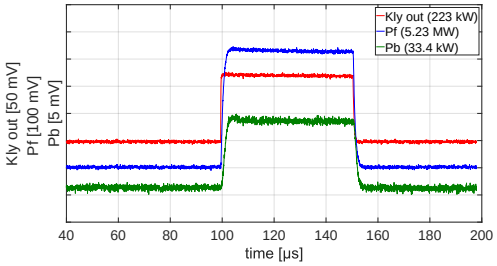

(b) Waveform at 5.2 MW power with a pulse width of 50 µs.

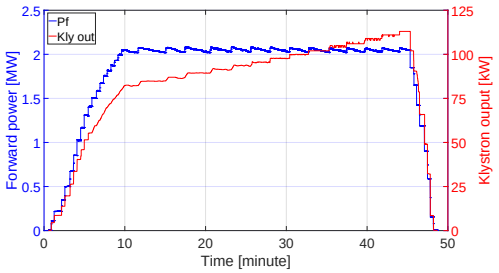

(c) Operation at 2.0 MW power with a pulse width of 2 ms.

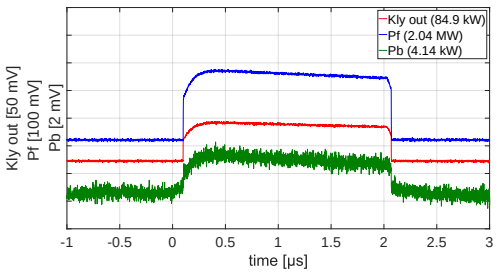

(d) Waveform at 2.0 MW power with a pulse width of 2 ms.

Figure 6.11: High power test of the variable hybrid with a coupling ratio of 62.5% without arcing. The power source is shut down when the testing time is longer than the target of 30 minutes.

Figure 6.12 shows the high power test of the variable hybrid with a coupling ratio of 75% without arcing. The variable hybrid with a coupling ratio of 75% can be operated at a power of 5.2 MW with a pulse width of 50 µs for 24 minutes or at 2.0 MW with a pulse width of 2 ms for more than 30 minutes. In the case of the 50 µs test, the circular power suddenly decreased and cannot be improved due to the maximal output power of the klystron for the current setting. Thus, the power source is shut down and the testing time is less than 30 minutes. There is no arcing during the operation. Arcing also occurs in the U-link of the bypass between the two variable hybrids at 5.2 MW with a pulse width of at least 100 µs.

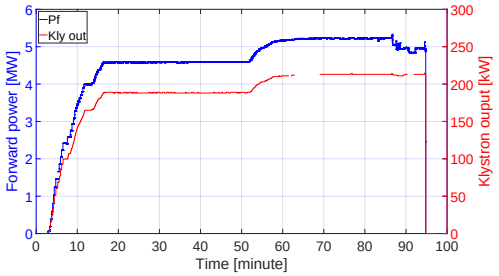

(a) Operation at 5.2 MW power with a pulse width of 50 µs.

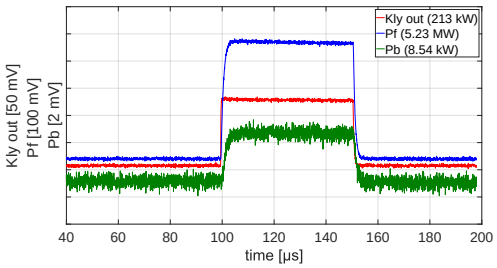

(b) Waveform at 5.2 MW power with a pulse width of 50 µs.

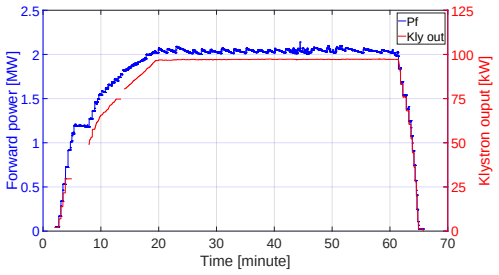

(c) Operation at 2.0 MW power with a pulse width of 2 ms.

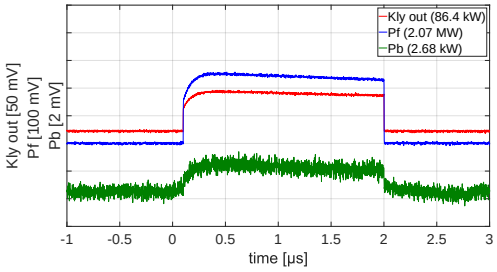

(d) Waveform at 2.0 MW power with a pulse width of 2 ms.

Figure 6.12: High power test of the variable hybrid with a coupling ratio of 75% without arcing.

Table 6.2 shows the result of the high power test of the variable hybrid [28]. Arcing does not occur during these high power test. After the operation, the power source is shut down to complete the test. The power handling capability of variable hybrid can satisfy the requirements of the compact LPDS.

Table 6.2: Result of the high power test of the variable hybrid without arcing [28]. After the operation, the power source is shut down to complete the test.

Coupling ratio ($\|S_{31}\|$)	Power	Pulse width	Operation time
20%	5.2 MW	200 μs	$\geq$ 30 minutes
	2.0 MW	2 ms	$\geq$ 30 minutes
25%	5.2 MW	200 μs	$\geq$ 30 minutes
	2.0 MW	2 ms	$\geq$ 30 minutes
33.3%	5.2 MW	200 μs	$\geq$ 30 minutes
	2.0 MW	2 ms	$\geq$ 30 minutes
50%	5.2 MW	200 μs	$\geq$ 30 minutes
	2.0 MW	2 ms	$\geq$ 30 minutes
62.5%	5.2 MW	50 μs	$\geq$ 30 minutes
	2.0 MW	2 ms	$\geq$ 30 minutes
75%	5.2 MW	50 μs	24 minutes *
	2.0 MW	2 ms	$\geq$ 30 minutes

* The circular power suddenly decreased from 5.2 MW to 5.0 MW after 24 minutes for no known reason, and cannot be improved due to the maximal output power of the klystron at the current setting.

6.3 Evaluation of Variable Phase shifter

Figure 6.13 shows an image of the manufactured variable phase shifter. The geometric length was measured of 300 mm. One aluminum fin is set in the waveguide, and supported by two aluminum robs. A step motor is used to shift the fin.

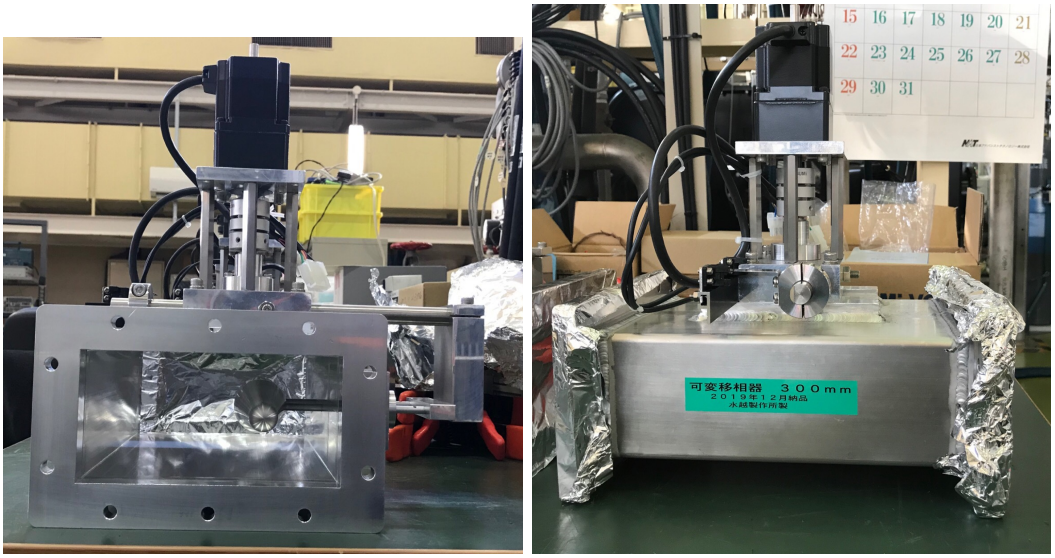

(a) Frount view (b) Side view

Figure 6.13: Image of the manufactured variable phase shifter.

Figure 6.14 shows the measured and simulated S_{11} of four variable phase shifters. S_{11} is less than -30 dB when the fin is moved from 0 to 43 mm. Figure 6.15 shows the measured and simulated transmitted phase of four variable phase shifters. The phase can be adjusted from 36° to −1° when the fin is moved from 0 to 43 mm, which means that the total phase changes by 37°. The phase is approximately 17.5° when the fin is moved approximately 15 mm. The maximal adjusted phase range can be from 36° to −3°. The measured transmitted phase and S_{11} are consistent with the simulated result. Thus the S parameter of the manufactured variable phase shifters can meet the requirements of the compact LPDS.

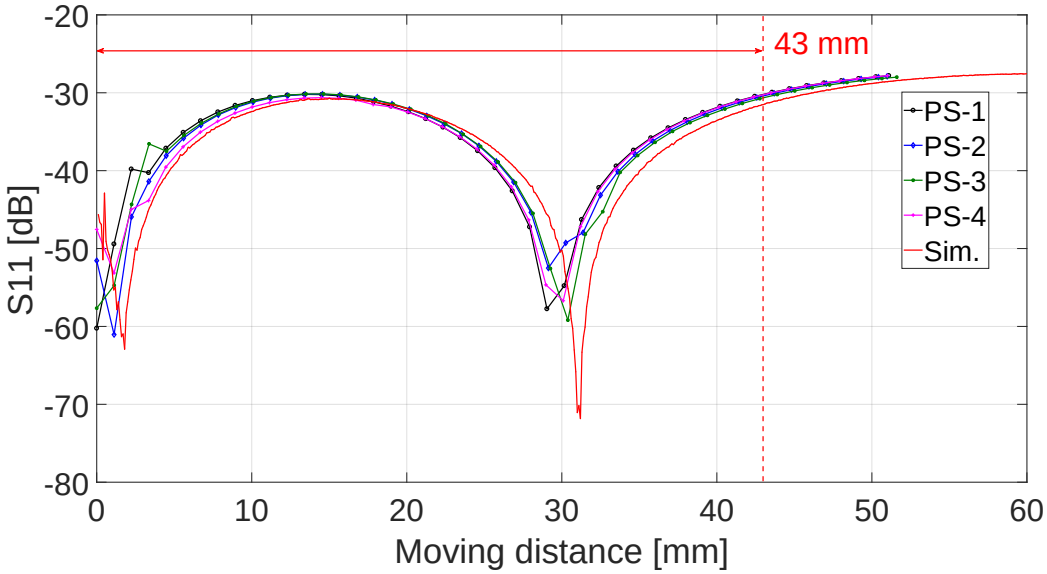

Figure 6.14: Measured and simulated S_{11} of four variable phase shifters.

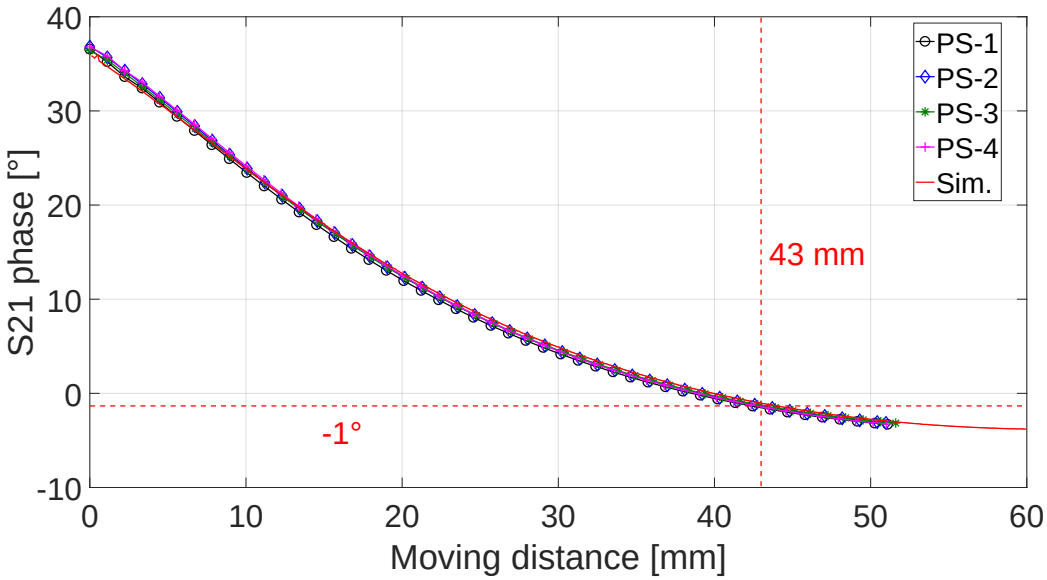

Figure 6.15: Measured and simulated transmitted phase of four variable phase shifters.

Figure 6.16 depicts an image showing the installation for the two variable phase shifters in the resonant ring. Four variable phase shifters are inserted

between two RF windows, filled with air, and tested together. This setup for the testing of the variable phase shifters is similar to the setup for testing the variable hybrid.

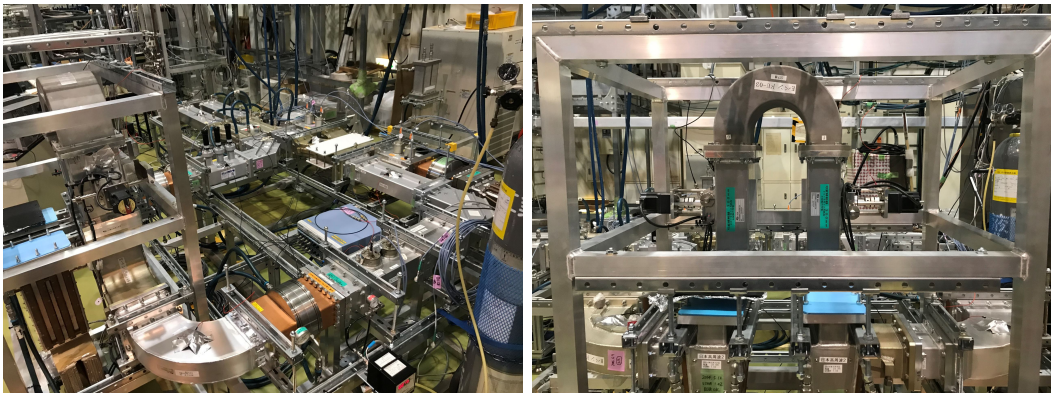

(a) (b)

Figure 6.16: Image depicting the installation of two variable phase shifters in the resonant ring. Four variable phase shifters are tested together.

Three conditions of the variable phase shifters are tested at high power for the case of the fin is close to the wall, at the center of the moving range (movement approximately 21.5 mm), and the end of the moving range (movement approximately 43.0 mm). The 360° phase shifter is used to adjust the one turn phase to the optimal condition to maximize the power gain.

Figure 6.17 shows the high power test result of the variable phase shifter without arcing when the fin is close to the wall. The variable phase shifter can be operated at a power of 5.2 MW power with a pulse width of 200 μs or at 2.0 MW with a pulse width of 2 ms for more than 30 minutes when the fin is close to the wall. There is no arcing during the operation. The power source is shut down when the testing time is longer than the target of 30 minutes.

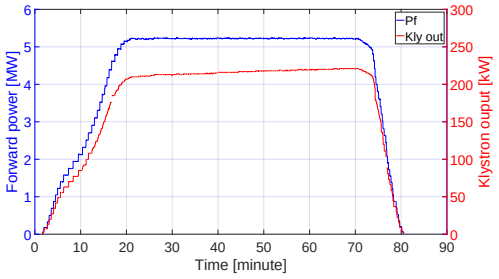

(a) Operation at 5.2 MW power with a pulse width of 200 µs.

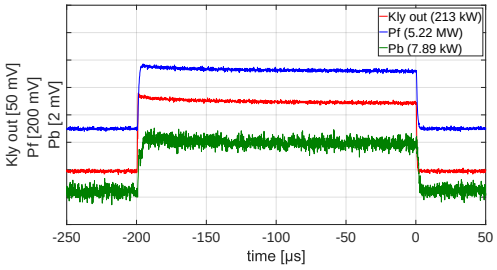

(b) Waveform at 5.2 MW power with a pulse width of 200 µs.

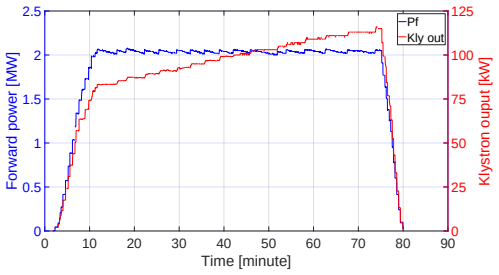

(c) Operation at 2.0 MW power with a pulse width of 2 ms.

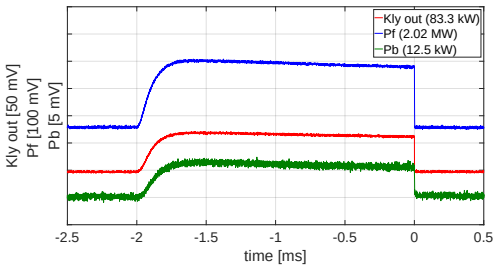

(d) Waveform at 2.0 MW power with a pulse width of 2 ms.

Figure 6.17: High power test result of the variable phase shifter without arcing when the fin is close to the wall. The power source is shut down when the testing time is longer than the target of 30 minutes.

Figure 6.18 shows the high power test result of the variable phase shifter without arcing when the fin is moved to the center of the movement range. The variable phase shifter can be operated at a power of 5.2 MW with a pulse width of 200 µs or at 2.0 MW with a pulse width of 2 ms for more than 30 minutes when the fin is moved to the center of its movement range. There is no arcing during the operation. The power source is shut down when the testing time is longer than the target of 30 minutes.

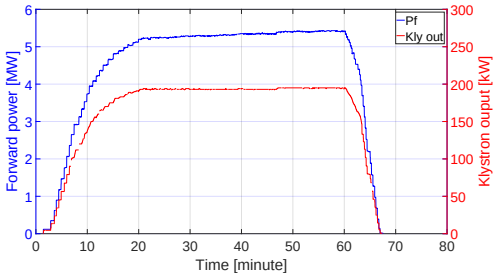

(a) Operation at 5.2 MW power with a pulse width of 200 μs.

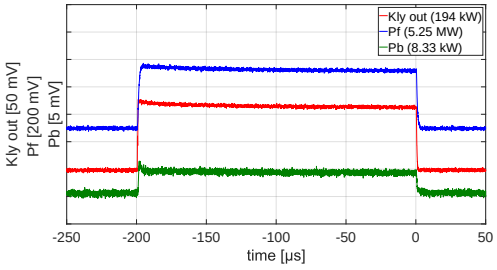

(b) Waveform at 5.2 MW power with a pulse width of 200 μs.

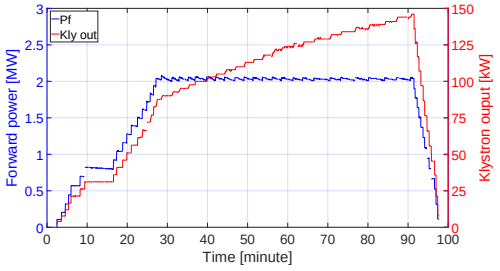

(c) Operation at 2.0 MW power with a pulse width of 2 ms.

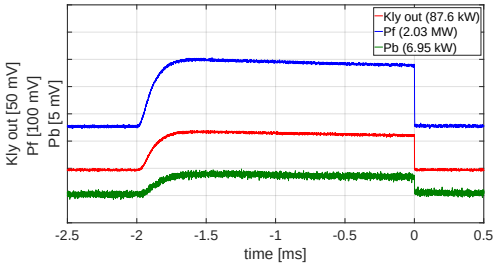

(d) Waveform at 2.0 MW power with a pulse width of 2 ms.

Figure 6.18: High power test result of the variable phase shifter without arcing when the fin is moved to the center of the movement range. The power source is shut down when the testing time is longer than the target of 30 minutes.

Figure 6.19 shows the high power test result of the variable phase shifter without arcing when the fin is moved to the end of the movement range. The variable phase shifter can be operated at a power of 5.2 MW with a pulse width of 200 μs or at 2.0 MW with a pulse width of 2 ms for more than 30 minutes when the fin is moved to the end of its movement range. There is no arcing during the operation. The power source is shut down when the testing time is longer than the target of 30 minutes.

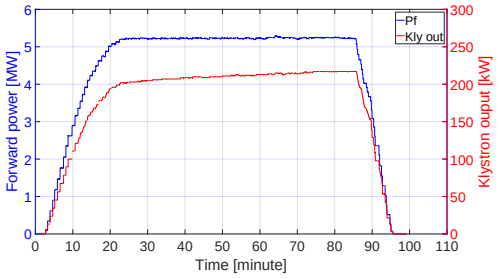

(a) Operation at 5.2 MW power with a pulse width of 200 µs.

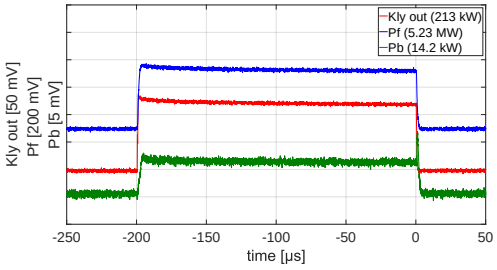

(b) Waveform at 5.2 MW power with a pulse width of 200 µs.

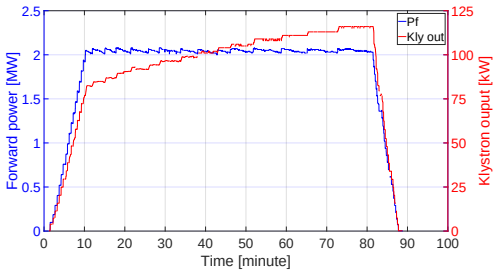

(c) Operation at 2.0 MW power with a pulse width of 2 ms.

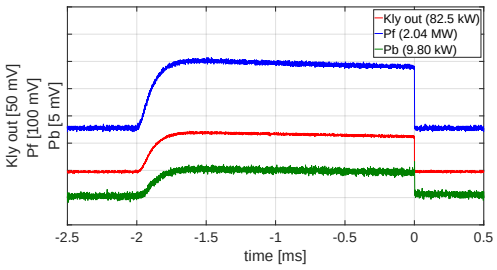

(d) Waveform at 2.0 MW power with a pulse width of 2 ms.

Figure 6.19: High power test result of the variable phase shifter without arcing when the fin is moved to the end of the movement range. The power source is shut down when the testing time is longer than the target of 30 minutes.

Table 6.3 displays the result of the high power test of the variable phase shifters. Arcing does not occur during these high power tests. After the operation, the power source is shut down to complete the test. The power handling capability of the variable phase shifter can satisfy the requirements of the compact LPDS.

Table 6.3: Result of the high power test of the variable phase shifter without arcing. After the operation, the power source is shut down to complete the test.

Position of fin	Power	Pulse width	Operation time
Close to wall	5.2 MW	200 µs	$\geq$ 30 minutes
($\sim$ 0 mm)	2.0 MW	2 ms	$\geq$ 30 minutes
Half of range	5.2 MW	200 µs	$\geq$ 30 minutes
($\sim$ 21.5 mm)	2.0 MW	2 ms	$\geq$ 30 minutes
Maximum of range	5.2 MW	200 µs	$\geq$ 30 minutes
($\sim$ 43.0 mm)	2.0 MW	2 ms	$\geq$ 30 minutes

6.4 Evaluation of Fixed Phase Shifter

Figure 6.20 shows an image of the three manufactured fixed phase shifters. The geometric length is measured to be two 296 mm and a 1,026 mm, respectively.

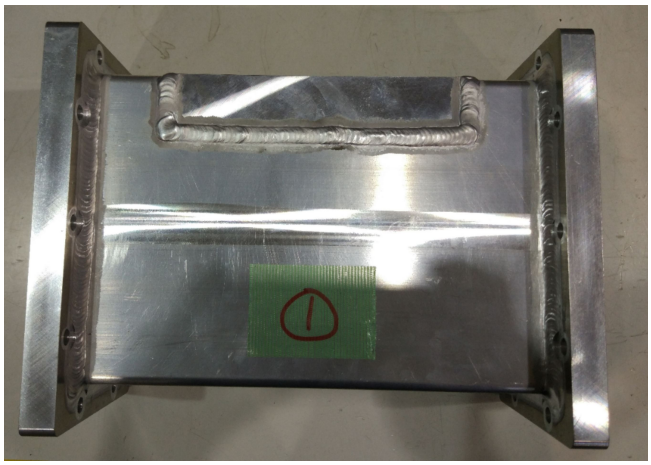

(a) #FPS1

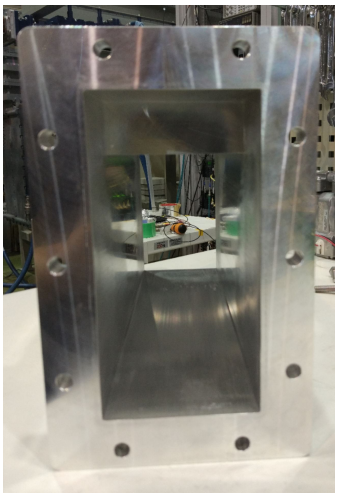

(b) #FPS2

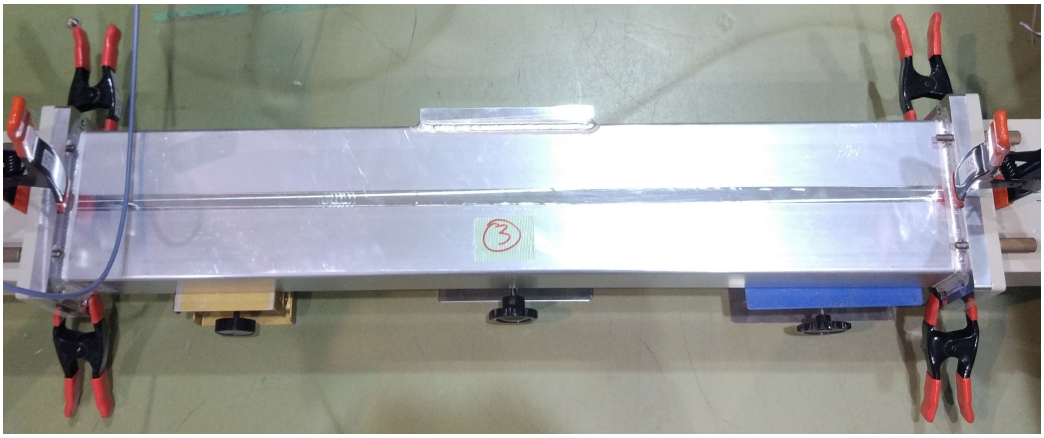

(c) #FPS3

Figure 6.20: Image of the three manufactured fixed phase shifters.

Table 6.4 shows the measured and simulated S parameters of the three fixed phase shifter. The phase difference between the measured and simulated S_{21} is less than 1°. Considering the phase adjusted margin of 15°, this phase difference can be compensated by the variable phase shifter. The measured return loss (S_{21}) is less than -30 dB. The measured S parameter of the three

fixed phase shifters can satisfy the requirements of the compact LPDS.

Table 6.4: Measured and simulated S parameter of the three fixed phase shifters (FPS).

Coupling ratio ($\|S_{31}\|$)	#FPS1	#FPS2	#FPS3
Length	296 mm	296 mm	1026 mm
Simulated S_{21}	95.29°	103.39°	−84.22°
Measured S_{21}	95.50°	102.9°	−84.93°
Measured $\|S_{11}\|$	-34.44 dB	-34.09 dB	-44.03 dB

Figure 6.21 depict an image showing the installation of the three fixed phase shifters in the resonant ring. These three fixed phase shifters are tested together.

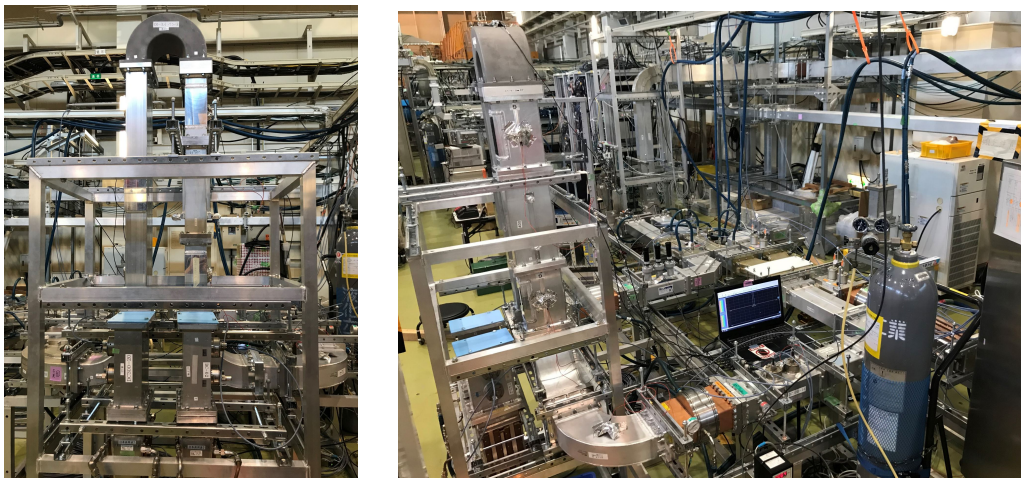

(a) (b)

Figure 6.21: Image depicting the installation of the three fixed phase shifters in the resonant ring.

Figure 6.22 shows the high power test result of the three fixed phase shifters without arcing. The three fixed phase shifters can be operated at a powr of 5.2 MW power with a pulse width of 200 μs or at 2.0 MW with pulse width of 2 ms for more than 30 minutes. There is no arcing during the operation. The power source is shut down when the testing time is longer than the target of 30 minutes.

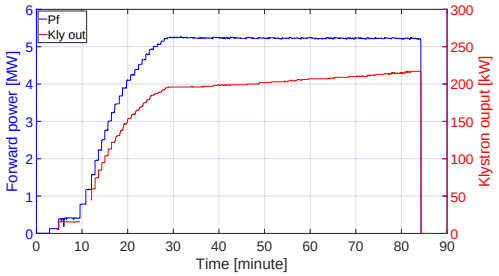

(a) Operation at 5.2 MW power with a pulse width of 200 µs.

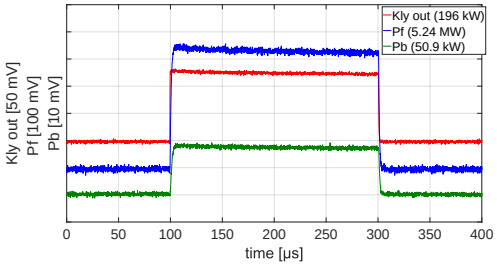

(b) Waveform at 5.2 MW power with a pulse width of 200 µs.

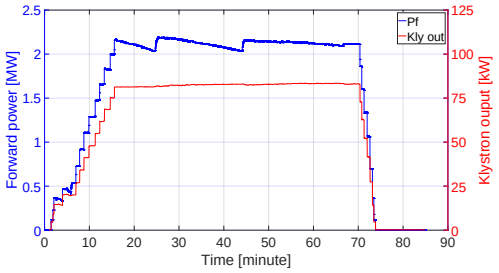

(c) Operation at 2.0 MW power with a pulse width of 2 ms.

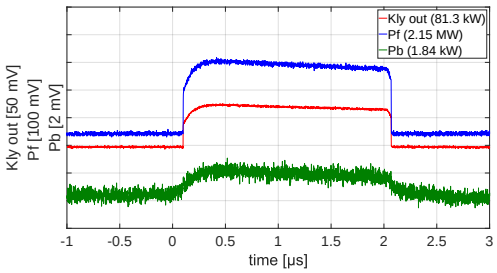

(d) Waveform at 2.0 MW power with a pulse width of 2 ms.

Figure 6.22: High power test result of the three fixed phase shifters without arcing. The power source is shut down when the testing time is longer than the target of 30 minutes.

Table 6.5 shows the result of the high power test of the fixed phase shifter. Arcing does not occur during these high power tests. After the operation, the power source is shut down to complete the test. The power handling capability of the three fixed phase shifters can satisfy the requirements of the compact LPDS.

Table 6.5: Result of the high power test of the three fixed phase shifter without arcing. After the operation, the power source is shut down to complete the test.

Power	Pulse width	Operation time
5.2 MW	200 µs	$\geq$ 30 minutes
2.0 MW	2 ms	$\geq$ 30 minutes

The investigation of the variable hybrids, variable phase shifters, and fixed phase shifters indicates that the S parameters and power handling capability can satisfy the requirements of the compact LPDS. The compact LPDS for

four cavities will be constructed and demonstrated in the STF.

Chapter 7

Evaluation and Operated Procedure of the Compact LPDS

The measured S parameter and high power test of the RF components satisfy the requirements of the compact LPDS. The compact LPDS will then be constructed in the tunnel of the Superconducting RF Test Facility (STF) to demonstrate its feasibility. This chapter introduces the low power test of the compact LPDS. Based on the schedule of beam operation in the STF, the high power test is expected to be performed in the 2021.

7.1 Construction of the Compact LPDS

Figure 7.1 shows the schematic for the construction of the compact LPDS for four cavities in the STF. This compact LPDS will be connected to four SC cavities installed in the cryomodule of 'CM–2a'. Considering the height of the STF tunnel and the supporting system, the compact LPDS is set on the horizontal plane. A bellow with a variable length is necessary to compensate for the production error of the geometric dimension and to decrease the mechanical stress. It will be installed between the circulator and the input coupler of the SC cavity.

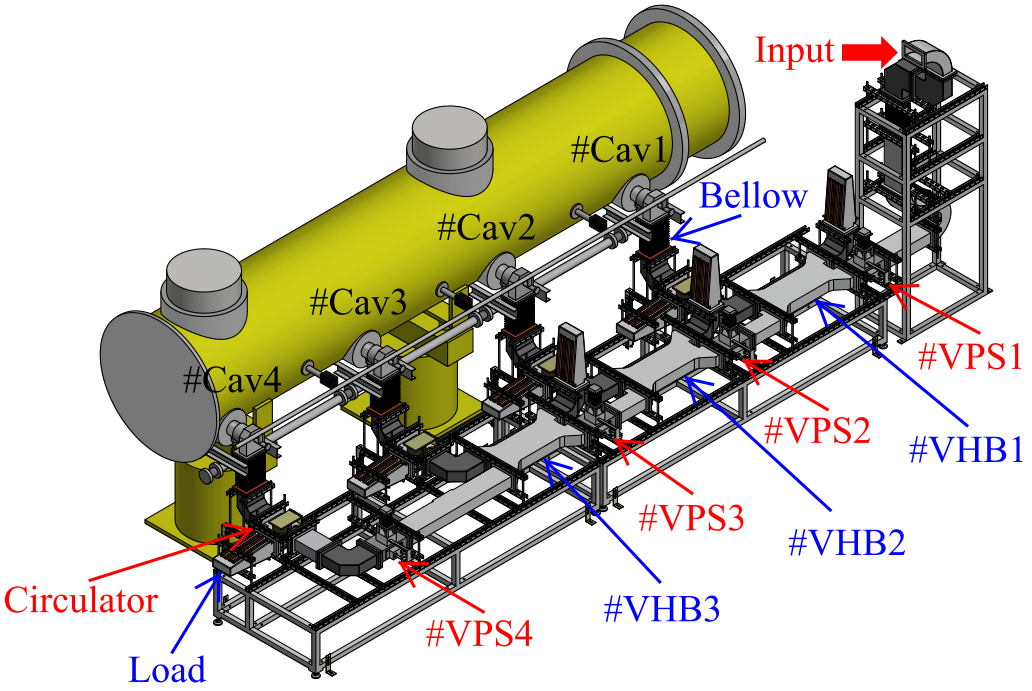

Figure 7.1: Schematic showing the construction of the compact LPDS and cryomodule 'CM–2a' for four cavities in the STF. The VHB and VPS are variable hybrid and variable phase shifter, respectively.

7.2 Low Power Test of the Compact LPDS

Figure 7.2 shows an image of the low power test setup for the compact LPDS for four cavities in the STF. The low power test of the compact LPDS is focused on the adjusted capability of the power distribution and phase. A 4-port network analyzer is used to obtain measurements and the three output ports of the compact LPDS can be measured simultaneously.

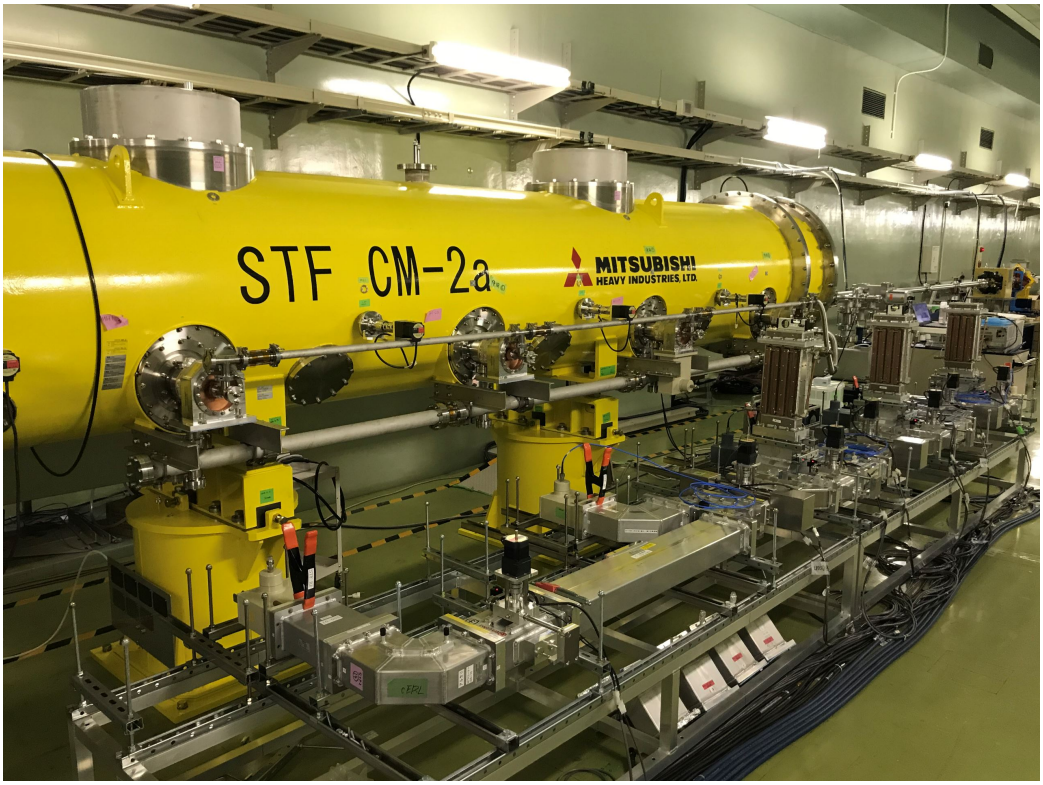

Figure 7.2: Image depicting the low power test of the compact LPDS for four cavities in the STF.

Firstly, the compact LPDS is adjusted to the average power distributed condition. The order of adjustment is as follows:

1) Set the three variable hybrids and the four variable phase shifters for the average power distributed condition based on the measured data of each component.

2) Adjust #VHB3 to equalize the power of #Cav3 and #Cav4.

3) Adjust #VPS4 to shift the phase difference between #Cav3 and #Cav4 to -90°.

4) Adjust #VHB2 to equalize the power of #Cav2, #Cav3 and #Cav4.

5) Adjust #VPS3 to shift the phase difference between #Cav2 and #Cav3 to -90°.

6) Adjust #VHB1 to equalize the power of #Cav1, #Cav2 and #Cav3.

7) Adjust #VPS2 to shift the phase difference between #Cav1 and #Cav2 to -90°.

Table 7.1 displays the measured result of the compact LPDS for four cavities for the average power distributed condition. The compact LPDS can realize the average power distributed condition and adjust the phase difference between adjacent cavities to -90°. The reflection to the input of the compact LPDS is -25.99 dB and the total power transmitted to the four cavities is 96.59% of the input power. The measured power loss of the compact LPDS for four cavities is -15.00 dB.

Table 7.1: Measured result of the compact LPDS for four cavities for the average power distributed condition.

	Power	Phase	Phase difference
#Cav1	-6.147 dB (24.28%)	-128.4°	
#Cav2	-6.179 dB (24.11%)	141.4°	-90.20
#Cav3	-6.152 dB (24.26%)	51.33°	-90.07°
#Cav4	-6.209 dB (23.94%)	-38.82°	-90.15°
Compact LPDS			
Reflection to input		-25.99 dB (0.25%)	
Total power of 4 cavities		96.59%	
Power loss of compact LPDS		-15.00 dB (3.16%)	

In the case of the average power distributed condition, the power transmitted to each cavity is approximately -6.20 dB of the input power of the compact LPDS for four cavities. The required adjusted range of power is $\pm 25\%$. Thus, the power transmitted to each cavity should be adjusted in the range of -5.2 dB to -7.5 dB. The three variable hybrids are adjusted individually, and the corresponding variable phase shifter should be adjusted to compensate for the phase shift of the variable hybrid.

Figure 7.3 shows the measured output power of the compact LPDS while #VHB1 and #VPS1 are adjusted. Figure 7.4 shows the measured output phase of the compact LPDS while #VHB1 and #VPS1 are adjusted. The measured result indicates that the power of #Cav1 can be adjusted from -8.009 dB to -4.585 dB, and the phase of #Cav1 $\sim$ #Cav3 are approximately maintained. Thus, the #VPS1 can compensate for the phase shift of #VHB1 while the coupling ratio is adjusted to $\pm 25\%$. Figure 7.5 shows the relationship for the count of the step motor between #VHB1 and #VPS1.

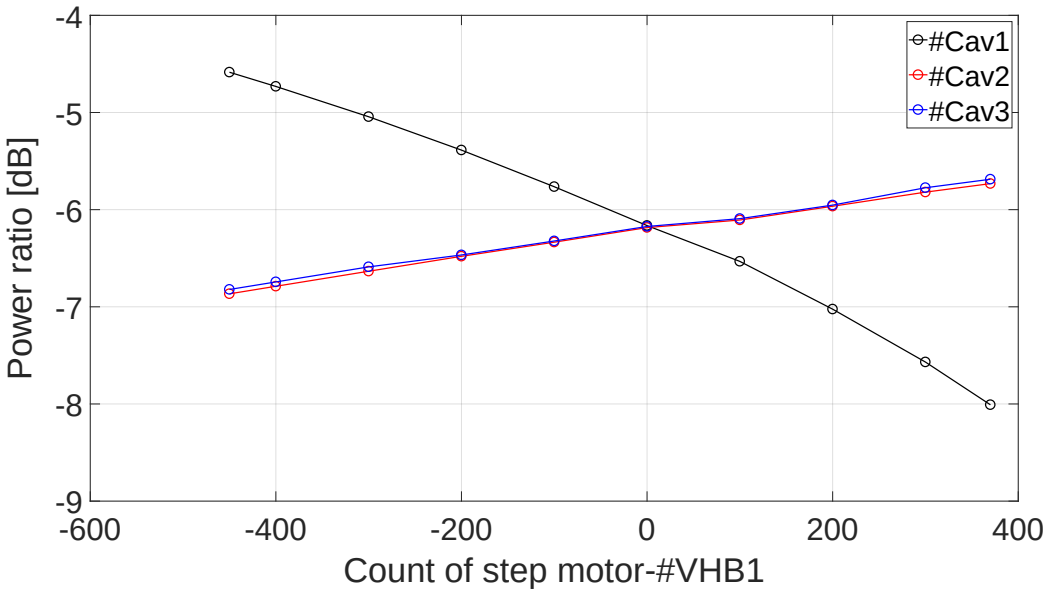

Figure 7.3: Measured output power of the compact LPDS while #VHB1 and #VPS1 are adjusted.

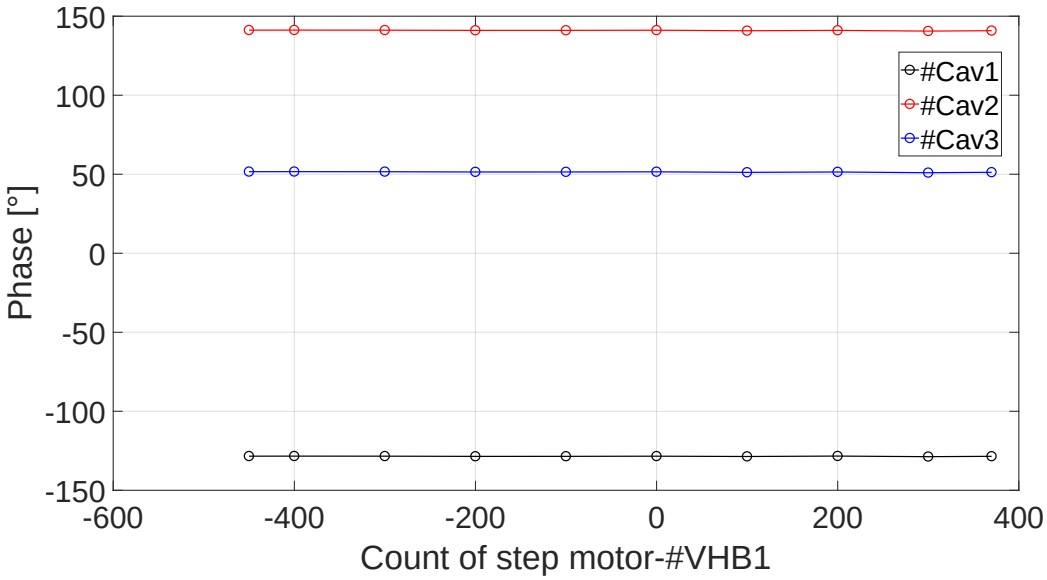

Figure 7.4: Measured output phase of the compact LPDS while #VHB1 and #VPS1 are adjusted.

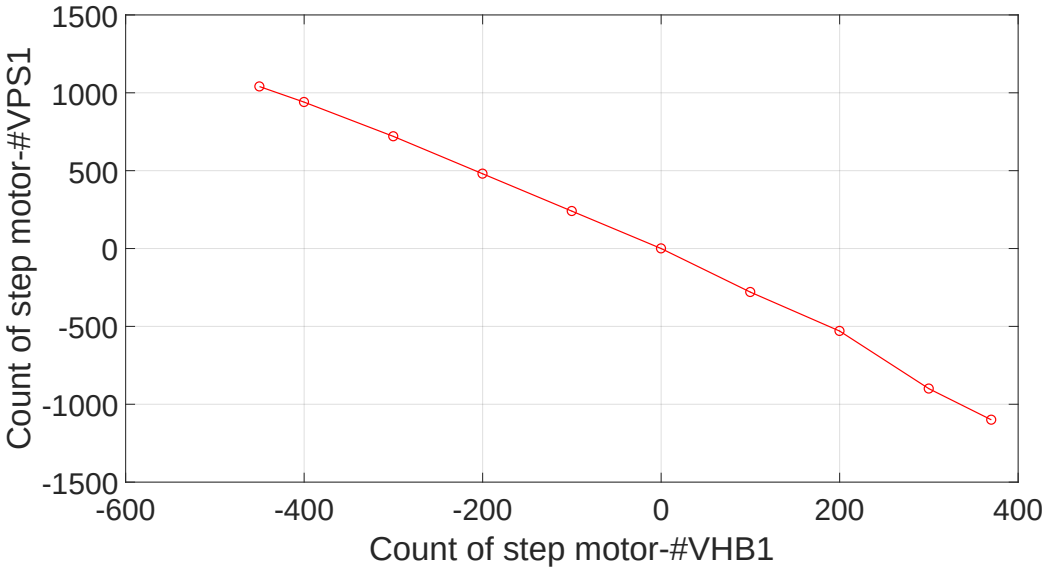

Figure 7.5: Relationship for the count of the step motor between #VHB1 and #VPS1.

Figure 7.6 shows the measured output power of the compact LPDS while #VHB2 and #VPS2 are adjusted. Figure 7.7 shows the measured output phase of the compact LPDS while #VHB2 and #VPS2 are adjusted. The measured result indicates that the power of #Cav2 can be adjusted from -7.784 dB to -4.812 dB, and the power of #Cav1 is approximately maintained. In addition, the phase of #Cav1 $\sim$ #Cav3 are approximately maintained during the adjustment. Thus, #VPS2 can compensate for the phase shift of #VHB2 while the coupling ratio is adjusted to $\pm 25\%$. Figure 7.8 shows the relationship of the count of the step motor between #VHB2 and #VPS2.

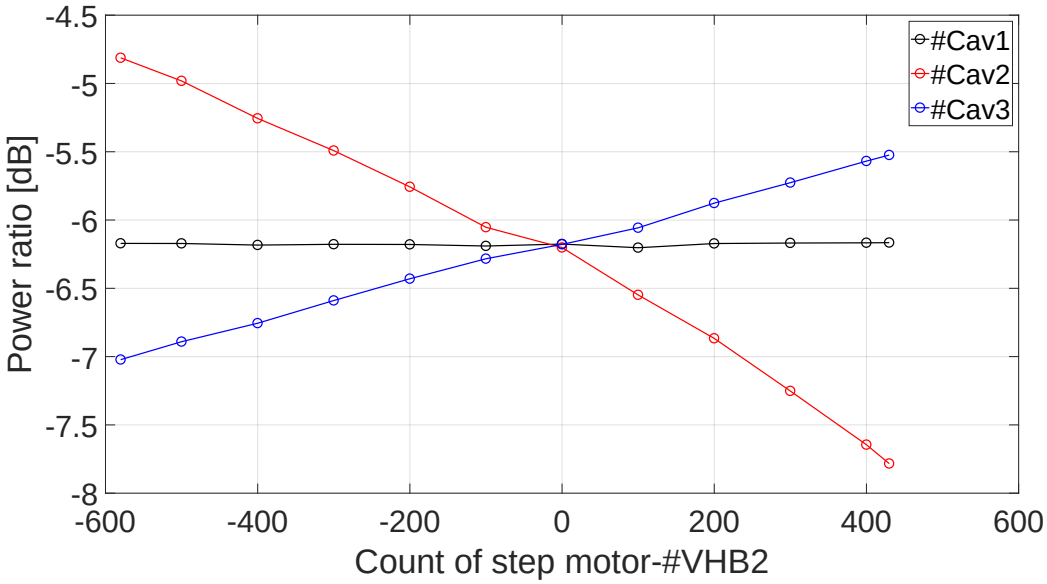

Figure 7.6: Measured output power of the compact LPDS while #VHB2 and #VPS2 are adjusted.

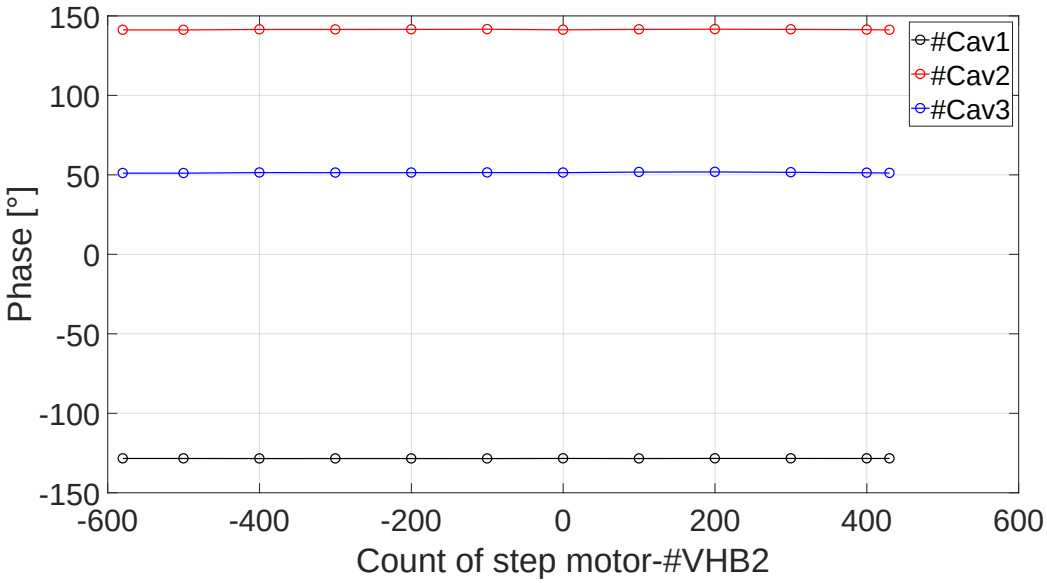

Figure 7.7: Measured output phase of the compact LPDS while #VHB2 and #VPS2 are adjusted.

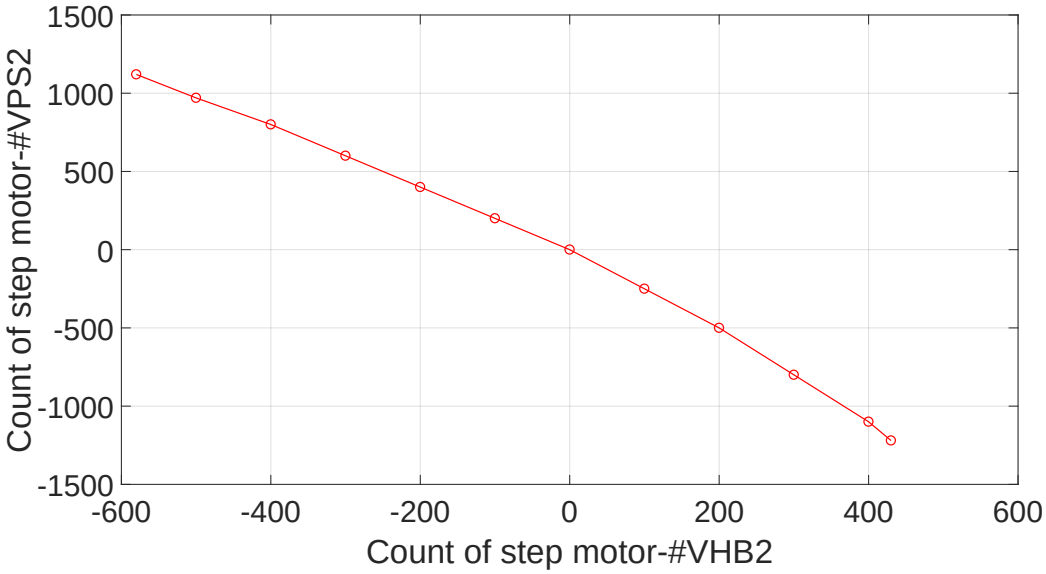

Figure 7.8: Relationship of the count of the step motor between #VHB2 and #VPS2.

Figure 7.9 shows the measured output power of the compact LPDS while #VHB3 and #VPS3 are adjusted. Figure 7.7 shows the measured output phase of the compact LPDS while #VHB3 and #VPS3 are adjusted. The measured result indicates that the power of #Cav3 can be adjusted from -5.113 dB to -7.630 dB and the power of #Cav2 is approximately maintained. In addition, the phase of #Cav2 $\sim$ #Cav4 are approximately maintained during the adjustment. Thus, #VPS3 can compensate for the phase shift of #VHB3 while the coupling ratio is adjusted to $\pm 25\%$. Figure 7.8 shows the relationship of the count of the step motor between #VHB3 and #VPS3.

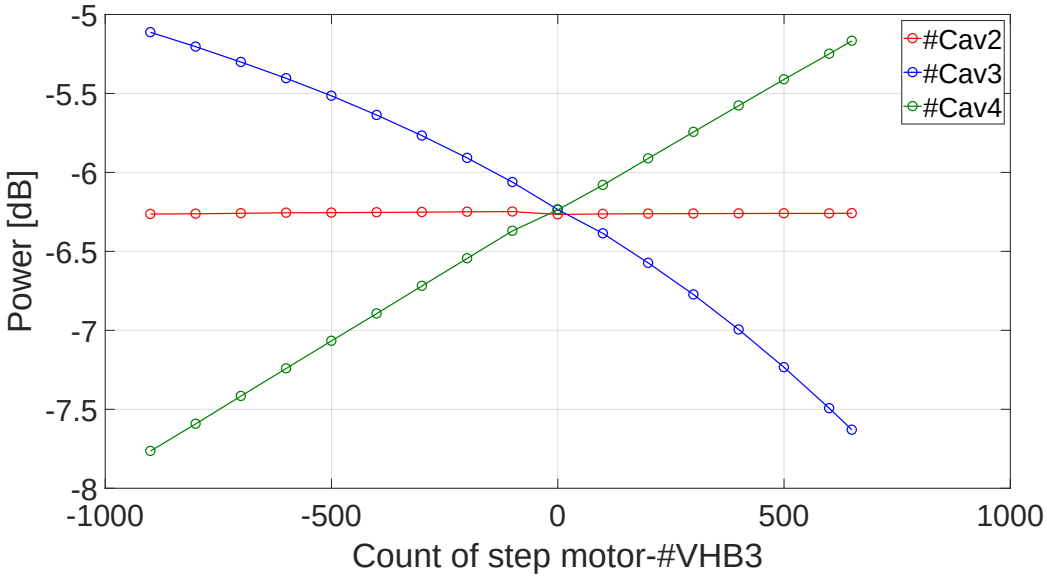

Figure 7.9: Measured output power of the compact LPDS while #VHB3 and #VPS3 are adjusted.

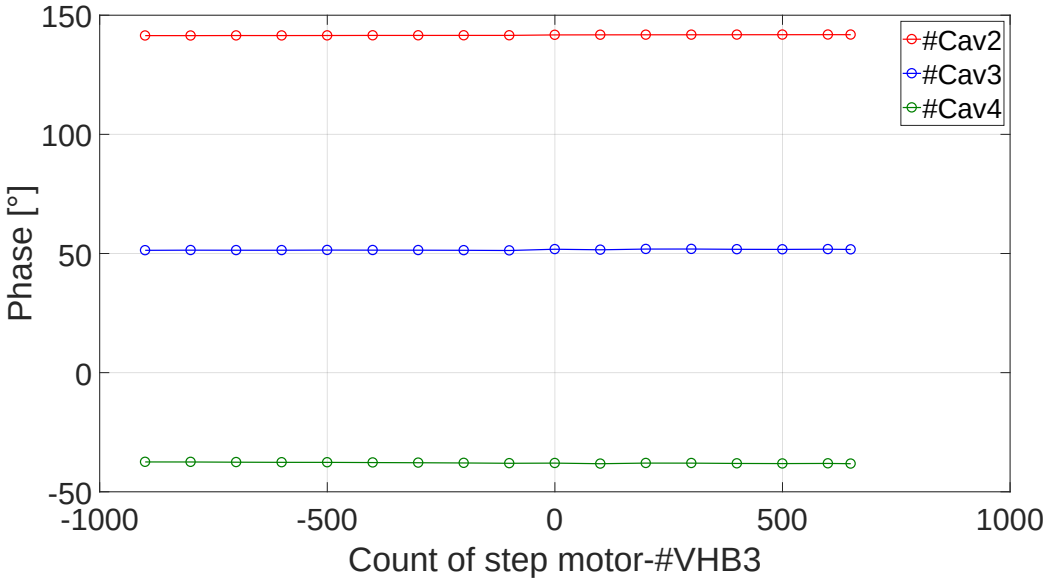

Figure 7.10: Measured output phase of the compact LPDS while #VHB3 and #VPS3 are adjusted.

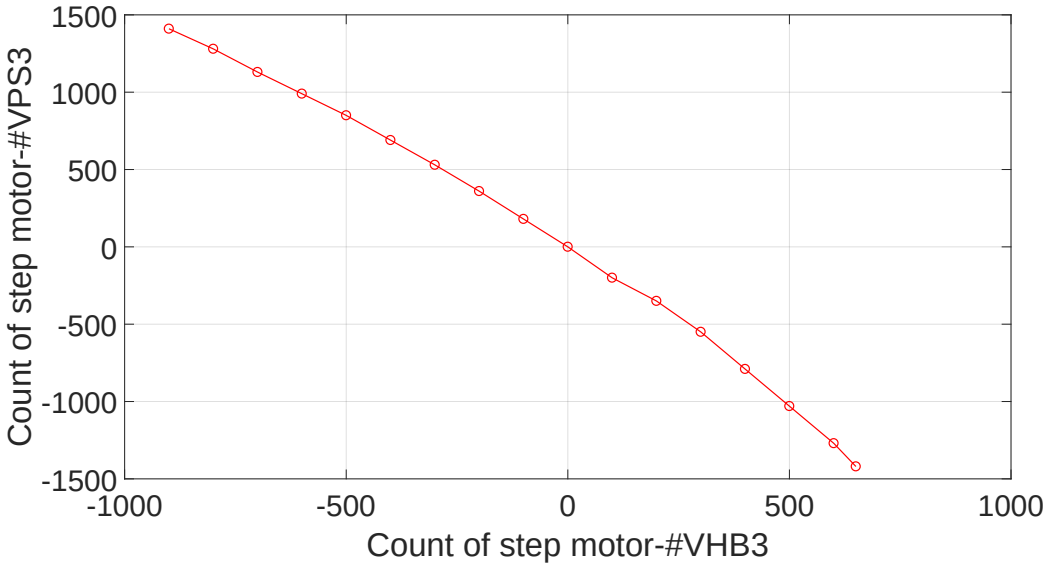

Figure 7.11: Relationship of the count of the step motor between #VHB3 and #VPS3.

Finally, only the #VPS4 is adjusted. The measured result indicates that the phase of #Cav4 can be adjusted from $-60.38°$ to $-20.44°$ and the phase of #Cav2 and #Cav3 is approximately maintained. The phase shift range of #VPS4 is 39.94°. In addition, the power of #Cav2 $\sim$ #Cav4 is approximately maintained during the adjustment.

Based on the low power test of the compact LPDS, the variable hybrid can realize $\pm 25\%$ variation of the power coupling ratio, and the variable phase shifter can compensate for the phase shift of the followed variable hybrid.

Table 7.2 displays the measured phase margin of #VPS1 $\sim$ #VPS4. The measured phase margin is shifted from the simulated value due to the phase difference between the measurement and the simulation for the variable hybrid, and the fixed phase shifter. Based on the measured phase margin, the required uniformity of the phase for the circulators, and bellows for different cavities, should be better than 4°.

Table 7.2: Measured phase margin of #VPS1 ∼ #VPS4.

	Measured phase margin	Simulated phase margin
#VPS1	$-16.0^\circ \sim 9.77^\circ$	$-11.06^\circ \sim 10.12^\circ$
#VPS2	$-16.1^\circ \sim 4.47^\circ$	$-10.21^\circ \sim 9.65^\circ$
#VPS3	$-14.5^\circ \sim 5.67^\circ$	$-9.27^\circ \sim 8.79^\circ$
#VPS4	$-22.0^\circ \sim 17.9^\circ$	$-17.5^\circ \sim 17.5^\circ$

7.3 Operation procedure of the Compact LPDS

Based on the low power test of the RF components and the compact LPDS, the table displays the related count number of the step motor between the variable hybrid and the variable phase shifter. Using this table, the shifted value of the step motor of the variable phase shifter can be automatically calculated when the variable hybrid is adjusted. The operation procedure of the compact LPDS is shown as follow:

1) Calculate the required generator power based on the maximal gradient of each cavity.

2) Calculate the required coupling ratio of each variable hybrid.

3) Adjust the variable hybrid for the required coupling ratio.

4) Adjust the variable phase shifter to compensate for the phase shift of the variable hybrid.

5) Finally, the power ratio between the cavities is equal to the calculated value and the phase difference between adjacent cavities is 90°.

Chapter 8

Conclusion and Future Prospects

The 250 GeV ILC is a future electron-positron collider that utilizes the superconducting RF technology. The PDS is developed to transmit RF power from one multi-beam klystron to 39 SC cavities. Each PDS is composed of three LPDSs for 13 cavities. The maximal accelerating gradient of each cavity has $\pm 20\%$ variation from 31.5 MV/m, depending on the cavity's performance. A variable hybrid and variable phase shifter are employed in the LPDS to adjust the RF power and the phase of each cavity can operate the SC cavity close to the quench limit and accelerate beams on the crest of the RF field. Thus, the maximal average accelerating gradient of the main LINAC can be achieved. The initial design of PDS and LPDS is shown in the ILC-TDR. Due to the limited space of the tunnel, the cryomodule integrated with the LPDS is expected to be assembled in the tunnel by a cart. In the case of the LPDS in the ILC-TDR, it seems to be difficult of facilitating removal of the cart after the installation process of the cryomodule.

The primary motivation of this research was to develop a compact LPDS that can be integrated on the cryomodule and reduce the production cost. The process began with the design of the model, followed by the design of the RF components. The RF components are manufactured and tested at low power using a network analyzer and at high power using a L-band resonant ring. Finally, the compact LPDS is constructed and tested at low power in the tunnel. The power handling capability of the RF components and the adjusted range of the compact LPDS are demonstrated. This research was conducted at the Superconducting RF Test Facility (STF) at the KEK. The main results can be summarized as follows:

- Several candidate models for the compact LPDS was presented. The

requirements of the compact LPDS was analyzed in detail.

- The compact RF components of the variable hybrid (730 mm) and the variable phase shifter (300 mm) were designed. The variable hybrid can realize the adjustment of the power coupling ratio from -8.84 dB to -2.04 dB to operate the SC cavity close to its quench limit. The variable phase shifter can realize the a change in the phase of 37.8° to compensate for the phase shift of the variable hybrid and reserve 15° for the margin.

- The concept of a fixed phase shifter was introduced to adjust the phase difference between adjacent cavities to 90°.

- The requirements of a low level RF control system was introduced based on a probabilistic analysis of the compact LPDS. When the Q_L is same for the cavities, the detuning should be controlled within ±16 Hz.

- Three variable hybrids, four variable phase shifters and three fixed phase shifters were manufactured. The measured S parameters met the requirements of compact LPDS.

- An L-band resonant ring was constructed in the STF for high power test of the RF components. The resonant ring was operated at 4.5 MW with a pulse width of 1.65 ms for 120 minutes in 2019.

- The power handling capability of the RF components was evaluated using the resonant ring and it was determined that they satisfy the requirements of the compact LPDS. These RF components can be operated at a power of 2 MW with a pulse width of 2 ms and a power of 5.2 MW with a pulse width of more than 50 μs.

- The compact LPDS was constructed in the STF. The adjustment of power and phase was demonstrated and was determined to satisfy the requirements of the compact LPDS.

- The operation procedure of the compact LPDS was presented.

In the future, the compact LPDS and the operating procedure will be demonstrated for high power operation, and beam commissioning in the STF. In addition, downstream of the compact LPDS, a new type of fixed phase shifter will be designed to meet the required phase.

Appendix A

Vector Diagram of Cavity Field

Figure A.1 shows the vector diagram for the voltage and current of the cavity. Table A.1 displays the definition of the vector for the voltage and current, and the angle of the cavity.

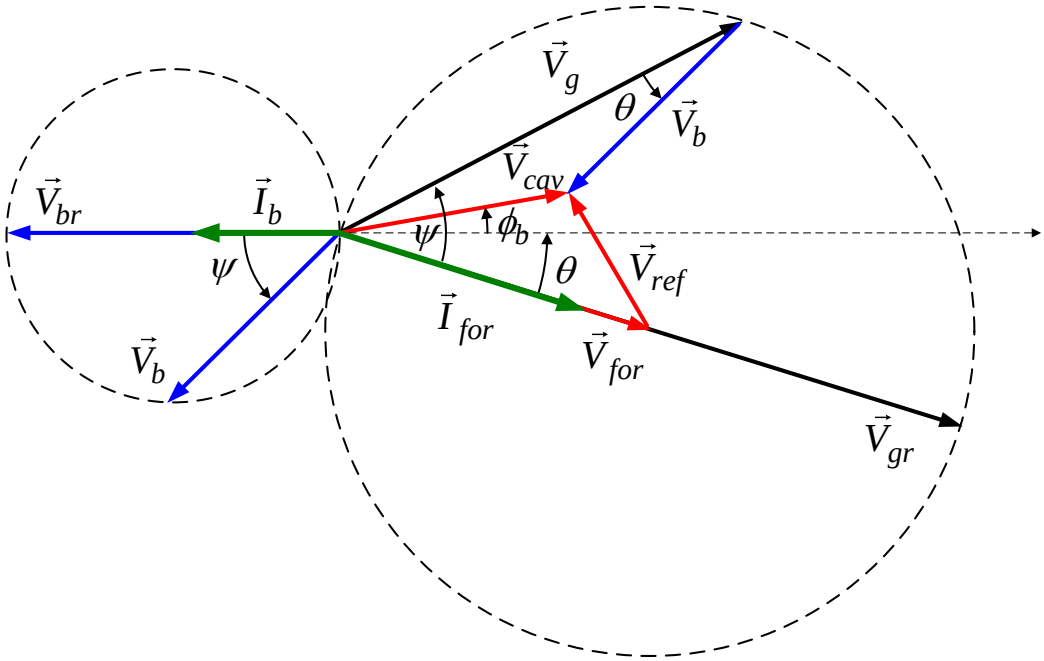

Figure A.1: Vector diagram for the voltage and current of the cavity.

Table A.1: Definition of the vector for the voltage and current, and the angle of the cavity.

V_g	Voltage generated by generator current
V_{gr}	Voltage generated by generator current on resonance
V_{for}	Incident voltage to cavity
V_{ref}	Reflected voltage from cavity
V_b	Voltage generated by beam current
V_{br}	Voltage generated by beam current on resonance
V_{cav}	Cavity voltage
I_g	Generator current
I_{for}	Incident current to cavity
I_{ref}	Reflected current from cavity
I_b	Beam current
I_{cav}	Cavity current
R	Cavity resistance
R_L	Loaded shunt impedance
Z_{cav}	Cavity impedance
Z_{ext}	External impedance
β	Coupling ratio
ψ	Tuning angle
ϕ_b	Beam phase
θ	Angle between I_g and real axis

Figure A.2 shows the equivalent circuit of the cavity driven by the generator. I_g is the generator current and I_{cav} is the cavity current. The impedance of the cavity, Z_{cav}, is expressed

$$\begin{aligned} \frac{1}{Z_{cav}} &= -\frac{1}{j\omega L} + \frac{1}{R} + j\omega C \\ Z_{cav} &= \frac{R}{1 - jR\left(\frac{1}{\omega L} - \omega C\right)} \end{aligned} \tag{A.1}$$

The external impedance Z_{ext} is the impedance of the transmission line Z_0 transformed to the cavity side.

$$Z_{ext} = N^2 \cdot Z_0 \tag{A.2}$$

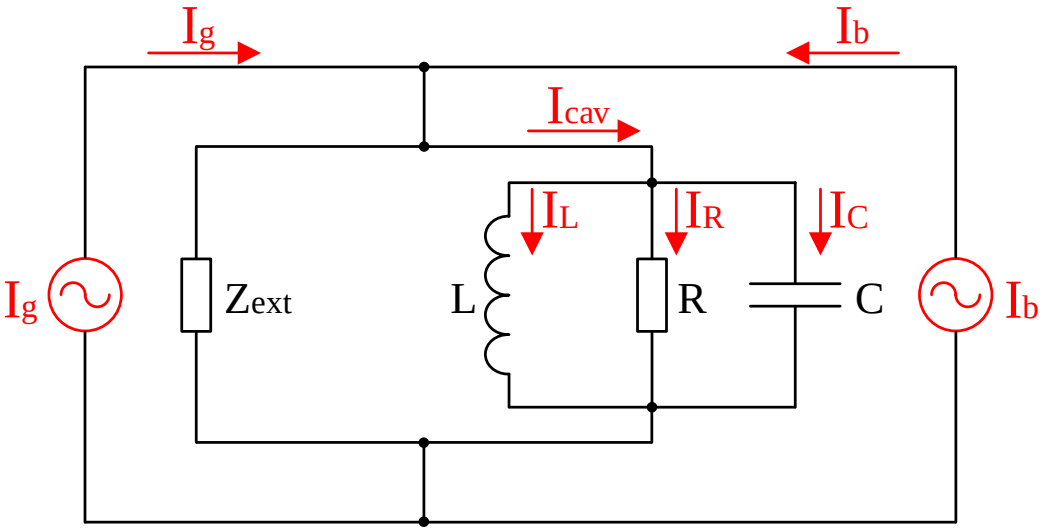

Figure A.2: Equivalent circuit of the cavity driven by the generator.

The coupling ratio β is defined as the ratio of the cavity resistor R and the external impedance Z_{ext}.

$$\beta = \frac{R}{Z_{ext}} \tag{A.3}$$

The external impedance Z_{ext} is parallel to the cavity resistance R. Thus the Z_{ext} and R can be replaced by a single resistor R_L, called the loaded shunt impedance.

$$\frac{1}{R_L} = \frac{1}{R} + \frac{1}{Z_{ext}} \tag{A.4}$$

Combining equations (A.3) and (A.4), the loaded shunt impedance R_L can be represented as

$$R_L = \frac{R}{1+\beta} \tag{A.5}$$

The vectors for the voltage and current of the cavity have the relationship

$$\vec{V}_{cav} = \vec{V}_{for} + \vec{V}_{ref} = \vec{V}_g + \vec{V}_b = Z_{cav} \cdot \vec{I}_{cav} \tag{A.6}$$

$$\vec{I}_{cav} = \vec{I}_{for} + \vec{I}_{ref} + \vec{I}_b \tag{A.7}$$

$$\vec{V}_{for} = Z_{ext} \cdot \vec{I}_{for} = \frac{R}{\beta} \cdot \vec{I}_{for} \tag{A.8}$$

$$\vec{V}_{ref} = -Z_{ext} \cdot \vec{I}_{ref} = -\frac{R}{\beta} \cdot \vec{I}_{for} \tag{A.9}$$

$$\vec{I}_{for} = \vec{I}_g \tag{A.10}$$

Inserting equations (A.8) and (A.9) into (A.7), we have

$$\vec{I}_{cav} = \frac{\vec{V}_{for}}{Z_{ext}} - \frac{\vec{V}_{ref}}{Z_{ext}} + \vec{I}_b \tag{A.11}$$

Combining equations (A.6) and (A.11), we have

$$\vec{V}_{ref} = \frac{1}{Z_{cav} + Z_{ext}} \cdot \left(\left(Z_{cav} - Z_{ext} \right) \vec{V}_{for} + Z_{cav} Z_{ext} \vec{I}_b \right) \tag{A.12}$$

Inserting equation (A.12) into (A.6), we have

$$\vec{V}_{cav} = \frac{Z_{cav}}{Z_{cav} + Z_{ext}} \cdot \left(2\vec{V}_{for} + Z_{ext} \vec{I}_b \right) \tag{A.13}$$

The cavity current $\vec{I}_{cav}$ can be calculated from the cavity voltage $\vec{V}_{cav}$

$$\vec{I}_{cav} = \frac{\vec{V}_{cav}}{Z_{cav}} = \frac{1}{Z_{cav} + Z_{ext}} \cdot \left(2\vec{V}_{for} + Z_{ext} \vec{I}_b \right) \tag{A.14}$$

The cavity voltage $\vec{V}_{cav}$ and cavity current $\vec{I}_{cav}$ can be represented using the tuning angle ψ and the coupling factor β

$$\begin{aligned} \vec{V}_{cav} &= \frac{\beta}{\beta + 1} \cdot \frac{1}{1 - j\tan\psi} \cdot \left(2\vec{V}_{for} + \frac{R}{\beta} \vec{I}_b \right) \\ &= \frac{\beta}{\beta + 1} \cdot \cos\psi \cdot e^{j\psi} \cdot \left(2\vec{V}_{for} + \frac{R}{\beta} \vec{I}_b \right) \\ &= R_L \cdot \cos\psi \cdot e^{j\psi} \cdot \left(2\vec{I}_g + \vec{I}_b \right) \end{aligned} \tag{A.15}$$

$$\begin{aligned} \vec{I}_{cav} &= \frac{\beta \left(1 - j(\beta + 1)\tan\psi \right)}{(\beta + 1)(1 - j\tan\psi)} \cdot \left(2\frac{\vec{V}_{for}}{R} + \frac{1}{\beta} \vec{I}_b \right) \\ &= \frac{1}{\beta + 1} \cdot \frac{1 - j\beta\tan\psi + (\beta + 1)\tan^2\psi}{1 + \tan^2\psi} \cdot \left(2\vec{I}_g + \vec{I}_b \right) \end{aligned} \tag{A.16}$$

The first and second terms of equation (A.15) correspond to $\vec{V}_g$ and $\vec{V}_b$, respectively.

$$\begin{aligned}\vec{V}_g &= 2R_L\vec{I}_g \cdot \cos\psi \cdot e^{j\psi} \\ &= \vec{V}_{gr} \cdot \cos\psi \cdot e^{j\psi}\end{aligned} \tag{A.17}$$

$$\begin{aligned}\vec{V}_b &= R_L\vec{I}_b \cdot \cos\psi \cdot e^{j\psi} \\ &= \vec{V}_{br} \cdot \cos\psi \cdot e^{j\psi}\end{aligned} \tag{A.18}$$

The voltage generated by a generator current and beam current on the resonance ($\vec{V}_{gr}$ and $\vec{V}_{br}$) are expressed as

$$\vec{V}_{gr} = 2R_L\vec{I}_g \tag{A.19}$$

$$\vec{V}_{br} = R_L\vec{I}_b \tag{A.20}$$

In the case of the SC cavity, the coupling factor is much larger than 1 (for the ILC, $\beta \sim 1650$), thus $Z_{ext} \approx R_L$. $\vec{V}_{gr}$ is approximately two times $\vec{V}_{for}$.

$$\vec{V}_{gr} = 2R_L\vec{I}_g \approx 2Z_{ext}\vec{I}_g = \vec{V}_{for} \tag{A.21}$$

The reflected voltage and current from the cavity can be calculated from $\vec{V}_{cav}$ and $\vec{I}_{cav}$, respectively.

$$\begin{aligned}\vec{V}_{ref} &= \vec{V}_{cav} - \vec{V}_{for} \\ &= R_L \cdot \cos\psi \cdot e^{j\psi} \cdot \left(\frac{(\beta-1)+j(\beta+1)\tan\psi}{\beta}\vec{I}_g + \vec{I}_b\right)\end{aligned} \tag{A.22}$$

$$\begin{aligned}\vec{I}_{ref} &= -\frac{\vec{V}_{ref}}{Z_{ext}} \\ &= \frac{\beta}{\beta+1} \cdot \cos\psi \cdot e^{i\psi} \cdot \left(\frac{(\beta-1)+j(\beta+1)\tan\psi}{\beta}\vec{I}_g + \vec{I}_b\right)\end{aligned} \tag{A.23}$$

Appendix B

Generator power for flattop

The voltage and current for the cavity with beam loading have been introduced in the previous section. The generator power P_g and reflected power P_{ref} can then be calculated based on the cavity voltage $\vec{V}_{cav}$, beam current $\vec{I}_b$ and tuning angle ψ. Usually, the DC beam current I_{b0} is quoted. In the case of a periodic bunch where the bunch length is much shorter than the bunch space, the amplitude of the Fourier component of $|\vec{I}_b|$ with a frequency equal to the RF frequency ω_0 is approximately twice the amplitude of the DC component I_{b0} [17].

$$|\vec{I}_b| \approx 2 \cdot I_{b0} \tag{B.1}$$

The vector triangle composed of $\vec{V}_{cav}$, $\vec{V}_b$ and $\vec{V}_g$ is shown in the Fig. A.1. The magnitude of $\vec{V}_g$ is calculated as

$$\begin{aligned} V_g^2 &= V_{cav}^2 + V_b^2 - 2 \cdot V_{cav} V_b \cos(\psi - \phi_b) \\ &= (V_{cav}\cos\psi + V_b\cos\phi_b)^2 + (V_{cav}\sin\psi + V_b\sin\phi_b)^2 \end{aligned} \tag{B.2}$$

The generator power P_g can be calculated using $\vec{V}_{for}$ and $\vec{I}_{for}$

$$\begin{aligned} P_g &= \frac{1}{2} Re\vec{V}_{for} \cdot \vec{I}^*_{for} \\ &= \frac{R}{2\beta} I_g^2 \end{aligned} \tag{B.3}$$

The V_{gr} can be derived from the generated power P_g

$$
\begin{aligned}
|\vec{V}_{gr}| &= 2R_L|\vec{I}_g| \\
&= 2R_L\sqrt{\frac{2\beta P_g}{R}} \\
&= 2\sqrt{\frac{2\beta R_L P_g}{\beta+1}}
\end{aligned}
\tag{B.4}
$$

Based on the equations (A.17) and (A.18), we have

$$
\begin{aligned}
|\vec{V}_g| &= V_{gr}\cos\psi \\
|\vec{V}_b| &= V_{br}\cos\psi
\end{aligned}
\tag{B.5}
$$

The equation (B.2) can be rewritten using equations (A.20), (B.4) and (B.5) to give the following;

$$
\begin{aligned}
(V_{gr}\cos\psi)^2 = \quad & V_{cav}^2\cos^2\psi\left[\left(1+\frac{V_{br}}{V_{cav}}\cos\phi_b\right)^2\right. \\
& \left.+\left(\tan\psi+\frac{V_{br}}{V_{cav}}\sin\phi_b\right)^2\right] \\
\frac{8\beta}{\beta+1}R_L P_g = \quad & V_{cav}^2\left[\left(1+\frac{R_L|\vec{I}_b|}{V_{cav}}\cos\phi_b\right)^2\right. \\
& \left.+\left(\tan\psi+\frac{R_L|\vec{I}_b|}{V_{cav}}\sin\phi_b\right)^2\right] \\
P_g = \quad & \frac{\beta+1}{8\beta}\frac{V_{cav}^2}{R_L}\left[\left(1+\frac{2R_L I_{b0}}{V_{cav}}\cos\phi_b\right)^2\right. \\
& \left.+\left(\tan\psi+\frac{2R_L I_{b0}}{V_{cav}}\sin\phi_b\right)^2\right]
\end{aligned}
\tag{B.6}
$$

Usually, the parameters of normalized quality factor $\frac{r}{Q}$, loaded quality factor Q_L and detuning Δf are stated. In the case of the SC cavity, β is much larger than 1 and detuning is much smaller than the resonant frequency. The generator power P_g can then be represented as;

$$
\begin{aligned}
P_g = \quad & \frac{\beta+1}{4\beta}\frac{V_{cav}^2}{\left(\frac{r}{Q}\right)Q_L}\left[\left(1+\frac{\left(\frac{r}{Q}\right)Q_L I_{b0}}{V_{cav}}\cos\phi_b\right)^2\right. \\
& \left.+\left(\tan\psi+\frac{\left(\frac{r}{Q}\right)Q_L I_{b0}}{V_{cav}}\sin\phi_b\right)^2\right] \\
\approx \quad & \frac{1}{4}\frac{V_{cav}^2}{\left(\frac{r}{Q}\right)Q_L}\left[\left(1+\frac{\left(\frac{r}{Q}\right)Q_L I_{b0}}{V_{cav}}\cos\phi_b\right)^2\right. \\
& \left.+\left(\frac{\Delta f}{f_{1/2}}+\frac{\left(\frac{r}{Q}\right)Q_L I_{b0}}{V_{cav}}\sin\phi_b\right)^2\right]
\end{aligned}
\tag{B.7}
$$

Where $f_{1/2}$ is the bandwidth of the cavity.

$$
f_{1/2} = \frac{f_0}{2Q_L} \tag{B.8}
$$

The reflected power P_{ref} can be calculated from the reflected voltage $\vec{V}_{ref}$ and the reflected current $\vec{I}_{ref}$ (equations (A.22) and (A.23))

$$
\begin{aligned}
P_{ref} &= \frac{1}{2}\left\{\vec{V}_{ref}\cdot\vec{I}_{ref}^{*}\right\} \\
&= \frac{\beta}{\beta+1}\frac{R_L}{2}\cos^2\psi\left|\frac{(\beta-1)+j(\beta+1)\tan\psi}{\beta}\vec{I}_g+\vec{I}_b\right|^2 \\
&= \frac{\beta}{4(\beta+1)}\left(\frac{r}{Q}\right)Q_L\cos^2\psi\cdot \\
&\quad\left|\frac{(\beta-1)+j(\beta+1)\tan\psi}{\beta}\sqrt{\frac{4\beta}{\beta+1}\frac{P_g}{\left(\frac{r}{Q}\right)Q_L}}e^{-j\theta}+\vec{I}_b\right|^2
\end{aligned}
\tag{B.9}
$$

Where θ is the angle between the generator current I_g and the real axis.

$$\begin{aligned}\cos\theta &= \frac{V_g^2 + V_b^2 - V_{cav}^2}{2V_g V_b} \\ &= \frac{I_g^2 + I_{b0}^2 - \left(\dfrac{V_{cav}}{\left(\frac{r}{Q}\right) Q_L \cos\psi}\right)^2}{2I_g I_{b0}}\end{aligned} \tag{B.10}$$

In the case of optimal tuning, the second bracket in equation (B.7) vanishes. The generator power at optimal tuning $(P_g)_{opt}$ is expressed as;

$$(P_g)_{opt} = \frac{\beta+1}{4\beta}\frac{V_{cav}^2}{\left(\frac{r}{Q}\right) Q_L}\left(1 + \frac{\left(\frac{r}{Q}\right) Q_L I_{b0}}{V_{cav}}\cos\phi_b\right)^2 \tag{B.11}$$

The optimal tuning angle ψ_{opt} and optimal detune Δf_{opt} are expressed as

$$\begin{aligned}\tan\psi_{opt} &= -\frac{\left(\frac{r}{Q}\right) Q_L I_{b0}}{V_{cav}}\sin\phi_b \\ \frac{\Delta f_{opt}}{f_0} &= -\frac{\left(\frac{r}{Q}\right) I_{b0}}{2V_{cav}}\sin\phi_b\end{aligned} \tag{B.12}$$

Differentiating equation (B.11) with a variable coupling factor β to find the minimal value of generator power P_g, we have;

$$\begin{aligned}&\frac{\mathrm{d}\,(P_g)_{opt}}{\mathrm{d}\beta} = 0 \\ &\rightarrow \beta_{opt} = 1 + \frac{\left(\frac{r}{Q}\right) Q_0 I_{b0}}{V_{cav}}\cos\phi_b\end{aligned} \tag{B.13}$$

The minimal generator power $(P_g)_{min}$ is expressed as

$$(P_g)_{min} = \beta_{opt}\frac{V_{cav}^2}{\left(\frac{r}{Q}\right) Q_0} \tag{B.14}$$

The optimal tuning angle ψ_{opt} can be expressed using the optimal coupling factor β_{opt}.

$$\tan\psi_{opt} = -\frac{\beta_{opt}-1}{\beta_{opt}+1}\tan\phi_b \tag{B.15}$$

The optimal loaded quality factor $(Q_L)_{opt}$ can be calculated from optimal coupling factor β_{opt}.

$$(Q_L)_{opt} = \frac{Q_0}{1+\beta_{opt}} = \frac{V_{cav}}{2\frac{V_{cav}}{Q_0} + \left(\frac{r}{Q}\right) I_{b0}\cos\phi_b} \tag{B.16}$$

In the case of the SC cavity, β is much larger than 1, and the following approximation can be derived;

$$\begin{aligned}
(Q_L)_{opt} &\approx \frac{V_{cav}}{\left(\frac{r}{Q}\right) I_{b0}\cos\phi_b} \\
\tan\psi_{opt} &\approx \tan\phi_b \\
\rightarrow \psi_{opt} &\approx \phi_b \\
(P_g)_{min} &\approx \frac{V_{cav}^2}{\left(\frac{r}{Q}\right)(Q_L)_{opt}} \\
&= V_{cav}\cdot I_{b0}\cdot\cos\phi_b
\end{aligned} \tag{B.17}$$

$$P_{ref} \approx \frac{1}{1+\tan^2\psi}\cdot\left|(1+i\tan\psi)\sqrt{P_g}\cdot e^{-j\theta} + \frac{1}{2}\sqrt{\left(\frac{r}{Q}\right)Q_L}\vec{I}_b\right|^2 \tag{B.18}$$

The cavity voltage V_{cav} can be calculated using the accelerating gradient E_{acc} and the geometric length l of the cavity such that $V_{cav} = E_{acc}\cdot l$. Thus, the minimal generator power is expressed as

$$(P_g)_{min} = E_{acc}\cdot l\cdot I_{b0}\cdot\cos\phi_b \tag{B.19}$$

List of Figures

List of Tables

Bibliography

[1] ILC, http://www.linearcollider.org/ILC/?pid=1000895.

[2] https://www2.kek.jp/ipns/en/research/ilc/.

[3] L. Evans, S. Michizono. "The International Linear Collider Machine Staging Report 2017", Rep. KEK 2017-3, Oct. 2017. https://arxiv.org/abs/1711.00568.

[4] Y. H. Chin, S. Miyake, A. Yano, et al. "Development of 10 MW L-Band Multi-Beam Klystron (MBK) for european X-FEL project", in Proc. 22nd IEEE Particle Accelerator Conf. (PAC'07), Albuquerque, USA, 2007, pp. 2098-2100. https://ieeexplore.ieee.org/document/4441162.

[5] https://etd.canon/en/product/category/microwave/klystron.html.

[6] http://newsline.linearcollider.org/wp-content/uploads/2016/06/.

[7] C. Nantista, C. Adolphsen, F. Wang, et al. "Waveguide component R&D for the ILC (No. SLAC-PUB-15465)". SLAC National Accelerator Lab., Menlo Park, USA, 2013. https://accelconf.web.cern.ch/IPAC2013/papers/wepfi080.pdf.

[8] D. M. Pozar. "Microwave engineering", chapter 5. USA: John Wiley & Sons, 2009.

[9] S. Kazakov, S. Fukuda, M. Yoshida et al. "L-Band Waveguide Elements for SRF Application", in Proc. 6th Particle Accelerator Society Meeting (PASJ'09), Tokai, Japan, Aug. 2009, pp.980-982. https://www.pasj.jp/web_publish/pasj6/papers/fpaca22.pdf.

[10] Y. Yamamoto, T. Dohmae, M. Egi, et al. "Achievement of Stable Pulsed Operation at 36 MV/m in STF-2 Cryomodule at KEK", in Proc. 18th International Conf. on RF Superconductivity (SRF'17), Lanzhou, China, July 17-21, 2017, pp. 722-728. https://inspirehep.net/literature/1657099.

[11] "The European X-Ray Free-Electron laser; Technical Design Report", DESY 2006-097 (2007) http://xfel.eu/en/documents.

[12] S. Choroba. "The High Power RF System for the European XFEL". in Proc. 29th Linear Accelerator Conf. (LINAC'18), Beijing, China, Sep. 2018, pp. 601-604. https://accelconf.web.cern.ch/linac2018/papers/we1a04.pdf.

[13] V. Katalev and S. Choroba. "Waveguide distribution systems for the european XFEL", in Proc. European 10th Particle Accelerator Conf. (EPAC'06), Edinburgh, Scotland 2006. https://accelconf.web.cern.ch/e06/papers/tupch116.pdf.

[14] V. Katalev and S. Choroba. "Compact waveguide distribution with asymmetric shunt tees for the European XFEL", in Proc. 22nd IEEE Particle Accelerator Conf. (PAC'07), Albuquerque, USA, 2007, pp. 176-178. https://ieeexplore.ieee.org/abstract/document/4440150.

[15] S. Choroba. "The High Power RF System for the European XFEL", in Talk 29th Linear Accelerator Conf. (LINAC'18), Beijing, China, Sep. 2018. https://accelconf.web.cern.ch/linac2018/talks/we1a04_talk.pdf.

[16] B. T. Du, T. Matsumoto, S. Michizono, et al. "Design of a Compact Power Distribution System for the ILC", in Proc. 10th International Particle Accelerator Conf. (IPAC'19), Melbourne, Australia, May. 2019, pp. 436-438. https://ipac2019.vrws.de/papers/mopmp007.pdf.

[17] T. Schilcher. "Vector Sum Control of Pulsed Accelerating Fields in Lorentz Force Detuned Superconducting Cavities", Ph.D. thesis, Phys. Dept., University Hamburg, Hamburg, Germany, 1998. https://bib-pubdb1.desy.de/record/291638/files/schilcher.pdf.

[18] B. T. Du, T. Matsumoto, S. Michizono, et al. "Development of a compact Local Power Distribution System for the ILC." Nuclear Instruments and Methods in Physics Research Section A: Accelerators, Spectrometers, Detectors and Associated Equipment (2020): 164589. https://www.sciencedirect.com/science/article/pii/S0168900220309864.

[19] S. B. Wibowo. "Digital Low-Level RF Control System Development for International Linear Collider", Ph.D. thesis, Acc. Science Dept., Graduate University for Advanced Studies, Tsukuba, Japan, 2017. https://inspirehep.net/literature/1692716

[20] M. Omet. “Digital Low Level RF Control Techniques and Procedures Towards the International Linear Collider”, Ph.D. thesis, Acc. Science Dept., Graduate University for Advanced Studies, Tsukuba, Japan, 2014. http://id.nii.ac.jp/1013/00004769/.

[21] W. X. Wang. “Microwave Engineering Technology”, chapter 4, 2014.

[22] L. J. Milosevic and R. Vautey. “Traveling-Wave Resonators”, in IRE Transactions on Microwave Theory and Techniques, vol. 6, no. 2, pp. 136-143, April 1958. https://ieeexplore.ieee.org/abstract/document/1124528.

[23] K. Tomiyasu. “Attenuation in a Resonant Ring Circuit (Correspondence)”. IRE Transactions on Microwave Theory and Techniques, vol. 8, pp. 253-254, 1960. https://ieeexplore.ieee.org/abstract/document/1124738.

[24] H. Itoh, M. Shimozuma, H. Tagashira, et al. “Measurement of the effective ionisation co-efficient and the static breakdown voltage in SF_6 and nitrogen mixtures”, J. Phys. D: Appl. Phys., vol. 12, pp. 2167-2172, Feb. 1979. https://iopscience.iop.org/article/10.1088/0022-3727/12/12/018/meta.

[25] B. T. Du, T. Matsumoto, S. Michizono, et al. “L-Band Resonant Ring for Testing RF Windows for ILC”, in Proc. 29th Linear Accelerator Conf. (LINAC’18), Beijing, China, Sep. 2018, pp.679-681. https://www-linac.kek.jp/linac-paper/2018/linac18-du-resonantring.pdf.

[26] B. T. Du, T. Matsumoto, S. Michizono, et al. “High-power Operation of an L-band Resonant Ring”, Proc. 16th Annual Meeting of Particle Society of Japan International (PASJ’19), Kyoto, Japan, Jul. 2019, pp. 884-886. http://www.pasj.jp/web_publish/pasj2019/proceedings/PDF/FRPH /FRPH009.pdf

[27] J. S. Rigden (Ed.). “Macmillan encyclopedia of physics.” Physics Today 50, 1997, p. 65. doi:10.1063/1.881915.

[28] B. T. Du, T. Matsumoto, S. Michizono, et al. “Development of a compact Local Power Distribution System for the ILC.” Nuclear Instruments and Methods in Physics Research Section A: Accelerators, Spectrometers, Detectors and Associated Equipment (2020): 164589. https://www.sciencedirect.com/science/article/pii/S0168900220309864

Acknowledgments

I would like to thank every one who supported my doctoral research and dissertation.

Firstly, I would like to thank my supervisor Toshihiro Matsumoto. His advice over the years proved to be helpful and highly relevant to my research. He taught me how to become a better researcher. I wish to thank our group leader Shinichiro Michizono for his many key suggestions regarding for my research. I would also like to thank Takako Miura for her comments. A special thank you to ZhiGao Fang for introducing me to the KEK and for his assistance in application. I thank Feng Qiu and Na Liu for the numerous discussions and their support while in Japan.

I thank the Japan Ministry of Education, Science and Culture for the MEXT scholarship.

I am thankful to my master's supervisor GuiRong Huang. He was very supportive over the long distance between China and Japan. I wish to thank to YontTao Liu and HongXiang Lin who were members of the RF group in the NSRL. I thank my classmates ZhuoXia Shao, XiaoKang Sun, Gangwen Liu, Ziyu Huang for the wonderful time spent in the USTC.

Finally, I also wish to thank my entire family for the great support I received. I thank my wife for accompanying me to Japan for three years. Furthermore, I would like to thank all the friends who supported me throughout my academic journey.

Baiting Du

Declaration

I declare that I wrote this Ph.D.–dissertation independently and without any other references and resources than that stated in the bibliography.

Tsukuba, JAPAN